Department of Precision and Microsystems Engineering

Dynamic calibration for high accuracy flux control of reluctance actuators

Bochen Hao

Report no : 2023.091
Coach : Dr. ir. Leon Jabben
Professor : Dr. S. Hassan Hossein Nia Kani
Specialisation : Mechatronic System Design
Type of report : Master Thesis
Date : 20 November 2023

Dynamic calibration for high accuracy flux control of reluctance actuators

by

Bochen Hao

Department of Precision and Microsystems Engineering
Delft University of Technology

to obtain the degree of Master of Science

to be defended publicly on Monday November 20, 2023 at 1:00 PM.

Student number:	5473926	
Project duration:	December 2022 – November 2023	
Supervisors:	Dr. ir. L. Jabben,	MI-Partners
	Dr. S. H. HosseinNia,	TU Delft

This thesis is confidential and cannot be made public until November 19, 2025.

TU Delft

Summary

In the semiconductor industry, the demand for a continuously higher throughput puts tough requirements on the force capacity and accuracy of actuators. Reluctance actuators, as a promising alternative to the present state-of-the-art Lorentz actuators, are capable of achieving much higher force densities. On the other hand, reluctance actuators suffer from strong intrinsic nonlinearity, such as the quadratic and position-dependent current-force relation, negative stiffness, and magnetic hysteresis, making accurate control challenging. These nonlinear effects can be much suppressed if, instead of controlling the current through the driving coil, the magnetic flux in the actuator core is controlled. As a preparation step for implementing the flux control experimentally on reluctance actuators, this project aims to design and realise the necessary hardware for flux control implementation, including a reluctance actuator prototype and a test setup, and then dynamically calibrate the actuator for flux measurement and control. More specifically, a hybrid reluctance actuator prototype that is suitable for flux control, as well as a test setup for measuring the position and dynamic force output of the actuator, are designed and realised. Using this setup, relations between key variables of the actuator are measured to enable nonlinear compensation in the current and flux control, and a hybrid flux measuring scheme using a Hall sensor and a sense coil is proposed and experimentally implemented. Although noise in the flux measurement is effectively minimised, the result shows a mismatch in the frequency domain between the outputs of the Hall sensor and the sense coil, where further investigation is needed to improve the feasibility of this approach. Furthermore, a hybrid force measuring scheme is proposed and implemented where errors of the load cell due to high-frequency dynamics of the setup can be compensated using acceleration measurements, leading to a wider frequency range for the force measurement. With the realised hardware and the obtained measurements from this project, the next step in future works would be to experimentally implement the flux control on a reluctance actuator and compare its performance with the standard current control.

Contents

1 Introduction

1.1. Background

For production in the semiconductor industry, both high accuracy and high throughput are desired, which put tough requirements on equipment such as wafer scanners. Usually, Lorentz actuators are applied due to their high linearity and low stiffness. However, when increasingly higher throughput is demanded, Lorentz actuators are unable to produce the higher accelerations needed to drive the mover stage. As a promising alternative, reluctance actuators are capable of achieving a much higher force density at small air gaps. However, their strong intrinsic nonlinearity, such as the nonlinear current-force relation, position-dependent negative stiffness, and hysteresis effect, make the design and control of reluctance actuators rather challenging. Currently, current-based and flux-based feedback control are the two common control modes being studied, together with other techniques to yield better linearity and accuracy.

At MI-Partners where this project is proposed and carried out, reluctance actuators with flux control have been of interest for high-precision high-frequency applications such as the positioning of a maglev stage. However, its feasibility and achievable performance have yet to be sufficiently proved and compared with the standard current-mode control. Thus, a series of projects have been formulated, aiming to implement and evaluate flux control relative to current control, in terms of tracking accuracy, force predictability, linearity as well as the influence of other bandwidth-limiting effects.

This thesis project continues the preceding work by another student [1], which focused on theoretical analysis and simulations of current control and flux control. The expected advantages of flux control over current control were proved on the theoretical level. Furthermore, a flux measurement scheme by merging a Hall sensor with a sense coil was proposed and validated in simulations. Its advantages over using a single flux sensor in terms of noise suppression were shown by noise analysis and simulations. As a continuation of the previous project and a preparation step for the experimental implementation of flux control, this thesis project aims to design and realise the necessary hardware for flux control implementation, including a reluctance actuator prototype and a corresponding test setup, and then dynamically calibrate the actuator for flux measurement and control.

1.2. State of the Art

The presence of the above-mentioned nonlinear effects poses a great challenge in accurately controlling reluctance actuators with a high bandwidth. Thus, special efforts and techniques for linearising the actuator are of great importance. One approach would be to optimise the design of the actuator, which however provides a very limited linearisation effect. As a result, active feedback

control would still be needed to compensate for the rest of the nonlinearity. A typical control method is the current feedback control, which is relatively easy to implement thanks to its common application on Lorentz actuators. However, some major nonlinear effects, such as the $B(I)$ relation which involves position dependency and magnetic hysteresis, remain out of the current control loop and thus cannot be compensated [2]. Alternatively, one can control the flux in the air gap directly, so that the position dependency and hysteresis effect can be much suppressed and a better linearisation effect can be achieved. It is experimentally verified in the literature that a flux-controlled reluctance actuator is able to achieve a significantly higher position accuracy and better linearity than a current-controlled one [2][3]. However, the challenge for implementing flux control would be to measure magnetic flux accurately across a wide frequency range. In [2][3][4], hybrid flux estimation schemes using a sense coil together with a Hall sensor or a current sensor are implemented, and as a result, a wider measurable frequency range and a lower output noise than using either sensor can be achieved by taking advantage of the complementary characteristics of the two flux sensors. These state-of-the-art approaches for linearising the actuator can be selectively applied in the linearisation scheme proposed in this project.

1.3. Project Overview

1.3.1. Project Definition

This project aims to carry out dynamic flux calibration for a reluctance actuator, to characterise the actuator for implementing the flux control. As preliminaries, a reluctance actuator prototype and a test setup will be designed and built.

1.3.2. Objectives and Methodology

To achieve the project goal stated above, the following objectives and corresponding methodology are defined.

- **Design and realise a reluctance actuator prototype that is suitable for flux control.**
  For given requirements, a reluctance actuator prototype will be designed, validated using FEM analysis, manufactured, and assembled to provide a target to test on. Flux sensors will be implemented, and a scheme for dynamic flux measurement will be proposed and applied.

- **Design and realise a test setup for dynamic calibration of the designed reluctance actuator.**
  A test setup will be designed that enables dynamic force measurement across a wide frequency range. Besides, the setup will also provide high-stiffness support to the actuator and the ability to position the actuator within its operating gap range.

- **Perform dynamic calibration on the realised reluctance actuator prototype for current and flux control.**
  Relationship between key variables will be measured to characterise the actuator and validate the proposed flux measuring scheme, in preparation for the implementation of the current and flux control.

1.3.3. Report Overview

In the following chapters of this project, work corresponding to the above-mentioned objectives will be introduced respectively. Firstly, chapter 2 provides preliminary knowledge by deriving fundamental theories and carrying out literature reviews on actuator linearisation and flux measurement. Then, chapter 3 and chapter 4 describe the design and realisation process of the reluctance actuator prototype and the test setup, respectively. Finally, dynamic calibration and other relevant measurements carried out on the designed reluctance actuator are discussed in chapter 5. In the end, conclusions and recommendations will be given in chapter 6.

2

Preliminary

To get more insight into the working principle and state-of-the-art control techniques of reluctance actuators, some preliminary studies and literature reviews are carried out. Firstly, fundamental theories of reluctance actuators are derived to reveal crucial underlying relationships, from which some intrinsic nonlinear effects can be discovered that make it challenging to realise accurate control. Besides, to study state-of-the-art approaches for handling the actuator nonlinearity during control, relevant literature is reviewed, covering different approaches including special actuator designs, feedback control in different modes, as well as advanced techniques applied in the feedback control.

2.1. Fundamentals of Reluctance Actuators

2.1.1. Basic Construction

A standard reluctance actuator consists of a coil for generating a variable magnetomotive force, and a ferromagnetic core to provide a high-permeability path for magnetic flux. The core consists of two separate parts, the stator and the mover, with an air gap of variable size in between. The "C-I" (Figure 2.1(a)) and "E-I" (Figure 2.1(b)) are two typical configurations for reluctance actuators, which consist of a C- or E-shaped stator and an I-shaped mover.

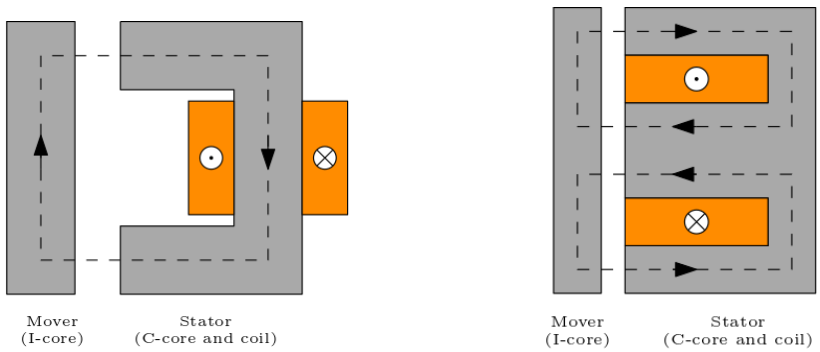

Figure 2.1: Reluctance actuators in (a) C-I and (b) E-I configurations.

In comparison, an E-core can be considered as splitting the flux loop in a C-core stator into two parallel loops, which enables the E-core to utilise the thickness of the mover and the space between poles more efficiently [5]. However, as a drawback, the E-I design is susceptible to any kind of

asymmetry and some stray torque might exist due to unequal force generated in the two loops [4].

These basic designs are only capable of generating an attractive force. A double-actuator design (Figure 2.2) can be applied to produce bi-directional forces. Besides, some special actuator configurations are developed to produce a bi-directional force in a more efficient and simple way, such as the one shown in Figure 2.4(b) which has a position-independent linear relation between force and flux.

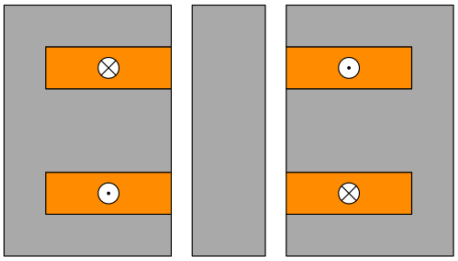

Figure 2.2: A double-actuator configuration for reluctance actuators, which enables the production of bi-directional forces.

2.1.2. Fundamental Theories

In this section, taking the "C-I" configuration introduced in section 2.1.1 as an example, the basic relations for analysing reluctance actuators are derived (referring to section 2.1 in [4] and chapter 2 in [3]).

Magnetic flux calculation

Ampère's law can be expressed as

$$\oint_C \mathbf{H} \cdot \mathrm{d}\mathbf{l} = \iint_S \mathbf{J} \cdot \mathrm{d}\mathbf{S} \tag{2.1}$$

where the left-hand side of the equation represents the line integral of magnetic field intensity $\mathbf{H}$ around a closed curve C is equal to the surface integral of current density $\mathbf{J}$ across a surface S enclosed by C. Applying this equation along the closed curve shown in Figure 2.1(a) gives

$$H_c l_c + 2H_g l_g = NI \tag{2.2}$$

where the subscript $_c$ denotes the ferromagnetic core and $_g$ the air gap, and N is the number of windings of the driving coil. Note that the magnetic field intensity within the core H_c and the air gap H_g are assumed constant along the specified path.

The Gauss's law for magnetism can be expressed as

$$\oiint_S \mathbf{B} \cdot \mathrm{d}\mathbf{S} = 0 \tag{2.3}$$

which states that the net magnetic flux passing through any closed surface S is always zero. This lets us relate the magnetic flux densities in the core and the air gap using

$$\Phi = B_c A_c = B_g A_g \tag{2.4}$$

where Φ is the magnetic flux at any cross-section along the specified path.

To relate the two equations derived from Ampère's law and Gauss's law, the magnetic field intensity H and magnetic flux density B can be related by $B = \mu H = \mu_0 \mu_r H$, where μ is the magnetic permeability of corresponding material, which can be written as the product of vacuum permeability μ_0 and relative permeability μ_r. If we approximate $\mu_{r,g} = 1$ for air, and $\mu_{r,c}$ is constant for the core (i.e., ignoring nonlinearity in B-H relationship), then we have

$$\begin{aligned} B_c &= \mu_0 \mu_{r,c} H_c = \mu_c H_c \\ B_g &= \mu_0 \mu_{r,g} H_g = \mu_0 H_g \end{aligned} \tag{2.5}$$

Using (2.5), equations (2.2) and (2.4) can be combined and rewritten into

$$\Phi = \frac{NI}{\frac{l_c}{\mu_c A_c} + \frac{2l_g}{\mu_0 A_g}} \tag{2.6}$$

which can be also written in a more general form as

$$\Phi = \frac{\mathcal{F}}{\mathcal{R}_c + \mathcal{R}_g} = \frac{\mathcal{F}}{\mathcal{R}} \tag{2.7}$$

where $\mathcal{F}$ and $\mathcal{R}$ are the total magnetomotive force and reluctance in the magnetic circuit, respectively.

To further simplify the relationship, by assuming the cross-sectional area of the core A_c and that of the air gap A_g are equal (i.e., ignoring flux fringing and leakage effects at the air gap), we have $B_c = B_g = B$, i.e., the magnetic flux densities are equal everywhere along the path. Then (2.6) can be simplified as

$$B = \frac{NI}{\frac{l_c}{\mu_c} + \frac{2l_g}{\mu_0}} \tag{2.8}$$

Given the fact that, for ferromagnetic material, $\mu_r \gg 1 \Rightarrow \frac{l_c}{\mu_c} = \frac{l_c}{\mu_r \mu_0} \ll \frac{2l_g}{\mu_0}$, then (2.8) can be simplified as

$$B = \frac{\mu_0 NI}{2l_g} \tag{2.9}$$

This equation gives a zeroth-order approximation for magnetic flux density in a reluctance actuator. For a more complex case where more elements (such as permanent magnets) are added or considered, (2.7) can be used to derive a more accurate expression $\Phi = \sum \mathcal{F} / \sum \mathcal{R}$.

In cases where permanent magnets are added to produce a bias flux, (2.2) can be modified into

$$H_c l_c + 2H_g l_g + H_m l_m = NI + H_{m,c} l_m \tag{2.10}$$

and the corresponding flux can be written as

$$\Phi = \frac{\mathcal{F}}{\mathcal{R}_c + \mathcal{R}_g + \mathcal{R}_m} = \frac{NI + H_{m,c} l_m}{\frac{l_c}{\mu_c A_c} + \frac{l_g}{\mu_0 A_g} + \frac{l_m}{\mu_m A_m}} \tag{2.11}$$

where the subscript $_m$ refers to permanent magnets and $H_{m,c}$ is the coercivity of the magnets.

Force calculation

The force exerted by the stator on the mover can be calculated by the integral of Maxwell's stress tensor **T**

$$\mathbf{F} = \oint_S \mathbf{T} \cdot \mathrm{d}\mathbf{S} \tag{2.12}$$

$$= \frac{1}{2\mu_0} \oint_S B_n^2 \mathrm{d}S \tag{2.13}$$

By selecting the outer contour of the mover as the integration path S, the total force can be expressed as

$$F = \frac{B^2 A_{p,\mathrm{tot}}}{2\mu_0} = \frac{B^2 A_p}{\mu_0} \tag{2.14}$$

with the direction of force being attractive towards the stator core. $A_{p,\mathrm{tot}}$ is the total pole area of the stator and $A_p = A_{p,\mathrm{tot}}/2$ the area of a single pole.

For the case where no permanent magnets are used, applying (2.9) in (2.14), one gets

$$F = \frac{\mu_0 n^2 I^2 A_p}{4{l_g}^2} \tag{2.15}$$

This equation provides a zeroth-order approximation for the force generated by a reluctance actuator, and it shows the relation between force and current being $F \propto I^2$ and the relation between force and air gap being $F \propto 1/{l_g}^2$. They indicate the nonlinearity and negative stiffness present in the basic physics of reluctance actuators.

2.1.3. Nonlinearity

Based on the analysis in the previous section as well as the presence of some other magnetic effects, some important nonlinear effects to be considered in the design and analysis of reluctance actuators are discussed below. This section is generally formed by summarising section 2.3 from [4] and section 2.4 from [3].

Current-flux-force relation

Equations (2.14) (2.15) show a quadratic relation of force with current or flux, $F \propto B^2 \propto I^2$. Such a nonlinear relationship has a few indications. Firstly, a given reluctance actuator will have a varying and current-dependent motor constant K_I. Secondly, the generated force will always be uni-directional regardless of the direction of current or flux. This might also put some extra challenge on the control of current around the neutral point. Furthermore, $\dot{F} \propto I\dot{I} \propto B\dot{B}$ means that at the point where I or B are zero or close to zero, the required $\dot{I}$ or $\dot{B}$ to generate a nonzero $\dot{F}$ will be extremely large, thus some bias current or flux would become necessary for lowering hardware requirements.

Force-position relation and negative stiffness

Equation (2.15) also shows an inverse-quadratic relation between force and gap size, $F \propto 1/{l_g}^2$. Hence we have $\mathrm{d}F/\mathrm{d}l_g \propto -1/{l_g}^3$. This means a given reluctance actuator will have a negative stiffness which is also rapidly varying with the change of l_g. As a result, any force disturbance might cause a significant unexpected change in the actuator model as well as the motor constant. Note that this effect is not present in a Lorentz actuator which theoretically has zero stiffness in the direction of force. Therefore, more control efforts would be required to obtain a comparable performance with a well-optimised Lorentz actuator.

Magnetic hysteresis
In the calculation above we assumed a linear relationship between B and H. However, for ferromagnetic materials, magnetic hysteresis and saturation effects exist and will cause a nonlinear B-H relationship if H goes out of the linear range. Figure 2.3 shows a typical B-H curve for ferromagnetic materials. Such an effect could cause additional delays in the control loop and limit the control bandwidth, which might be compensated by applying an inverse model of the hysteresis loop.

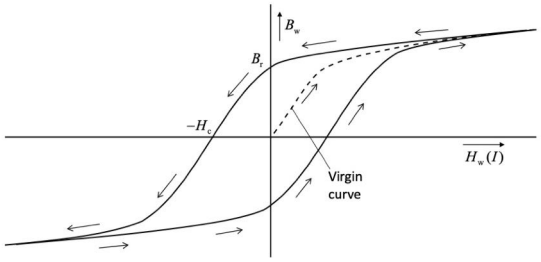

Figure 2.3: B-H curve demonstrating the magnetic hysteresis effect. [6]

Flux fringing and leakage
Flux fringing refers to the phenomenon that the magnetic flux fringes out while passing through a low-permeability medium (such as air), causing the actual effective air gap area to be greater and the corresponding local flux density to be less than the ideal case. Flux leakage refers to the phenomenon that a portion of magnetic flux takes a path that deviates from the intended path, and "leaks" out of the magnetic circuit. As a result, the effective or useful flux within the circuit becomes less. Moreover, the scale of flux fringing and leakage are dependent on the gap size [4], adding a secondary gap-dependent effect to the ideally gap-independent force-flux relation (2.14).

Eddy current
According to Faraday's law and Lenz's law, the varying magnetic field within the actuator core will induce loops of electric current named eddy currents, which will then create a magnetic field that counteracts the original magnetic field. This effect, if not modelled accurately, might have an unexpected influence on actuator performance. Furthermore, the energy of eddy current will dissipate as heat which might further cause other effects.

Other effects
Losses due to coil resistance as well as effects mentioned above, such as hysteresis loss and eddy current loss, will be dissipated mostly in the form of heat. Dissipated power might then cause thermal expansion and influence certain properties of the core and sensors, which will finally affect the performance of the actuator.

Besides, a "loop-widening phenomenon" was also discovered in previous research [4], which refers to the observed phase lag of the measured flux by the sense coil with respect to the measured current. The effect shows up from <10 Hz frequencies and the phase lag increases with frequency, but [4] was not able to conclude a cause for this phenomenon. It can be expected that this extra delay in the loop will add extra challenges for realising a fast and accurate control.

The presence of these nonlinear effects makes it more challenging to realise accurate and high-bandwidth control using standard control methods. In the next section, state-of-the-art approaches and techniques for the linearisation of reluctance actuators are reviewed and discussed.

2.2. Literature Review: Linearisation of Reluctance Actuators

Given the intrinsic nonlinearity within reluctance actuators discussed above, to achieve a high-accuracy control that is comparable with state-of-the-art solutions in the precision industry, proper approaches for linearising reluctance actuators are needed. This section generally summarises sections 2.4 and 2.5 in [4] to present some typical methods for improving the linearity of reluctance actuators.

2.2.1. Linearisation through Actuator Design

Bias current and flux

For a single-actuator configuration, a bias current I_0 of a certain portion of max current $I_{\max}$ can be fed through the driving coil. To make this the neutral state of the actuator, a bias force on the mover (such as gravity) is also needed to balance the force created by I_0. As a result, the working point of the actuator is taken from around $I = 0$ to around $I = I_0$, where the force-current relationship is relatively more linear (lower curvature of the curve $F(I)$), and the force error due to the linearisation of the $F \propto I^2$ relationship would be reduced. Besides, in this way, forces in both attractive and repulsive directions can be produced, and the small current range around $I = 0$ can be avoided, where a large or even infinite current slew rate is required to produce a non-zero force rate.

Alternative to biasing the current, permanent magnets can be used to produce a bias flux. Figure 2.4(a) shows a typical configuration for using a permanent magnet to produce a bias flux. This configuration can be modified by changing the flux path of the driving coil, such as the one used by [2] as shown in Figure 2.4(b). Two coils connected in series are installed on the outer path of the actuator, thus the flux generated by the coils will only flow through the outer path. As a result, the ability to generate bi-directional forces and a position-independent linear relation between force and flux can both be obtained.

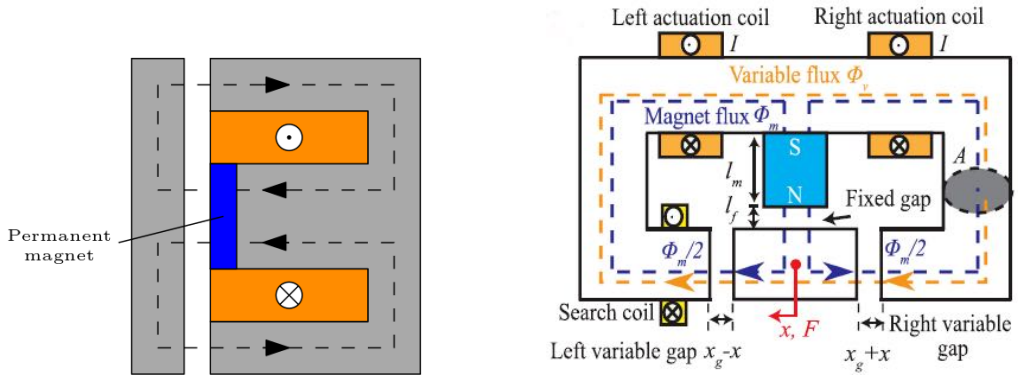

Figure 2.4: Flux-biased reluctance actuator (a) in E-I configuration and (b) in a modified form that is able to generate bi-direction forces and has a position-independent force-flux linearity in the direction of motion. [2]

Both bias current and bias flux produce a certain amount of magnetomotive force, thus they are expected to have similar effects in terms of improving linearity. Producing a bias flux using permanent magnets has the advantage of being more energy-efficient than biasing the current. However, flux generated by permanent magnets cannot be adjusted or removed on its own, as a result, the flux-biased actuator might have trouble reaching a zero-force neutral state.

Tuning of design variables

Based on equation (2.9) and (2.15), some design variables can be selected with special

considerations to reduce nonlinear effects. For example, a larger operating air gap would result in a higher linearity for reluctance actuators.

Lamination

By making the stator and mover core out of thin lamination with non-conductive bonding material in between, where the direction of lamination is perpendicular to the flux path, eddy currents will be constrained within each lamination layer and the overall scale and effect of eddy currents can thus be greatly reduced.

Core material selection

By selecting materials with a higher saturation flux density B_{sat} or with a greater range of B in the linear region, the effect of magnetic hysteresis and saturation can be reduced up to a higher B level, thus a higher actuator performance can be achieved.

2.2.2. Linearisation through Feedback Control and Calibration

Section 2.2.1 already provides design techniques for reluctance actuators with less amount of nonlinear effects in the first place. However, to further compensate for the remaining nonlinear effects as well as the negative stiffness, an active control with certain techniques would be needed.

Depending on the choice of control variables, two control modes are commonly used in the literature for reluctance actuators. Current feedback control, though being a commonly used and easy-to-implement control method for electromagnetic actuators, is greatly limited by the intrinsic nonlinear effects of reluctance actuators that lie in the current-flux relationship, which cannot be captured by the current feedback signal and compensated by the feedback loop [2][4]n. This poses a great challenge in reaching a high precision using current control on reluctance actuators. To tackle this, several techniques are developed to linearise the actuator for better current control performance, such as nonlinear compensation [7][8][9] and hysteresis modelling [9].

As a promising alternative, flux feedback control is able to capture and reject the influence of the air gap dependency and hysteresis effect [2], which are the main error sources in the current mode [10], by measuring and controlling the flux directly. However, accurate sensing of magnetic flux over a wide frequency range turns out to be more challenging than current sensing, which can become a major limiting factor for implementing the flux control.

Some nonlinear effects, such as the current-flux-force relation, can also be compensated by experimentally calibrating the actuator to obtain the current-flux-force mapping, from which a look-up table can be made and applied on the feedforward path to linearise the actuator. Alternatively, a parametric model can be fitted to the calibration data to generate an inverse plant for compensation.

The rest of this chapter is organised as follows. Firstly, section 2.2.2.1 and section 2.2.2.2 review the implementation of the current mode and flux mode control respectively. Then section 2.2.2.3 focuses on the comparison between the two control modes through simulation and experiments. Finally, findings and corresponding proposals will be summarised at the end of the chapter in section 2.4.

2.2.2.1 Current Control

Basic form

The basic form of a current-feedback control loop is shown in Figure 2.5. If a desired force F_d is given as the reference, then the $B(F)$ and $I(B)$ relations need to be modelled to convert the force reference into current reference. However, the great complexity and nonlinearity of the $B(F)$ and $I(B)$ relations, especially the latter which includes the hysteresis effect, makes accurate modelling a great challenge [4]. Various techniques are applied in the literature to improve the achieved performance of this control mode.

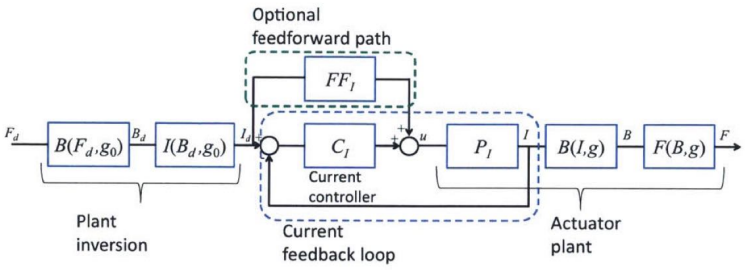

Figure 2.5: Block diagram of the basic form of current control for reluctance actuators. [4]

Nonlinear compensation

Although the standard feedback control serves to linearise the actuator to a certain degree, some other major nonlinear effects, such as hysteresis and gap-dependency in the current-flux relation, are left unattended outside of the current feedback loop [2], leading to the variation of the plant gain which weakens the benefits brought by the current-based feedback linearisation. To tackle this, an additional block that compensates for the nonlinearity in the force-to-current relation can be designed and implemented, which is named "Nonlinear Compensation (NLC)" in the literature. In Figure 2.6, the basic working principle of nonlinear compensation is demonstrated by implementing the inverse of the current-force relation (2.15) with position feedback. Comparing to a simple input conversion shown in Figure 2.5, the control scheme with NLC takes the change of the position as well as the quadratic current-force relation into consideration, so that the actuator is more effectively linearised with a greater working range and a lower mechanical stiffness [7].

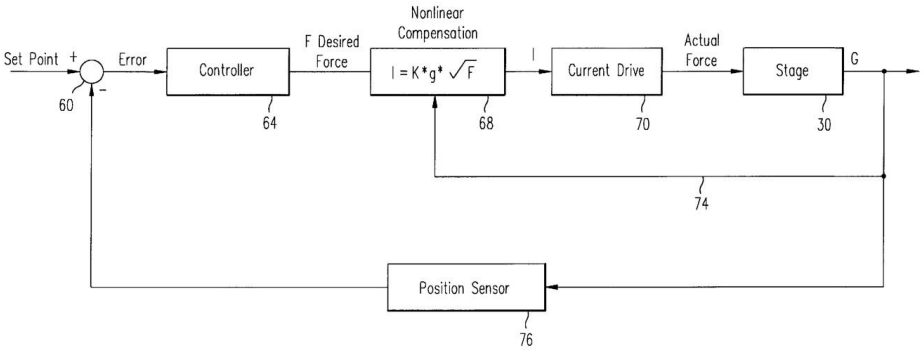

Figure 2.6: Basic structure of nonlinear compensation for reluctance actuators. [11]

A more accurate approach would be using actual measurement data to fit into a more complex yet invertible $F(I, l_g)$ analytical model, such as a polynomial function, or build a look-up table to relate force F, current I and gap size l_g for nonlinear compensation. In [7], the compensated actuator

stiffness with a non-compensated actuator with standard $I_{\max}/2$ bias are compared. It is found that nonlinear compensation using a simple model $F = k\left(I^2/{l_g}^2\right)$ could decrease the stiffness by at least 6.2 times, which improves to 21 times when a more advanced polynomial model with 5 additional terms is used. However, the effect of this nonlinear compensation scheme would still be limited by uncertainties caused by the hysteresis effect, in addition to modelling, fitting, and measurement errors.

Alternative to the model-based linearisation discussed above, nonlinear compensation can also be carried out using experimental data. In [8], a look-up table (LUT) based on calibration data is used for nonlinear inversion. Firstly, a nonlinear polynomial model characterising the force-current-gap relationship is developed based on calibration data. Then a 2D LUT is created that maps the force input F and position feedback x to the desired current I. This approach using LUT can be more computationally efficient than other model- or function-based inversion methods.

To achieve a more effective nonlinear compensation that also considers the hysteresis effect, an invertible hysteresis model for the I-B relation can be made, and its inverse can be applied in the nonlinear compensation block, to make a more accurate and realistic current-force conversion. In [9], a current-controlled reluctance actuator is linearised using an inverse parametric hysteresis operator derived based on the Duhem model. In addition, a measurement-based look-up table is used to model the remaining nonlinear effects between force and current. These two steps are connected using an intermediate variable, and serve together as a feedforward compensator to linearise the actuator. As a result, for a 400 N actuator, a force predictability greater than 99.95 % is achieved, a 10-times improvement over the case using only a polynomial model for nonlinear compensation without considering the hysteresis effect. However, as mentioned in [9], an accurate air gap control or measurement with up to 10 nm precision is required to achieve the results above. The presence of air gap dependency in the current-force relationship makes the performance of the current-based control strongly rely on an accurate gap measurement, which is an unavoidable limitation for the current control.

Other control techniques

Other control techniques for improving the current mode performance are also discovered, such as gain scheduling [12] in which controller gains are adjusted based on operating points of the actuator, and iterative learning control [13] in which the control input is repeatedly updated by learning the system response in the previous repetition. However, due to their complexity and the fact that a superior control design is not the focus of this project, these control methods will not be discussed here.

2.2.2.2 Flux Control

Basic form

The general form of the flux-mode control for reluctance actuators is shown in Figure 2.7. Compared with the current mode Figure 2.5, the main differences would be that the control variable is now magnetic flux instead of current, and accordingly the current-flux conversion happens within the loop. This means the nonlinear effects that exist in the current-flux relationship, such as hysteresis and air gap dependency which need to be compensated with great efforts in the current mode, can now be captured and compensated by the flux feedback [2]. As a result, nonlinear compensation in the flux mode would only need to compensate for the remaining nonlinearity in the force-flux relationship, which is mainly flux fringing and leakage [4].

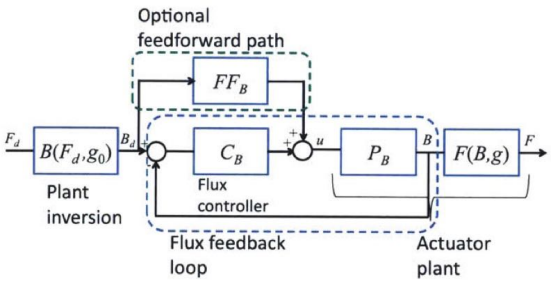

Figure 2.7: Block diagram of the basic form of flux control for reluctance actuators. [4]

Nonlinear compensation

Similar to the nonlinear compensation in the current mode as discussed in section 2.2.2.1. The inverse of the gap-independent flux-force relationship $F = B^2A/\mu_0$ would provide a simple model for inversion. However, the actual flux-force relation is still gap-dependent due to flux fringing and leakage, making it still helpful to measure or estimate gap size for a high performance. However, unlike the gap dependency in the current-flux relationship, this is only a secondary effect and will thus have much less influence on performance if not compensated properly [4].

In [4], a 2D look-up table (LUT) in the form $B(F, l_g)$ is generated from the force-flux-gap calibration data. It is used to generate the desired flux density B from the desired force F and the air gap size l_g.

Flux measurement

In recent literature concerning flux control, it is noticed that more focus has been put on realising an accurate flux sensing, instead of compensating the nonlinear force-flux relationship. Accurate sensing of magnetic flux in the air gap over a wide frequency range turns out to be more challenging than realising accurate current sensing, which has already been extensively studied and applied thanks to the broad use of Lorentz actuators [4].

Flux sensors, such as the Hall sensor and sense coil, are usually found to only provide optimal results in a certain frequency range. Thus, one can take advantage of the strength of different sensors by merging multiple sensors together to form a flux estimator. In [2], [3], and [4], hybrid flux sensor configurations are implemented by using a DC flux sensor mainly at low frequencies and an AC flux sensor mainly at high frequencies. Since the validation of flux measurement is considered a key contribution in this project and is reviewed in detail, it will be discussed below in section 2.3: Literature Review: Dynamic Measurement of Magnetic Flux.

2.2.2.3 Comparison between Current and Flux Control

In this section, the two control modes for reluctance actuators are compared. Methods used in the literature for quantifying control performances and enabling a fair comparison are reviewed, and their corresponding results are discussed.

In [1], simulation is carried out using basic control structure and linear controllers to validate the advantage of the flux control over current control. Results show that basic linear current control cannot keep the system stable throughout the designed motion range, while the standard

flux-mode control is found to be stable with a lower error. Furthermore, noise analysis also shows a slightly lower estimated noise in the flux mode compared to the current mode, which can be further decreased by merging multiple flux sensors to provide a better flux estimation. This validates the benefits of controlling the flux instead of current on the theoretical level.

In [3], both a current mode control with hysteresis compensation and a flux mode control using sense coil feedback are applied. To quantify their performances for comparison, force error for an injected force profile is measured in order to demonstrate force predictability. Meanwhile, the compensated actuator stiffness is calculated by measuring the force error while a certain gap disturbance is manually introduced. The same performance indicators are also used in [4], where the frequency response of the system $F_{\text{meas}}/F_{\text{in}}$ is also measured and analysed. It is shown that, while the reluctance controller being tested can only achieve a force predictability of no more than 90 % F_{max} using current-mode linear control, the force predictability can be improved to 99.5 % F_{max} by adding hysteresis compensation and polynomial nonlinear compensation, while the achieved stiffness is still as high as -200 kN/m at 100 N and 1 mm air gap. When the flux control scheme based on the Hall sensor and sense coil feedback is applied, actuator stiffness can be reduced to -2.5 kN/m with the same achievable force predictability of 99.5 % F_{max}. If a gap observer is added to modulate sensor and feedforward gain, the achieved stiffness can be further reduced to -500 kN/m, which is comparable to a Lorentz actuator with similar force capacity.

In [2], current-mode and flux-mode control with PI controllers are implemented on a hybrid reluctance actuator. To quantify the performance, actuator nonlinearity is measured by drawing a linear trend line in the reference-position plot and dividing the mapping error by the motion range. Besides, tracking error for a triangular scanning motion is also measured. Results show that measured tracking error and nonlinearity in the flux-controlled mode show a significant reduction compared with the current-controlled mode. For example, for a 30 µm and 60 Hz sinusoidal reference, the tracking error is reduced from >20 µm to <3 µm and the nonlinearity is reduced from 23 % to 5 %, by using flux mode control instead of current control.

2.3. Literature Review: Dynamic Measurement of Magnetic Flux

Accurate measurement of magnetic flux over a wide frequency range is one of the main challenges for implementing flux control on reluctance actuators. This chapter aims to review methods for accurately measuring static and dynamic flux on reluctance actuators. Section 2.3.1 provides an overview of typical magnetic sensors for reluctance actuators, then section 2.3.2 reviews methods for incorporating one or multiple sensors for flux estimation. Finally, findings and corresponding proposals will be summarised at the end of the chapter in section 2.4.

2.3.1. Magnetic Sensors Overview

In this section, typical types of flux sensors used on reluctance actuators are introduced. Their advantages and disadvantages for being used on reluctance actuators are discussed.

2.3.1.1 Hall sensor

A Hall sensor measures the magnitude of magnetic flux density using the Hall effect, which refers to the production of a voltage across a conductor in the presence of a magnetic field and an electric current that are perpendicular to each other, with a proportional relationship $V_H \propto I \cdot B$ [14]. Hall sensors are robust and relatively low-cost, while at the same time providing a direct and repeatable measurement of magnetic flux. However, there are a few drawbacks. Hall sensors suffer from a

greater temperature sensitivity compared to their alternatives, and their high-frequency performance is limited by the inferior noise characteristics [4]. Besides, their working principle requires them to be placed on the flux path, thus Hall sensors will either reduce available gap size (if placed in the air gap, Figure 2.8(a)) or create a low-permeability region in the iron core (if placed in the iron core), leading some researchers to refrain from using them [2]. Furthermore, the fact that they measure flux density at a single point makes their measurement more susceptible to local effects.

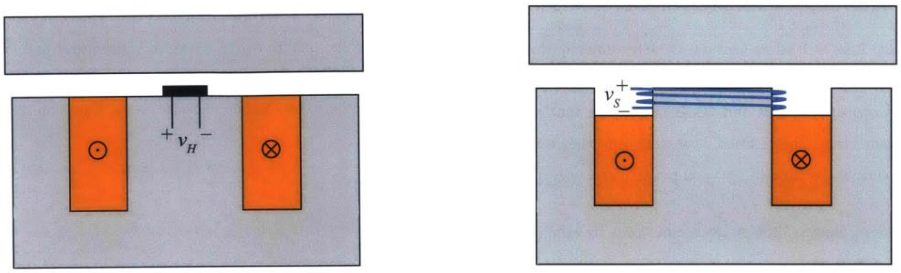

(a) (b)

Figure 2.8: Reluctance actuators with (a) a Hall sensor in the air gap and (b) a sense coil around the center pole. [4]

2.3.1.2 Sense coil (search coil)

A sense coil measures the rate of change of magnetic flux using Faraday's law

$$V_s = N\frac{\mathrm{d}\Phi}{\mathrm{d}t} \tag{2.16}$$

where V_s, Φ, and N are the generated voltage (i.e., electromotive force), the magnetic flux passing through the coil, and the number of coil windings respectively [15]. Thus by measuring the voltage across the coil, the rate of change of the total flux in the enclosed area can be known. Unlike the Hall sensor, a sense coil can be placed around one of the stator poles without taking space in the air gap as shown in Figure 2.8(b) [4]. It is also superior to the Hall sensor in high-frequency noise suppression, since the measured signal needs to be integrated to obtain flux measurement, which serves to suppress high-frequency noises [3]. However, noises at the low-frequency end will in turn be amplified and, more importantly, the fact that the sense coil is measuring the rate of change might result in drifting of magnetic flux B, since its DC component might slowly drift away without being noticed by observing $\mathrm{d}B/\mathrm{d}t$ [3].

2.3.1.3 Current sensor with model-based estimator

As discussed above, the working principle of Hall sensors makes it challenging to properly place them on reluctance actuators. This leads researchers to seek an alternative way of providing DC flux measurements. In [2], the measurement from a current sensor is used to provide an estimation of DC flux and replace the Hall sensor. Current signals are converted into flux signals by an estimator gain based on experimental data. In this way, similar functions to Hall sensors' can be realised with an alternative sensor that is much easier to install and operate. However, the accuracy of the flux estimator highly depends on the model used for I-B conversion, in which the presence of hysteresis is challenging to model accurately, and any simplification and model inaccuracy will result in estimation errors. In [4], a similar scheme is used for DC flux estimation, but additionally, a hysteresis model is applied while converting current measurement into flux estimation, providing a more accurate DC flux estimation that is able to capture some nonlinearity.

2.3.1.4 Hybrid configuration

Given the complementary characteristics of the flux sensors mentioned above, a hybrid measurement scheme can be designed to take advantage of the strengths of both sensors, by using one of the DC flux sensors (Hall sensor or current-based flux estimator) for low-frequency measurement and a sense coil for high-frequency measurement [4]. Practical implementation of this sensor configuration is carried out in [2], [3], and [4], and will be further discussed below.

However, while merging the signals from multiple sensors, differences in their working principle and measuring location could lead to some mismatch [4], which can be dependent on gap size, frequency, flux saturation level, etc., making signal merging more challenging.

2.3.2. Flux Estimation Schemes

In this section, methods of flux estimation are reviewed, which use or combine the above-mentioned flux sensors to produce an accurate flux measurement across a wide frequency range.

2.3.2.1 Complementary Filters

To take advantage of the complementary characteristics of DC and AC flux sensors, a flux estimator is designed in [2], which combines the DC flux estimation from a current sensor y_c and AC flux measurement from a sense coil y_s using complementary first-order filters (Figure 2.9). The cutoff frequency for the filters is set to 10 Hz based on measured noise PSD shown in Figure 2.10, which is where the two PSD curves intersect. As a result, the noise PSD of the merged signal is generally kept below both of the unmerged noise PSD. In the time domain, the noise of the merged signal is significantly reduced by over 6 times compared with the current sensor measurement, meanwhile no DC drift is observed in the merged signal. When this flux merging scheme is applied in a flux control loop, compensated actuator nonlinearity is reduced by 4.8 times, and tracking error is reduced by 19 times compared with the current-controlled actuator.

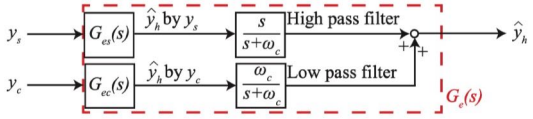

Figure 2.9: Block diagram of the flux estimator $G_e(s)$ using sensor fusion. [2]

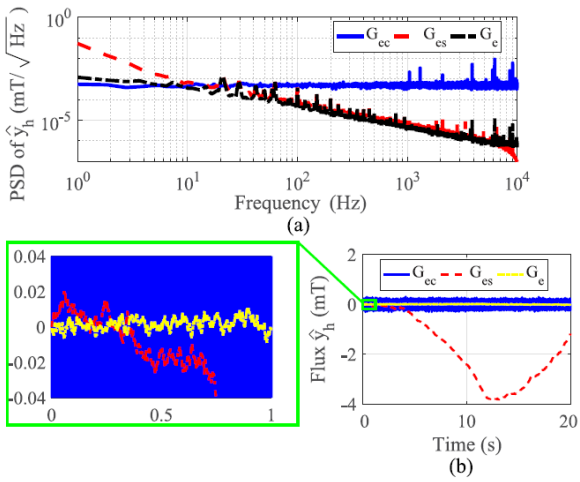

Figure 2.10: Comparison of noise in measured flux, measured by the current sensor G_{ec}, sense coil G_{es} and the merged flux estimator G_e: (a) PSD and (b) time-domain signals.

In [4], a similar design for the flux estimator is used, which combines a current sensor with a sense coil using high- and low-pass filters. For improvement, a hysteresis model is added to process the current signal so that the current sensor is now expected to also be able to capture the hysteresis effect and yield a closer result to Hall sensor outputs. Air gap measurement is also provided as another input to the hysteresis model. Furthermore, second-order low-pass and high-pass filters are used in order to obtain a zero DC gain when the high-pass filter is combined with an integrator $1/s$, which yields a combined transfer function of $\frac{s}{s^2+2s\omega_n+\omega_n^2}$ instead of $\frac{1}{s+\omega_n}$ when a first-order high-pass filter is used, so that any voltage offset from the sense coil will not result in a DC error in the merged signal. The corresponding low-pass filters can be derived using LPF $= 1 -$ HPF to keep a theoretically zero error in the merged signal. A cutoff frequency of 10 Hz is set for the complimentary filter pair.

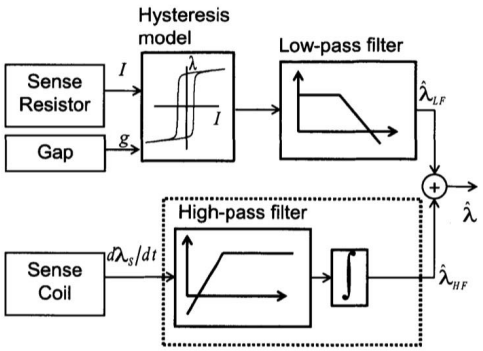

Figure 2.11: Complementary filter structure for estimating actuator flux, used in [4]

In [1], the combination of a sense coil with a Hall sensor, instead of a current-based flux estimator, is investigated. It is worth noting that, the merging of flux signals is demonstrated and applied in a different yet fundamentally equivalent way as Figure 2.11, as shown by the block diagram in Figure 2.12: The flux signal from the Hall sensor is used to compensate error in the merged signal by adding the integrated difference between Φ_{merge} and Φ_{Hall} to the flux signal from sense coil Φ_{sense}. A constant gain K_{merge} is chosen to determine the bandwidth of the compensating effect from the Hall sensor, so that the compensation from the Hall sensor will be increasingly dominated at lower frequencies and be more suppressed at frequencies higher than K_{merge}.

A noise analysis based on real measured sensor noise is also made in [1]. Results show that, compared with Hall sensor noise, noise from the sense coil has more than 10 times less influence on position, force and voltage outputs. This result alone indicates that using the sense coil alone without a Hall sensor would yield the best result, however, due to the DC drifting effect of the sense coil, a Hall sensor would still be needed in practice for low-frequency measurements.

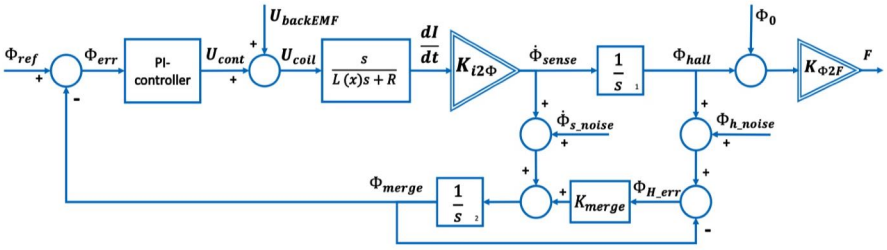

Figure 2.12: Block diagram from [1], showing an alternative form of the flux signal merging scheme as shown in Figure 2.9.

2.3.2.2 Cascade Control

In [3] a cascade control scheme is applied to incorporate a Hall sensor and a sense coil (Figure 2.13). For the inner loop, a sense coil is used for flux feedback with a high-bandwidth controller and direct voltage injection, and as a result small tracking errors at high frequencies can be achieved. To suppress drift caused by the measuring principle of the sense coil, an outer loop with Hall sensor flux feedback and a controller of 1.6 Hz bandwidth is used. The measured tracking error for 200 N second-order profiles is reduced to 0.05 N (0.025 %), compared with 0.1 N (0.05 %) for the case without Hall sensor feedback loop added.

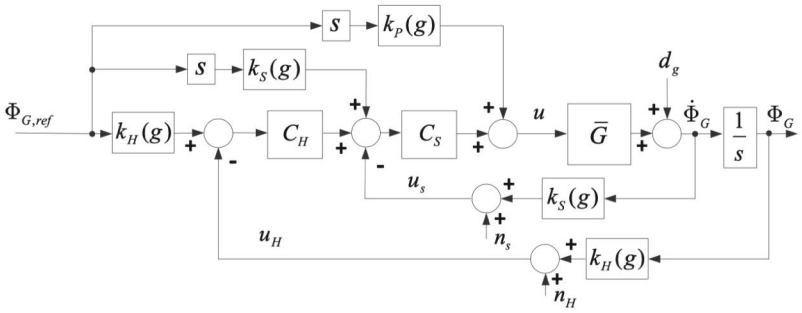

Figure 2.13: Generalized flux control based on the cascaded sensing coil and Hall probe feedback. [3]

However, it is noticed in [3] that the error becomes significant when the gap size deviates from the nominal value used in the scheme shown in Figure 2.13. To further reduce the mismatch between the two flux sensors, the gap dependency of the sensor gain k_H and k_S is compensated using an air gap observer, which includes a hysteresis model. The observer provides gap size estimation for adjusting k_H and k_S, using the current and flux measurement. As a result, the compensated stiffness of the actuator is reduced from -2.5 kN/m to under -500 N/m by adding the gap observer.

This merging scheme applies compensation from the Hall sensor in a similar way to the filter-based flux merging scheme introduced above in Figure 2.9 and Figure 2.12, and their block diagrams also

show similarities after transformation. However, if and how these two schemes are different in principle still needs further investigation.

2.4. Summary and Proposals

In this chapter, state-of-the-art techniques for the linearisation of reluctance actuators and introduced. While actuator design can be tuned and optimised for a more linear behaviour, however, further linearisation through actuator calibration and feedback control is still of great importance. It is noticed that, for current-based control the literature focuses more on nonlinear compensation, while for flux control more effort is put into the implementation of flux measurement. When their performances are compared, flux control is found to result in a lower tracking error as well as a lower actuator stiffness and nonlinearity than the current control. This validates the benefit of the flux control over current control for reluctance actuators.

Based on the insight obtained from the literature and the general objectives of the project defined above, the following schemes for feedback control and flux measurement on reluctance actuators are proposed, from which the main focus and contents of experimental measurements can be determined.

Current and flux feedback control

Look-up tables (LUTs) based on calibration data will be used for nonlinear compensation of both current and flux modes. For the current mode, the measured gap size is fed to the LUT, while for flux mode another way of estimating the gap using a look-up table $l_g(B, I)$ is proposed.

During experiments of this project, only the part from reference force to measured output force (shown in black in Figure 2.14 and 2.15) will be implemented, while the outer position loop (shown in gray in Figure 2.14 and 2.15) will not be realised.

Flux estimation scheme

Considering the results presented in the literature as well as the objectives of this project, it is proposed to use a Hall sensor and a sense coil as flux sensors in our experiments. A Hall sensor, placed in a machined slot at the top surface of one of the stator poles, is proposed for DC and low-frequency flux measurement instead of the current sensor, in order to study the feasibility of implementing Hall sensors without taking space in the air gap. Furthermore, 2nd-order high- and low-pass filters are proposed for signal processing and merging (Figure 2.15).

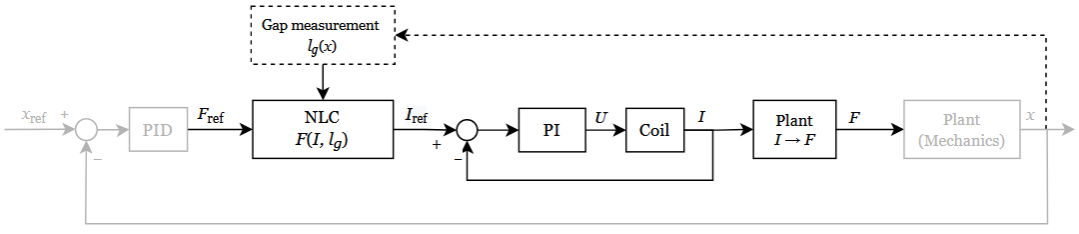

Figure 2.14: Proposed control design for the current mode.

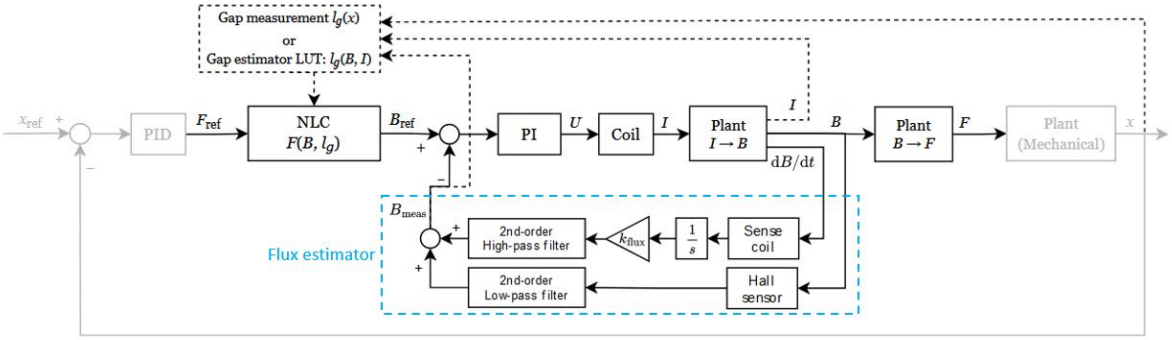

Figure 2.15: Proposed flux control loop and flux estimation scheme.

Proposed subjects for experiments

Based on the proposed schemes for feedback control and flux measurement, the following subjects are proposed for experimental measurements, as well as other relevant tests necessary for validating and evaluating the realised designs.

- **DC calibration of the actuator**
  The mapping between current, flux, gap size, and force are measured, so that look-up tables $F(I, l_g)$ and $F(B, l_g)$ are obtained for nonlinear compensation (NLC).

- **AC calibration of flux sensors**
  The ratio of flux outputs from the Hall sensor and the sense coil $k_{\text{flux}} = B_{\text{Hall}}/B_{\text{sense}}$ is measured, for matching and merging flux signals.

- **Frequency responses of the actuator**
  Various frequency responses, such as from the driving coil current I_{coil} to flux measurements B_{Hall}, B_{sense} and force output F, are measured to characterise actuator performance and validate the hybrid flux measuring scheme.

The corresponding details and results will be covered in chapter 5: Calibration and Measurements of the Designed Reluctance Actuator.

3

Design and Realisation of a Reluctance Actuator Prototype

3.1. Requirements

In this section, a set of system-level requirements is given to specify the desired performance of the whole system, from which some detailed actuator-level requirements are derived to characterise each actuator.

3.1.1. System Requirements

A set of system-level requirements are given (Table 4.1), where the maximum required acceleration is derived based on making 2 mm steps (3rd order profile) at the rate 100 steps/sec, and the stage weight and number of actuators are assumed referring to a typical system.

Table 3.1: System-level requirements

Parameter	Symbol	Unit	Original Value	Scaled-down Value
Total stage weight	$m_{\text{stage, tot}}$	kg	40	10
Max. required acceleration	a_{max}	m/s^2	87	87
Max. required force	$F_{\text{max, tot}}$	N	3480	870
Number of actuators	n_{act}	1	2	2
Stage weight per actuator	m_{stage}	kg	20	5
Max. required force per actuator	F_{max}	N	1740	435
Stroke of the stage	x_{var}	mm	1.5	1.5

To make the design more feasible and the setup easier to manipulate, the assumed total stage weight is scaled down, and other requirements are updated accordingly as shown in Table 3.2. As a result, the downscaled maximum required force output from a single actuator is $F_{\text{max}} = m_{\text{stage}} a_{\text{max}} = 435\,\text{N}$.

3.1.2. Actuator Requirements

Actuator-level requirements derived from system-level requirements are listed in Table 3.2. The meaning and derivation of some parameters are explained below.

Table 3.2: Actuator-level requirements

Parameter	Symbol	Unit	Value
Peak acceleration	a_{peak}	$\mathrm{m/s^2}$	87
Peak force	F_{peak}	N	500
RMS force	F_{rms}	N	354
Min. residual force	F_{min}	N	65
Peak force slew rate	$(\mathrm{d}F/\mathrm{d}t)_{\mathrm{peak}}$	N/ms	500
Actuator stroke	x_{var}	mm	1.50
Nominal gap size	x_{nom}	mm	0.90
Min. gap size	x_{min}	mm	0.15
Max. gap size	x_{max}	mm	1.65
End-of-stroke distance	x_{eos}	mm	0.15
Min. start-up gap size	x_{sMin}	mm	0
Max. start-up gap size	x_{sMax}	mm	1.80

For a better generality of results as well as a higher energy efficiency, hybrid reluctance actuators that use permanent magnets to generate a bias flux are studied. For this actuator type, the force generated by a single actuator can never reach zero, due to the flux mismatch between the magnets and the coil caused by flux leakage. As a first-iteration estimation, based on practical experience, the minimum residual force produced by a single actuator F_{min} is estimated using the relation

$$F_{\mathrm{min}} = 15\,\% \cdot F_{\mathrm{max}}\,. \tag{3.1}$$

If further FEM validation proves this to be an underestimation, a second iteration of the calculation might be needed to keep the following calculations remain valid and make sure the peak force generated by the system satisfies the requirement.

Then the peak force produced by a single actuator F_{peak} is calculated as

$$F_{\mathrm{peak}} = F_{\mathrm{max}} + F_{\mathrm{min}}\,, \tag{3.2}$$

and then the root-mean-square force is assumed to be

$$F_{\mathrm{rms}} = F_{\mathrm{peak}}/\sqrt{2}\,. \tag{3.3}$$

Furthermore, the desired peak slew rate of the force output $(\mathrm{d}F/\mathrm{d}t)_{\mathrm{max}}$ is determined based on the peak force of 500 N and the jerk time of 1 ms. However, this highly depends on the capability of the power amplifier used for driving the actuator, and therefore is not used to determine or evaluate the actuator design.

For requirements regarding the gap size, after defining the stroke x_{var} and nominal gap size x_{nom} of the actuator, the maximum and minimum gap sizes are calculated as

$$x_{\mathrm{max}} = x_{\mathrm{nom}} + \frac{1}{2}x_{\mathrm{var}}\,, \quad x_{\mathrm{min}} = x_{\mathrm{nom}} - \frac{1}{2}x_{\mathrm{var}}\,. \tag{3.4}$$

After defining the end-of-stroke distance x_{eos}, which specifies the allowed margin for the motion of the mover at the maximum and minimum gap sizes, the maximum and minimum start-up gap sizes are calculated as

$$x_{\mathrm{sMax}} = x_{\mathrm{max}} + x_{\mathrm{eos}}\,, \quad x_{\mathrm{sMin}} = x_{\mathrm{min}} - x_{\mathrm{eos}}\,. \tag{3.5}$$

3.1.3. Other Parameters and Considerations

Other relevant specifications in addition to those mentioned above that are also important for dimensioning calculation are listed in Table 3.3. They are determined conservatively based on practical experience.

Table 3.3: Other limitations and requirements needed for calculation

Parameter	Symbol	Unit	Value
RMS flux density	B_{rms}	T	0.50
RMS current density in driving coil	J_{rms}	A/mm^2	3.5
Peak current density in driving coil	J_{peak}	A/mm^2	4.9
Max. temperature for permanent magnet	$T_{\text{max,PM}}$	°C	60
Max. temperature for iron core	$T_{\text{max, core}}$	°C	80
Fill factor for driving coil	η_{fill}	1	0.6
Fill factor for iron core	η_{core}	1	0.9

3.2. Conceptual Design

In this section, the general procedure for the conceptual design of the reluctance actuator is described, which includes the dimensioning of the stator core and the driving coil, followed by the selection of parameters for the driving coil. For the first iteration, many parameters are given based on practical experience, and the resulting design will be iterated if found to not satisfy the requirements. Further optimisation is not carried out as long as the design satisfies the requirements, as performance improvement is not one of the design objectives, nor will it help the validation of flux control that will be carried out later.

3.2.1. Actuator Configuration

Basic construction and typical configurations were introduced in section 2.1.1. For this project, the E-I configuration is chosen over C-I, since it uses the spaces between the poles and the thickness of the mover more efficiently. Furthermore, an E-shaped core is easier for implementing a hybrid reluctance actuator design, since permanent magnets and a Hall sensor can be installed on the center pole without introducing any asymmetry. As a result, the E-I configuration with permanent magnets installed on the center pole is selected for this prototype design, as illustrated in Figure 3.1.

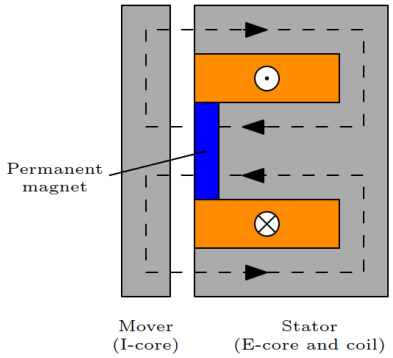

Figure 3.1: Reluctance actuator configuration proposed for this prototype design, with permanent magnets installed on the center pole of the stator core.

3.2.2. Dimension Calculation

For a reluctance actuator with the E-I configuration, based on the requirements and specifications provided in section 3.1 and theoretical relations derived in section 2.1 (with minor adaptations for different core shapes), a set of quick calculations and analyses are carried out to make a first-iteration conceptual design of the desired actuator, before detailed design and validation are carried out to determine if any further iteration is needed with modified parameters.

Core dimensioning

The area of the central pole face is calculated as

$$A_{\text{pole}} = \frac{F_{\text{nom}}\mu_0}{B_{\text{rms}}^2} = w_{\text{pole}} d_{\text{E}} \tag{3.6}$$

where w_{pole} and d_{E} are the width of the center pole (as indicated in Figure 3.2) and the depth of the E-core (perpendicular to the cross-section shown in Figure 3.2), respectively. By considering w_{pole} as a design variable, and defining the height-to-width ratio of the pole to a fixed ratio, the general dimension of the E-core can be determined.

Coil dimensioning

The required cross-sectional area of the main coil is determined based on the following limiting cases:

- At maximum air gap x_{max}, force output under root-mean-square current density J_{rms} should be no less than F_{rms}.
- At maximum air gap x_{max}, force output under peak current density J_{peak} should be no less than F_{peak}.
- To enable the coil to counteract the permanent magnet and produce the lowest possible net force, the magnetomotive force generated by the coil under root-mean-square current density J_{rms} should be no less than the maximum magnetomotive force from the magnet $\mathcal{F}_{\text{PM, max}}$.
- At maximum start-up air gap x_{sMax}, force output under root-mean-square current density J_{rms} should be greater than the residual force produced by the actuator on the opposite side.

The corresponding coil area calculated from those 4 cases are compared and the greatest value is assigned to be the final coil area A_{coil}.

For a certain cross-sectional area A_{coil}, a shape factor describing the height-width ratio $\eta_{\text{shape, coil}} = h_{\text{coil}}/w_{\text{coil}}$ is needed to determine the coil dimension. For the first iteration, a common height-width ratio $\eta_{\text{shape, coil}} = 3.0$ is chosen as the initial value. Then the height and width of the coil can be solved as

$$w_{\text{coil}} = \sqrt{A_{\text{coil}}/\eta_{\text{shape, coil}}}, \quad h_{\text{coil}} = \eta_{\text{shape, coil}} w_{\text{coil}} \tag{3.7}$$

Permanent magnets

As stated in section 3.2.1, permanent magnets will be incorporated in the actuator as shown in Figure 3.1 for creating a bias flux. Neodymium magnets (NdFeB) with grade N42SH are chosen due to their high coercivity and good availability. The maximum allowed temperature for the magnets during operation is set to 60 °C, although the magnet itself can resist much higher temperatures, to limit the degradation of performance (coercivity H_c, remanence B_r, etc.) when temperature increases. Using the data for H_c and B_r at room temperature, and the corresponding temperature coefficients α_H and α_B, the coercivity and remanence of the magnet at any given temperature can be estimated. This allows us to calculate the permeability of the permanent magnet μ_{PM}, and thus the reluctance $\mathcal{R}_{\text{PM}}$, at any given temperature.

Then, the required thickness of the permanent magnet t_{PM} can be calculated by solving the following equation system.

$$\begin{aligned} \mathcal{F}_{\mathrm{PM}} &= H_{\mathrm{c}} t_{\mathrm{PM}} \\ \mathcal{F}_{\mathrm{PM}} &= B_{\mathrm{bias}} A_{\mathrm{pole}} \mathcal{R}_{\mathrm{nom}} \\ \mathcal{R}_{\mathrm{nom}} &= \mathcal{R}_{\mathrm{gap,nom}} + \frac{t_{\mathrm{PM}}}{\mu_0 \mu_{\mathrm{PM}} A_{\mathrm{pole}}} \end{aligned} \tag{3.8}$$

The term $\mathcal{R}_{\mathrm{gap,nom}}$ in the equation represents the reluctance of the air gap at the nominal gap size, and can be expressed as

$$\mathcal{R}_{\mathrm{gap,nom}} = \frac{2x_{\mathrm{nom}} + t_{\mathrm{safe}}}{\mu_0 A_{\mathrm{pole}}}, \tag{3.9}$$

where t_{safe} is an extra air gap kept next to the permanent magnet to prevent mechanical contact or collision with other parts.

Here, in the first iteration, the bias flux density provided by the permanent magnet B_{bias} is set to a certain value so that the corresponding bias force satisfies $F_{\mathrm{bias}} = (1/4)F_{\mathrm{peak}}$. Then the thickness of the permanent magnet can be calculated with (3.8).

Dimensioning results

The calculation procedure shown above is implemented, and parameters are tuned in several iterations to reach a desired state. A set of actuator dimensions and specifications is finally obtained as shown in Table 3.4 and Figure 3.2.

Table 3.4: Dimensions of the core and the driving coil

Parameter	Symbol	Unit	Value
Width of E-core	w_{E}	mm	69.4
Height of E-core	h_{E}	mm	50.0
Depth of E-core (with isolation)	d_{E}	mm	91.0
Width of central pole	w_{pole}	mm	20
Area of central pole	A_{pole}	mm^2	1820
Mass of E-core	m_{E}	kg	1.59
Mass of I-core	m_{I}	kg	0.36
Coil width	w_{coil}	mm	12.8
Coil height	h_{coil}	mm	37.8
Magnet thickness	t_{PM}	mm	1.3

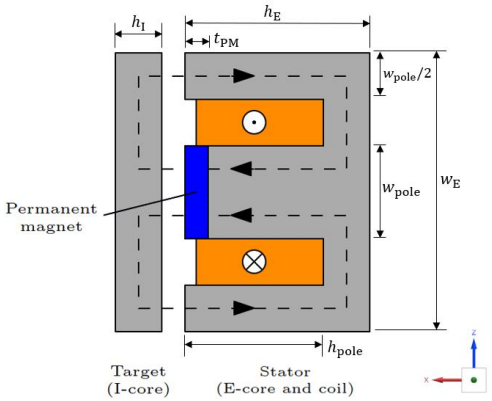

Figure 3.2: Reluctance actuator configuration proposed for this prototype design, with labels for dimension parameters.

3.2.3. Coil Windings

As the first iteration, a typical value can be chosen for the wire diameter of the driving coil d_{wire}. Then the number of turns required for the coil is calculated as

$$n_{\text{turns}} = \left\lfloor \frac{A_{\text{coil}} J_{\text{rms}} \eta_{\text{fill}}}{i_{\text{rms}}} \right\rfloor = \left\lfloor \frac{A_{\text{coil}} \eta_{\text{fill}}}{A_{\text{wire}}} \right\rfloor \tag{3.10}$$

To validate the feasibility of the chosen design parameters for the coil, i.e., to check if it is possible to fit a coil with wire diameter d_{wire} and turn number n_{turns} into a $w_{\text{coil}} \times h_{\text{coil}}$ area, a MATLAB script is used to implement the orthocyclic winding and calculate the maximum number of turns that could fit into the given area (Figure 3.3(a)). This maximum turn number needs to be no less than the desired value n_{turns} to make the corresponding wire diameter d_{wire} feasible (i.e., able to generate the desired current density J_{rms}).

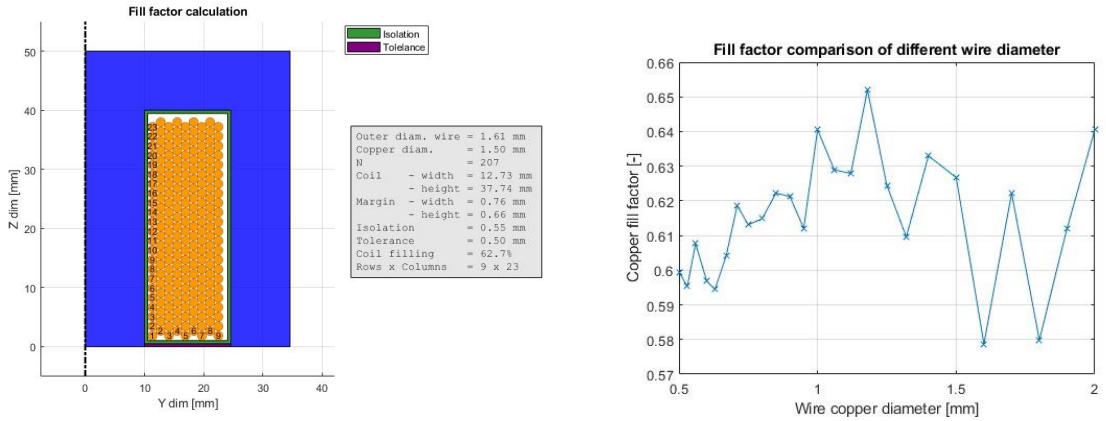

(a) (b)

Figure 3.3: Coil winding calculation using MATLAB scripts: (a) simulation of orthocyclic winding of the coil, and (b) fill factor comparison of different wire diameters for the driving coil.

Furthermore, the corresponding fill factor (conductor area over the total area on a cross-section) can be calculated, and compared with the fill factor when a different wire diameter is applied (Figure 3.3(b)). This way, one can choose to use the wire size which provides a higher fill factor, or improve the fill factor by slightly altering the wire diameter.

Using the described procedure above, the design of the coil can be optimised in a few iterations, and finally the copper wire with conductor diameter of $d_{\text{wire}} = 1.5\,\text{mm}$ is selected, with corresponding specifications shown in Table 3.5 and Figure 3.4.

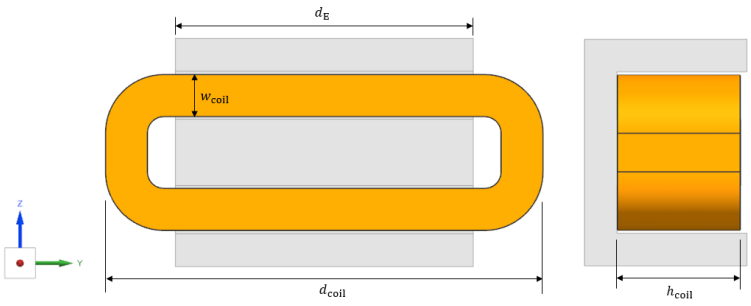

Figure 3.4: Design for the driving coil with labels for dimension parameters.

Table 3.5: Calculated coil specifications

Parameter	Symbol	Unit	Value
Coil width	w_{coil}	mm	12.8
Coil height	h_{coil}	mm	37.8
Coil cross-sectional area	A_{coil}	mm^2	484
Conductor diameter	d_{wire}	mm	1.50
Conductor cross-sectional area	A_{wire}	mm^2	1.77
Wire total length	l_{wire}	m	63
Coil resistance	R_{coil}	Ω	0.61
Max. coil inductance	$L_{\text{coil, max}}$	mH	42
Number of turns	n_{turns}	1	203
Coil mass	m_{coil}	kg	1.02

Slew rate analysis

According to the determined coil specifications in Table 3.5, the required current slew rate and voltage input for achieving the desired force slew rate of $(\mathrm{d}F/\mathrm{d}t)_{\text{peak}} = 500\,\text{N}$ can be calculated.

Given the flux-current relation $BA_{\text{pole}} = n_{\text{turns}}I/\mathcal{R}$, the current slew rate can be expressed as

$$\frac{\mathrm{d}I}{\mathrm{d}t} = \frac{A_{\text{pole}}\mathcal{R}}{n_{\text{turns}}}\frac{\mathrm{d}B}{\mathrm{d}t}. \tag{3.11}$$

Meanwhile, according to the force-flux relation $F = B^2A_{\text{pole}}/\mu_0$, the force slew rate can be expressed as

$$\frac{\mathrm{d}F}{\mathrm{d}t} = \frac{2BA_{\text{pole}}}{\mu_0}\frac{\mathrm{d}B}{\mathrm{d}t}. \tag{3.12}$$

Combining (3.11) with (3.12), we get

$$\frac{\mathrm{d}I}{\mathrm{d}t} = \frac{\mu_0\mathcal{R}}{2n_{\text{turns}}B}\frac{\mathrm{d}F}{\mathrm{d}t}, \tag{3.13}$$

and the corresponding required voltage input for achieving this current slew rate is given by

$$V_{\text{in}} = V_R + V_L = IR + L\frac{\mathrm{d}I}{\mathrm{d}t} = IR + \frac{\mu_0 n_{\text{turns}}}{2B}\frac{\mathrm{d}F}{\mathrm{d}t}, \tag{3.14}$$

where V_R and V_L are resistive voltage and inductive voltage, and $L = {n_{\text{turns}}}^2/\mathcal{R}$ is the inductance of the actuator. From (3.13) and (3.14) it can be seen that both the required current slew rate $\mathrm{d}I/\mathrm{d}t$ and the induced voltage V_{in} depend on the generated flux in the actuator core B which can be related to the force output F. By applying the relation $B(F)$ in (3.13) and (3.14), the relations between the required current slew rate and the induced voltage for maintaining the required force slew rate of 500 N/ms can be plotted as shown in Figure 3.5. As a result, the induced voltage V_L reaches up to 319 V and in order to compensate for this induced voltage while driving the coil, a total voltage input $V_{\text{in}} = V_R + V_L$ of up to 325 V would be required (in which the resistive voltage $V_R = IR$ is estimated using the maximum allowed current of 8.7 A and the estimated coil resistance of 0.61).

A potential way to reduce the maximum required V_L would be to reduce the number of turns n_{turns} for the driving coil. As a result, the wire diameter of the driving coil needs to be increased to achieve the same current density which is specified as a design requirement. This has already been taken

into consideration during the coil design, and as a result the copper wire with a relatively large diameter of 1.50 mm was chosen.

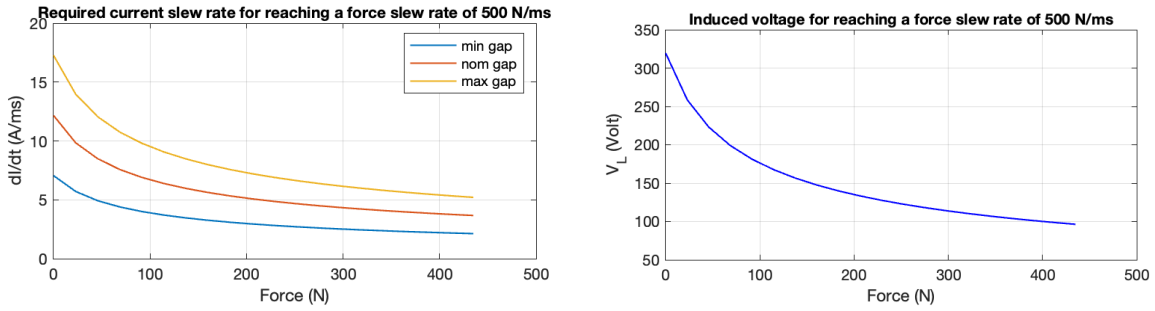

Figure 3.5: (a) Required current slew rate and (b) induced voltage for maintaining the required force slew rate of $500\,\mathrm{N/ms}$, calculated according to (3.13) and (3.14)

3.3. Detailed Design

The key specifications of the main components of the actuator (stator, mover, and coil) have already been determined in section 3.2 to satisfy the requirements listed in section 3.1. This section will focus on the design of other required components and features, such as flux sensors, as well as make necessary improvements to the current design.

3.3.1. Sensor Selection and Placement

In order to control and monitor the status of the reluctance actuator in both current and flux mode, several state parameters need to be measured, including the current in the driving coil, the magnetic flux in the air gap, and the force generated between the stator and the target plate. Meanwhile, the temperature of the coil also needs to be monitored to make sure it remains below a certain level without causing too much influence on the iron core and the permanent magnets due to Joule heating. In this section, sensors needed for measuring these state parameters will be selected, except for the force sensor which will be discussed later in chapter 4.

Hall sensor

As introduced in section 2.3.1.1, a Hall sensor directly measures the flux density using the Hall effect with a proportional relationship between flux and sensor output $V_H \propto I \cdot B$. However, the challenge is that it only measures the local flux density at a single point and has to be placed in the flux path, either in the air gap or in a slot on the stator pole. For this design, the latter approach will be applied, due to the fact that the chosen minimum gap size $x_{\min} = 0.15\,\mathrm{mm}$ is too small to accommodate a Hall sensor.

For this design, the analogue Hall sensor type HE244 is chosen due to its great linearity, low temperature sensitivity, and immediate availability in the lab. The sensor is placed beneath the top surface of the center pole of the stator core, in a machined slot located close to the geometric center of the top surface. Meanwhile, a through hole perpendicular to the top surface of the pole is made to accommodate the wires of the sensor. These stated features are illustrated in Figure 3.6.

However, adding the slot and the hole on the stator core transforms high-permeability regions into

a low-permeability air gaps in addition to the existing air gap, which will alter the flux distribution around the air gap and hence influence the flux density measured by the Hall sensor. To check if such an influence can be predicted and corrected by calibration, FEM analysis will be performed in section 3.4 to validate this design.

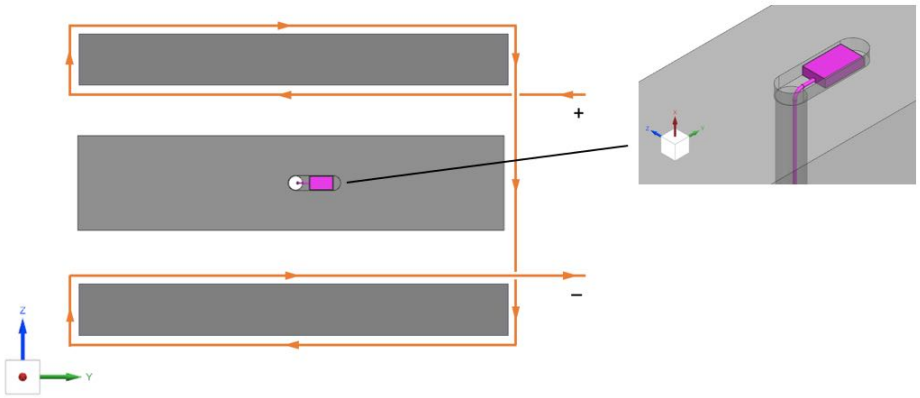

Figure 3.6: Installation locations of Hall sensor (in magenta) and sense coil (in orange) on the stator core, with a zoom-in oblique view for Hall sensor placement in a machined slot on the center pole of the stator. The winding direction for (a single turn of) the sense coil is also indicated with arrows.

Sense coil

As introduced in section 2.3.1.2, a sense coil measures the rate of change of magnetic flux $\mathrm{d}\Phi/\mathrm{d}t$, and has the advantage over Hall sensors that it can be applied in a reluctance actuator without taking space in the air gap. It is also expected to have a lower high-frequency noise thanks to the need for signal integration, which might on the other hand lead to signal drifting at low frequencies.

For this design, a sense coil is installed by wrapping a wire around the two side poles (in series, as shown in Figure 3.6), instead of the center pole, to minimise the flux leakage effect resulting from the bigger and more irregular air gap at the center pole.

To determine the number of turns N_s for the sense coil, quick calculation is done based on the actuator specifications. The generated voltage across the sense coil can be estimated with

$$V_\mathrm{s} = N_\mathrm{s}\frac{\mathrm{d}\Phi}{\mathrm{d}t} = N_\mathrm{s}\frac{N_\mathrm{c}\dot{I}_\mathrm{c}}{\mathcal{R}} \approx N_\mathrm{s}\frac{N_\mathrm{c}V_\mathrm{c}}{\mathcal{R}L} \tag{3.15}$$

where N_c, I_c, V_c denote the number of turns, current, voltage of the driving coil, and $\mathcal{R}$, L denote the reluctance and inductance of the actuator. At the nominal air gap, when the maximum possible input voltage is applied, it can be calculated that $V_\mathrm{s} \approx N_\mathrm{s} \cdot 0.13\,\mathrm{V}$. Thus, a turn number of $N_\mathrm{s} = 4$ is chosen for the sense coil, so that the amplified (20x) sense coil output voltage is comparable with the measuring range of the DAQ module ($\pm 10\,\mathrm{V}$) to ensure a satisfactory signal-to-noise ratio. Further tuning can be made by altering the amplification rate of the signal amplifier.

As for the wire type, a coaxial cable with a conductor diameter of 7×D0.08 mm is used. Given no large current is expected through the sense coil, a thin wire diameter makes the sense coil take less space. Plus, a coaxial cable, compared with a standard cable without shielding, can reduce potential dynamic effects such as capacitive coupling.

Current probe

An inductive-type current probe, Tektronix TCP312A, is used to measure the current in the driving coil. The working principle of the sensor allows it to be installed anywhere in the circuit with great flexibility simply by encircling the wire to be measured, thus there is no need to specifically discuss the placement of this sensor.

Thermometer

For monitoring the temperature of the driving coil, two PT1000 RTD sensors are installed on the inner surface of the coil using Kapton tapes, on the opposite side of each other (Figure 3.7). By measuring the resistance of the sensors, corresponding temperatures can be calculated using a reference mapping.

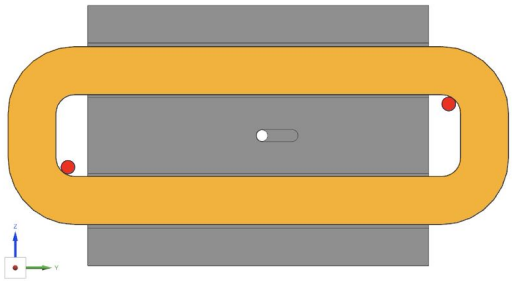

Figure 3.7: Location of the installed PT1000 thermometers on the driving coil.

3.3.2. Grounding Wire Connection

To ensure a proper grounding of the stator core, an M3 threaded hole is added on the side of the core for connecting a grounding wire. The location of the hole is shown in Figure 3.8, where a relatively low flux density is expected (Figure 3.14). Thus the threaded hole is believed to have a minor effect on the flux distribution, especially given its depth of only 7 mm.

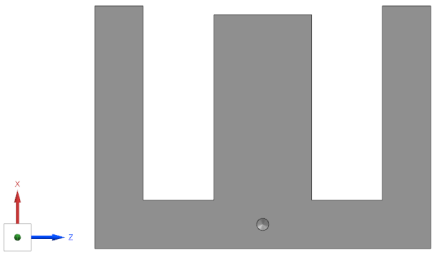

Figure 3.8: Location of the threaded hole for connecting the grounding wire.

3.3.3. Permanent Magnets

According to the calculation in section 3.2, neodymium magnets (NdFeB) in grade N42SH will be used for providing a bias flux, with the dimension of $90 \times 20 \times 1.3\,\text{mm}$ in Y, Z, and X direction respectively as shown in Figure 3.9.

However, for easier fabrication and installation, the above-mentioned dimension is divided into 6 identical block magnets placed along Y direction (Figure 3.9). As a result, the amount of "snapping" force generated between the stator core and each magnet piece is significantly reduced, enabling an easier and safer manual installation. The drawback of this configuration would be the magnified influence of the boundary effect at the interfaces between magnet pieces, and greater dimension errors due to tolerances in Y direction. Furthermore, the installation of several magnets in parallel will suffer from repulsive forces generated between the magnets, thus additional tools and steps are needed to hold the magnets in place during the assembly.

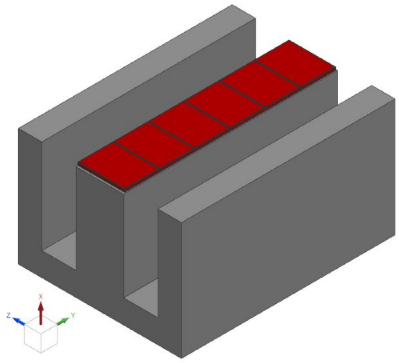

Figure 3.9: Configuration of permanent magnets on the stator core.

3.3.4. Core Material and Lamination

For this design, the main considerations when selecting the core material are saturation flux density and cost, since the main purpose is to achieve the desired force capability at a reasonable cost. As a result, silicon steel M270-50A is used, which typically saturates around 2 T and has a relatively low cost. Some superior alternatives, such as cobalt iron, have a higher saturation flux density, higher permeability, and lower coercivity, which lead to better force capacity, lower reluctance, and less hysteresis effect, respectively. However, such advanced improvements are not primarily desired for this prototype design.

In order to reduce the eddy current effect for a better high-frequency performance, the core is laminated in a direction perpendicular to the flux path (i.e., in the Y direction shown in other figures of CAD models). A number of identical E-shaped laminations are bonded with insulating material (bonding varnish) between each, so that the "equivalent resistance" of the core is significantly increased and the loss due to eddy current can be suppressed. Besides, the bonding varnish between each lamination film also serves as a better heat insulator, and hence can reduce other losses in the form of heat.

The thickness of the lamination film needs to be chosen properly. A thicker film will have a lower suppressing effect on losses, while a thinner film will result in a lower fill factor (effective thickness of core material over total core thickness). For this actuator prototype, a lamination thickness of 0.35 mm is selected, which is a commonly used value and is expected to achieve a fill factor of $> 97\,\%$ (assuming each bonding varnish layer is 8 µm or less).

Besides the stator core, the target plate is also laminated with the same material, lamination thickness, and lamination direction. In addition, a non-laminated target plate in stainless steel 430F

is also made, in order to compare and investigate the benefits of using a laminated target plate.

3.3.5. Mass Reduction of the Target Plate

In order to increase the resonance frequency of the mover to allow a wider measurable frequency range, the mass of the target plate is reduced by simply reducing the width of the target plate from 10 mm, which equals the width of the side poles of the stator core, to 7.5 mm. This way the available space in the target plate can be more efficiently utilised by magnetic flux with a higher density. The mass of the target plate can be further reduced by shaping the target plate according to the flux path, or by using a material with a higher saturation flux density. However, these advanced techniques are considered out of the scope of this prototype design.

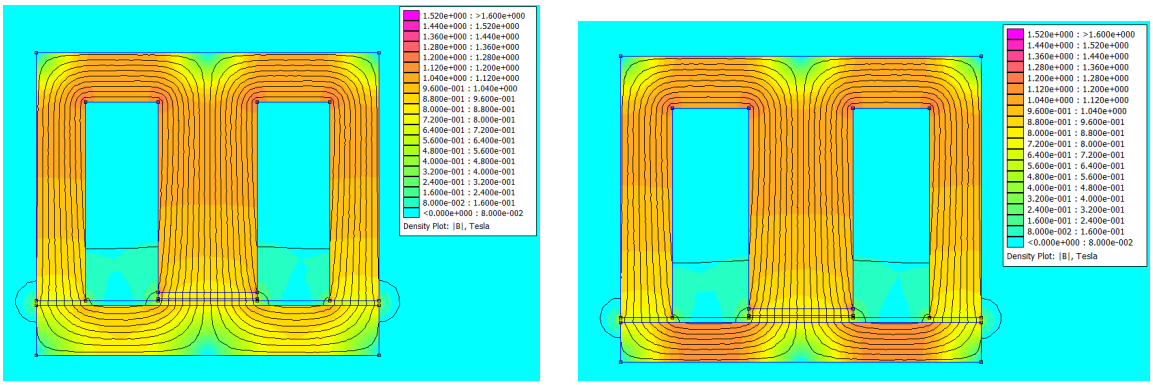

(a) (b)

Figure 3.10: 2D FEM analysis using FEMM of the flux density in the core at nominal air gap and nominal current: (a) before and (b) after width reduction of the target plate.

By comparing the flux density (at nominal air gap x_{nom} and nominal current I_{nom}) before and after the width change estimated using FEMM (Figure 3.10), it is noticed that the maximum flux density in the target rises from 0.95 T to 1.20 T which are both much lower than the saturation level of about 2 T, while the output force only drops from 858 N to 854 N. Thus, considering that this is already an exaggerated case compared to the designed force range of 0 - 500 N, the reduction of target plate width is considered safe with negligible influence on the performance of the actuator.

3.3.6. Stator and Target Housing

A housing for the stator is designed to provide a connecting interface between the stator and the test setup. The housing and other components of the stator are stiffly connected by potting using epoxy resin. The design of the stator housing is shown in Figure 3.11. The key features and design considerations of the stator housing are elaborated below.

Interfaces

The stator housing involves two interfaces, one with the stator core and the other with the test setup. The stator core makes contact with the housing at a few designated contact zones which serve as constraints in different DOFs for an accurate alignment. During assembly, the stator core is pushed onto the contact pads using set screws and held in place by friction before the potting is

carried out (Figure 3.11). On the other side, the stator housing is mounted onto the back plate using 4 threaded joints with extruded ring-shaped features to define constant contact areas (Figure 3.12).

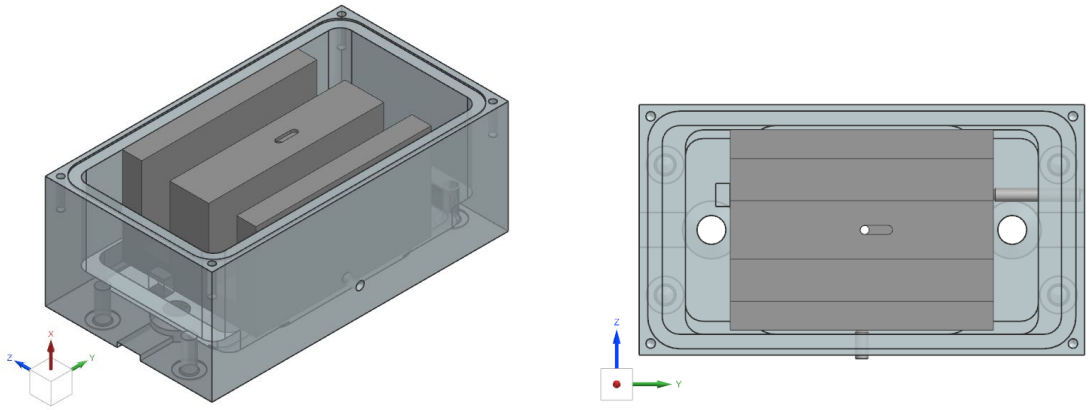

(a) (b)

Figure 3.11: Stator housing with stator core inside: (a) oblique view, and (b) top view, with set screws for fixing the stator core.

Features for assembly and potting

To ensure a flat top surface (the one next to the air gap) of the stator assembly, the potting is designed to be carried out with the top surface facing downwards (i.e., when -X direction shown in the figures aligns with the gravity direction). Thus, three holes are made on the opposite side of the top surface (Figure 3.12), which serve as outlets for all the wires of the stator components (coil, sensors, grounding wire, etc.), as well as potting compound inlets and air outlets during the potting. The holes are enlarged at the top to form pools that can hold extra epoxy resin in order to refill when the resin inside the enclosure shrinks. Besides, a slot along Y direction is also made to accommodate the wires coming out from the holes.

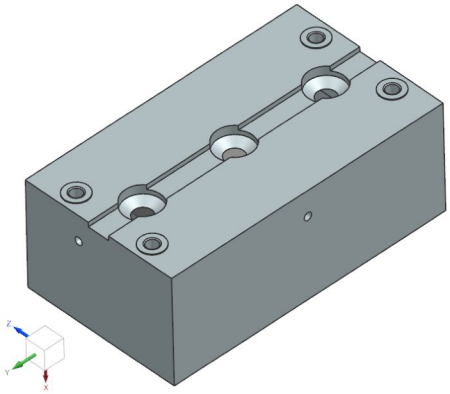

Figure 3.12: The back of the stator housing, showing the features designed for potting and mounting onto the setup.

The housing for the target plate has similar alignment features as those designed for the stator housing described above. However, since no potting is needed to connect the target plate and the target housing, epoxy glue will be used for the bonding, and an external force will be applied on the target plate to push it against the alignment features. Another interface involved is the one with the load cell, which is designed to be simply a fine-machined surface that enables a reliable force

transmission. Other features designed include: a through hole with M20 thread for preloading the load cell using a threaded rod, three M3 threaded holes for mounting accelerometers, and three "arms" for making contact with position sensors.

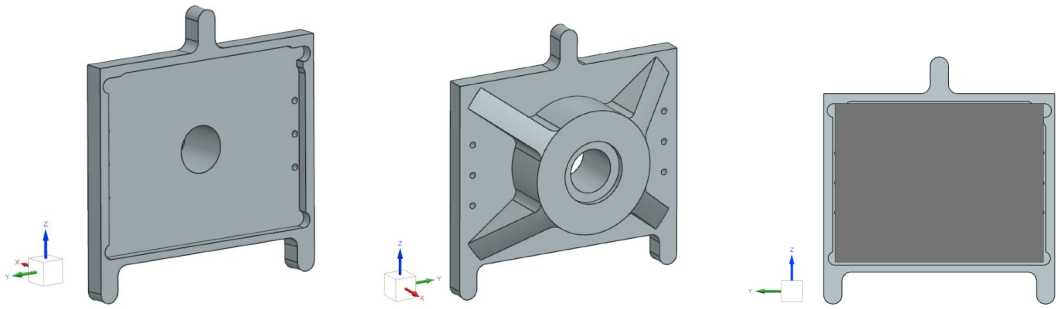

(a) (b) (c)

Figure 3.13: Design of the target plate housing: (a) oblique view of the front side, (b) oblique view of the back side, (c) front view of the front side, with target plate inside.

3.4. Design Validation using FEM

2D finite element method (FEM) analyses are carried out using the application FEMM, to simulate the flux distribution at a cross-section of the stator and mover core, and estimate the corresponding generated force.

In this specific case, FEM has the advantage that it is able to simulate in a more realistic way while taking into account the uneven cross-sectional flux distribution as well as flux fringing and leakage, which were not considered or estimated in previous calculations. However, some assumptions are made to simplify the problem into a 2D static analysis. As a result, some effects and factors that might pose minor influences on the actuator performance are neglected, such as eddy current in the core and variation of parameters in the third (depth) direction.

Force Generation

The force-generating capability for the design actuator is validated using FEMM (Figure 3.14). The simulation is carried out for several critical scenarios, for example, the highest allowed temperature and maximum possible gap size, to check if the requirements mentioned above can be satisfied. The force generated by the actuator can be calculated by integrating Maxwell's stress tensor along the contour of the cross-section of the target plate.

Table 3.6: Results from 2-D FEM analysis using FEMM

Gap size	Current	Magnet H_c	B_{avg} in target	Force output
nominal	0	max	0.60 T	251 N
nominal	I_{rms}	min	1.19 T	854 N
max	I_{rms}	min	0.88 T	427 N
max	I_{peak}	min	1.10 T	660 N
nom	$-0.82\,I_{\text{rms}}$	max	-0.01 T	22 N
min	$-0.82\,I_{\text{rms}}$	max	-0.00 T	42 N

The results are summarised in Table 3.6. It can be seen that, the bias force generated by the magnets at nominal gap and zero current is 251 N which matches the designed value 224 N with margin. Besides, the force generated at max gap and at I_{rms} and I_{peak} are higher than the designed $F_{\text{rms}} = 354\,\text{N}$ and $F_{\text{peak}} = 500\,\text{N}$, satisfying the requirements. The minimum residue force at minimum air gap is $F_{\text{min}} = 42\,\text{N}$, being lower and thus better than the estimated value of 65 N.

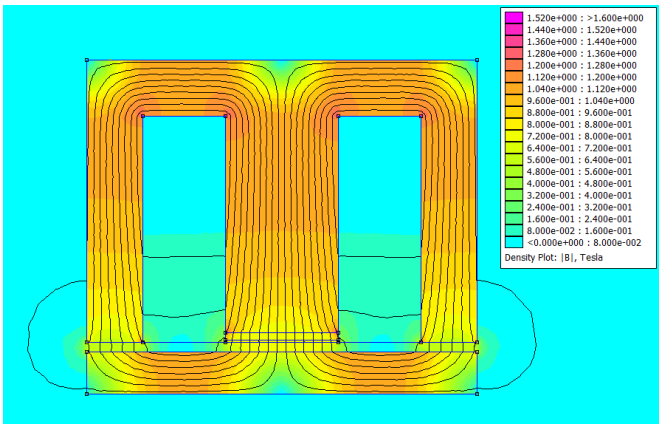

Figure 3.14: 2D FEM analysis of the designed actuator using FEMM, at the nominal gap size, with maximum allowed current and minimum magnet coercivity used.

Slot for placing Hall sensor

A similar FEM analysis is also carried out with the presence of the slot made for accommodating the Hall sensor, in order to investigate the flux distribution around the slot. As expected, the flux density is locally decreased at the slot due to the greater reluctance of this path, as demonstrated in Figure 3.15.

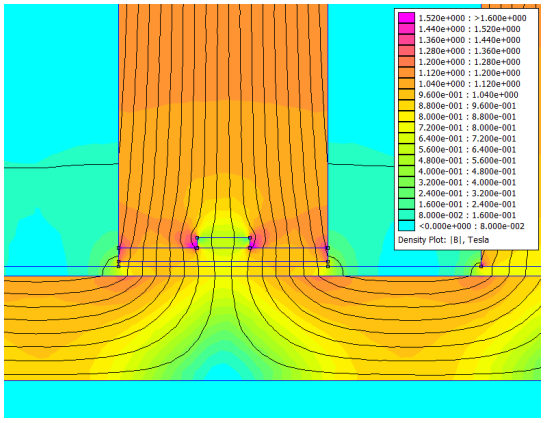

Figure 3.15: Flux distribution around the slot made for accommodating the Hall sensor simulated using FEMM.

To further investigate the relation between the measured flux density at the Hall sensor slot B_{Hall} and the actual average flux density at the top surface of the center pole B_{real}, the simulation is run at various current levels. In Figure 3.16(a) it is shown that the simulated $B_{\text{Hall}}/B_{\text{real}}$ ratio is almost constant except for when the flux density comes close to zero. By inspecting the flux distribution at those data points, it is found that the flux distribution alters in an irregular way due to the remaining leakage flux in the core. This is considered the main cause for the irregular change of relations demonstrated in both Figure 3.16(a) and Figure 3.16(b). In Figure 3.16(b) it is also shown

that the relation between the generated force and measured flux can still generally fit into a quadratic model, and the measured data only deviates from the model when the measured flux is close to zero. However, the parameters for the model might be dependent on the gap size, current level, and input frequency, which will then make the calibration and compensation of the Hall sensor output much more challenging.

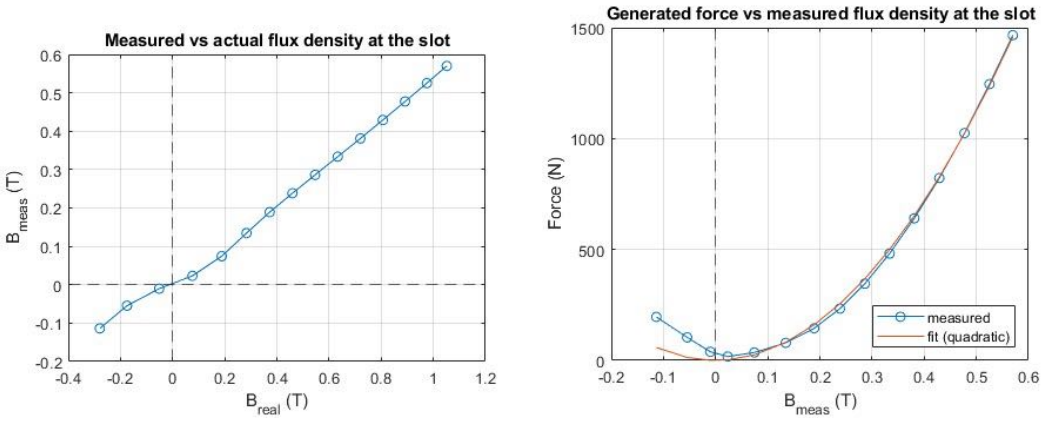

(a) (b)

Figure 3.16: FEM simulation results in the presence of a slot in the core for accommodating the Hall sensor: (a) flux density measured at the Hall sensor slot vs. average flux density in the gap, (b) generated force vs. flux density measured at the Hall sensor slot.

3.5. Actuator Assembly

Based on the design above, all components of the actuator are fabricated and assembled. Potting is then performed on the actuator by filling the assembly with potting compound, which, once hardened and cured, serves to fix all components together and enhance the mechanical performance of the stator.

The stator assembly before and after performing the potting are shown in Figure 3.17. The detailed procedure for the assembly and potting of the actuator is described in Appendix A.

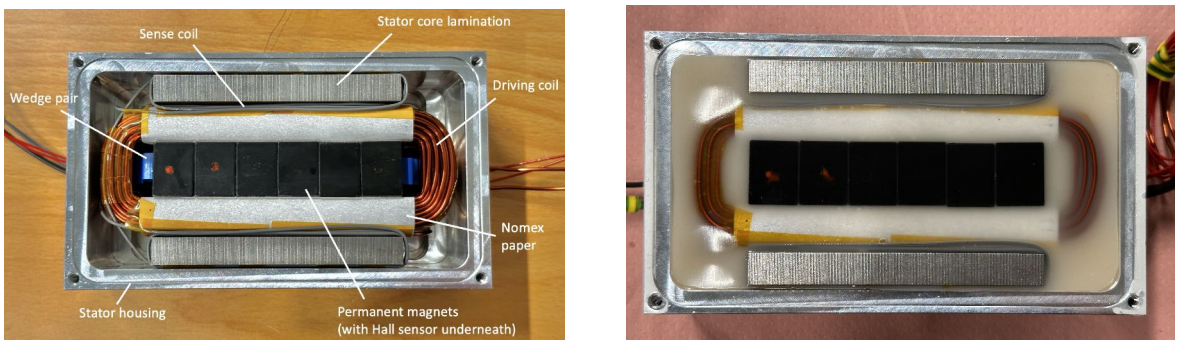

(a) (b)

Figure 3.17: Assembled actuator stator (a) before and (b) after potting.

4

Design and Realisation of a Test Setup for Reluctance Actuators

4.1. Requirements

The main objective is to build a platform for testing current- and flux-based control on reluctance actuators and measuring necessary data for performance evaluation. Therefore, the main functional requirements are

- Providing a mechanical base for supporting, aligning and positioning the actuator.
  - Hold the stator and the mover at certain positions with sufficient stiffness.
  - Adjust and measure the air gap size between the stator and the mover within a certain range.
- Providing means of measuring force and position.
  - Measure the 1D force output of the designed actuator within its operation range, both statically and dynamically up to a few kilohertz.

More specific requirements are given in Table 4.1, with corresponding reasoning as follows. The maximum reachable gap size is required to be at least 30 mm so that the force output can reach nearly zero. The gap positioning accuracy is mainly limited by the operating accuracy of the mechanism for gap adjustment as well as the parallelism between the two surfaces forming the air gap, for which an experience value is given as the requirement. The gap measuring error is on the other hand determined by the sensor accuracy and thus required to be lower than 1 % of the gap range. Regarding force measurement, the maximum measurable force is determined by the force range of the designed actuator, while the frequency and repeatability requirements are determined based on the desired control performance, i.e. achieving a control bandwidth of at least 1 kHz and a feedforward accuracy of at least 99 %. Finally, the required static stiffness is determined so that the natural frequency for a 1 kg moving mass is higher than the required measurable frequency range.

Table 4.1: System-level requirements for reluctance actuator design

Parameter	**Must**	**Wish**
Reachable gap range	0 mm to 30 mm	up to 40 mm
Gap positioning accuracy	$< 30\,\mu m$	$< 10\,\mu m$
Gap measuring accuracy	$< 10\,\mu m$	$< 5\,\mu m$
Maximum measurable force	$\pm 500\,N$	up to $\pm 2\,kN$
Force measuring frequency range	0 Hz to 1 kHz	up to 3 - 5 kHz
Force measuring repeatability (relative to full range)	$< 0.5\,\%$	$< 0.1\,\%$
Static stiffness in force direction	$> 5 \times 10^7 N/m$	$> 4 \times 10^8 N/m$

4.2. Conceptual Design

In this section, firstly, the general form of the setup is determined, and the whole setup is subdivided into several subsystems based on the functional requirements mentioned above in section 4.1. Then the design strategies for each subsystem are described in detail.

4.2.1. General Form and Subsystems

To limit workload, a static-gap design is chosen, in which the stator and the mover are both stationary during measurement so the air gap is kept constant. However, the gap size should still remain adjustable to reach and lock at any point within the range of the gap size. A dynamic design with a free mover would better simulate a motion system, but as a result the setup design would become more complicated and challenging. In a static setup, although we would not be able to measure the positioning accuracy directly, the static-gap experiments could still provide sufficient data for the evaluation of the flux control and flux sensor merging. Such data would also enable us to estimate the dynamic-gap performance by simulation using the static-gap data.

The whole setup consists of the following subsystems:

- **Gap adjusting system**: The mechanism for guiding and driving 1-DOF fine adjustments on the gap size between the stator and the mover, while keeping other DOFs properly constrained.
- **Base structure**: The structural support that provides sufficient stiffness between the stator and the mover to reduce error and enable a wide measuring frequency range. Meanwhile, 1-DOF relative translation between the stator and the mover should be allowed when the gap size is being adjusted within the designed range.
- **Force sensing system**: Sensor and auxiliary structure for measuring the dynamic force output of the actuator.

The following sections will elaborate on the design of each subsystem.

4.2.2. Gap Adjusting System

Based on the description in section 4.2.1, the gap adjusting system is essentially a 1-D translation stage, consisting of a driving mechanism, a guiding mechanism, and a 1-D position sensor. The corresponding key requirements are:

- Provide proper sensitivity for manual operation to allow a smooth and accurate adjustment of the gap size.
- Provide enough stiffness and load-bearing capacity to avoid unwanted motion in other DOFs and ensure a safe operation (for both human and machine).
- Can measure the distance and angle between the stator and the mover, in order to control the size and parallelism of the air gap.

The resulting design for the gap adjusting system is shown in Figure 4.1. A threaded rod is used to convert rotational input from the knob into linear motion of the stator, which is attached to one end of the threaded rod using a nut. The knob at the other end of the rod has a threaded hole that mates with the rod and is used for manual operation. A compression spring is used to preload the thread mating so that mechanical backlash in this mechanism can be avoided. Furthermore, a plastic washer is put between the knob and the base plate it makes contact with, to reduce friction and enable an easier actuation. To guide the linear motion driven by the threaded rod, a linear rail bearing is used. The actuator is mounted onto a back plate, which is then mounted onto the carriage of the linear bearing. For position sensing, three inductive position probes are used in a triangular configuration to measure the gap size as well as any relative rotation between the stator and the mover.

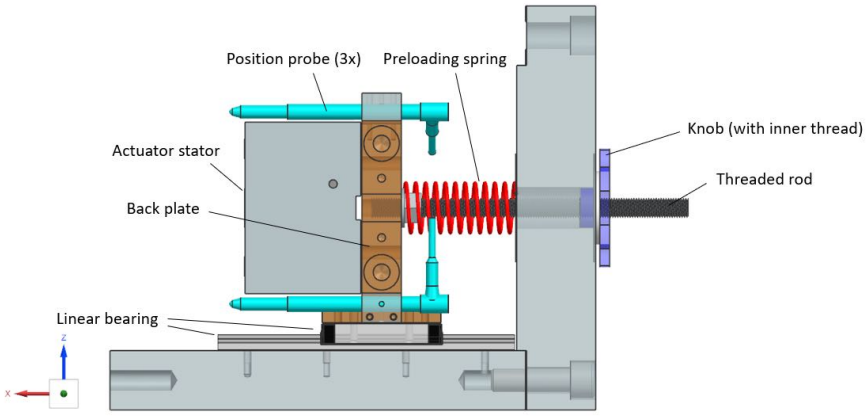

Figure 4.1: Side view of the gap adjusting system. Some irrelevant parts and features are hidden.

Standard parts selection

For the threaded rod, the metric fine thread M10×1.25 (in stainless steel) is selected. If a rotational resolution of 2° is assumed for manual operation, the thread pitch of 1.25 mm gives a linear resolution of 7 µm, which is considered sufficiently accurate compared with the actuator's full motion range of 1500 µm and the minimum gap size of 150 µm. As for the load capacity, the maximum force generated by the actuator when no current is supplied is expected to be no greater than 2 kN, which is much smaller than the proof load for the M10 thread. Hence, the selected parameters for the threaded rod are expected to satisfy the requirements above.

For the linear rail bearing, given the design of the mechanism shown in Figure 4.1, force generated by the actuator will not directly load the linear bearing, thus a miniature linear bearing with a low profile can be selected to minimise the space taken.

4.2.3. Base Structure

Based on the description in section 4.2.1, the key requirements for the base structure are:

- Provide sufficient stiffness between the stator and the mover.
- Allow the stator or the mover to be released in 1 DOF and move within the designed range of the gap size whenever needed, and can be locked again to restore the high stiffness.
  - The locking operation (from released to locked) should cause minimal or sufficiently small movement in the direction of air gap adjustment.
  - Once released, the remaining friction in the direction of motion should be minimal, to allow an accurate and smooth air gap adjustment.

The resulting design for the base structure is shown in Figure 4.2. Four thick plates are used to form a sufficiently stiff outer structure, and on each side of the base structure two additional side plates perpendicular to Y axis are used to stiffen the structure. It is worth mentioning that, the two side plates connected to the back plate of the actuator (brown part in Figure 4.2) each consist of 8 thin plates, to reduce the bending stiffness of the combined plate about the X direction, so that the Y-direction force they exert on the actuator during installation can be minimised, so that the accurate alignment between the stator and the target plate will not be much influenced.

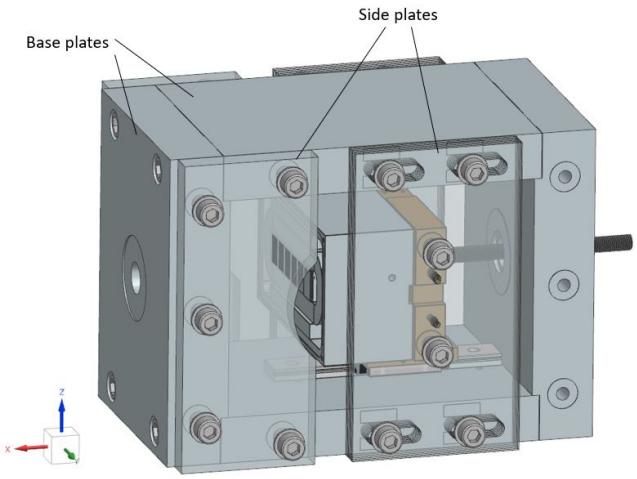

Figure 4.2: Base structure with the actuator stator and the gap adjusting system also present. Some other irrelevant parts and features are hidden.

4.2.4. Force Sensing System

This subsystem is required to accurately measure the force output of the reluctance actuator both statically and dynamically. The key requirements are:

- Can measure throughout the force range of the designed actuator (0 - 500 N) with error less than 0.5 % of the full range.
- Can measure across a wide frequency range from DC up to at least 1 kHz.

While the required measuring range of 500 N would not pose a great challenge, the measurement at high frequencies up to a few kilohertz would require a high axial stiffness for the load cell and a low weight for the target plate assembly in order to increase the natural frequency of the force measuring system to be higher than the desired measuring frequency range.

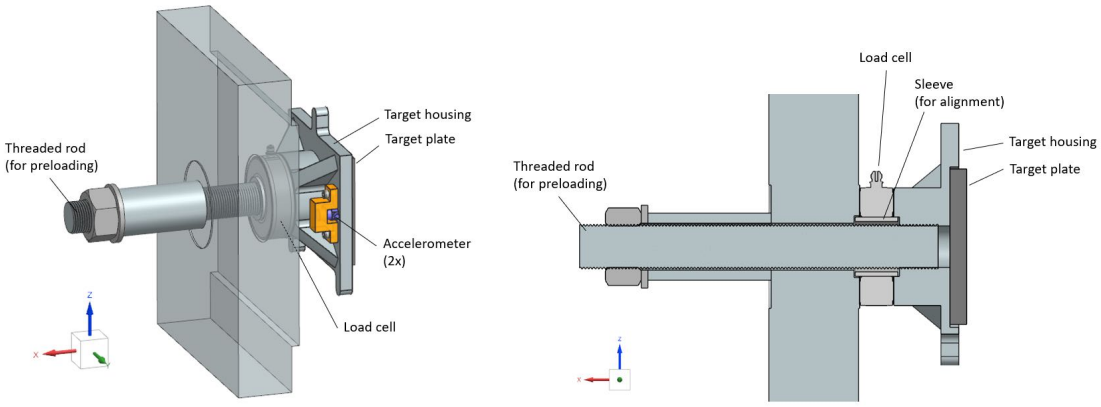

Figure 4.3: The force sensing system (including one of the base plates, the load cell, and the target plate assembly) showing the installation of the load cell: (a) oblique view, and (b) cross-sectional view.

For a high axial stiffness of the load cell, piezoelectric-type load cells are chosen for their high sensitivity, which does not necessarily decrease when the dimension of the load cell increases thanks to its working principle. This characteristic makes it possible to have a large and very stiff load cell that is almost equally sensitive as its smaller and less stiff alternatives. In this setup, the

configuration of the load cell is shown in Figure 4.3(b). Note that a threaded rod is used to apply a preload to the load cell, in order to enable measuring tensile forces. Meanwhile, a 3D-printed circular sleeve is applied between the threaded rod and the inner surface of the load cell (Figure 4.3(b)), in order to align the axis of the load cell with the center of the target plate, so that the torque acting on the load cell due to off-center loading is minimised.

However, the resulting natural frequency of the measurement system might still not be sufficiently high for ignoring the difference between the measured force F_{meas} and the applied force F_{real} due to the nonzero acceleration of the target plate. Considering the load cell as a spring and the target plate assembly as the corresponding moving mass, then according to the equation of motion,

$$ma = F_{\text{real}} - F_{\text{meas}} = F_{\text{error}} \tag{4.1}$$

which shows the cause of the force error. To estimate F_{error}, the transfer function of a mass-spring system gives

$$\frac{x}{F_{\text{real}}} = \frac{a/s^2}{F_{\text{real}}} = \frac{1}{ms^2 + k}, \tag{4.2}$$

and by combining the two equations, we get

$$\frac{F_{\text{error}}}{F_{\text{real}}} = 1 - \frac{F_{\text{meas}}}{F_{\text{real}}} = \frac{ms^2}{ms^2 + k}. \tag{4.3}$$

According to this, the force error due to finite acceleration would be 1 % at 10 % of the natural frequency, which increases to 5 % at 20 % of the natural frequency.

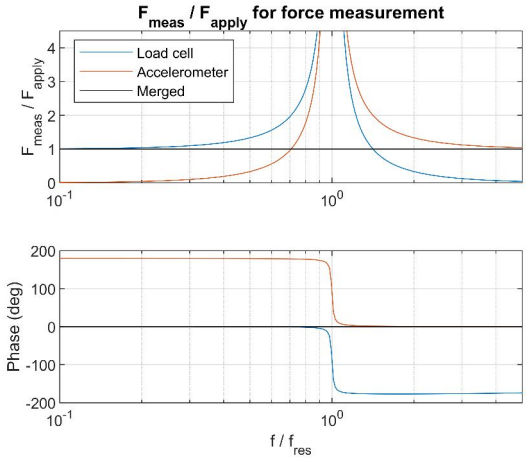

Figure 4.4: Bode plot of theoretical relation between applied force F_{apply} and measured force F_{meas}, demonstrating the merging of output signals from the load cell and accelerometer. It is shown that, theoretically and ideally, a perfectly accurate force measurement can be realised using this hybrid measuring scheme.

To compensate for this force error, accelerometers are used to measure the acceleration of the target plate, which is multiplied by the moving mass m and added to the measured force from the load cell. Theoretically, the load cell and accelerometer are completely complementary in this case, and the corrected results would be equal to the applied force, as shown in Figure 4.4 plotted using (4.3). However, there could be a certain degree of mismatch between the two signals due to sensor errors, influence from other dynamic modes, and the differences in the sensor frequency responses.

In this setup, two 1-D accelerometers are installed on the back of the target plate in a symmetric configuration, so that ideally the average of the two sensor outputs should represent the acceleration at the center of the target plate.

4.3. Detailed Design

4.3.1. Material Selection

Structural parts

Materials for the manufacture of each part are selected while various factors such as weight, stiffness, cost, and machinability are taken into account. For structural parts serving to provide a high stiffness, stainless steel AISI 304 is selected due to its high elastic modulus. It should be noticed that, the relatively high density of stainless steel, combined with the bulky design of structural parts, would result in a heavy final assembly. However, since there are no mobility requirements on the test setup, the disadvantage of having heavy parts would be no more than a more difficult assembling process.

Stator housing

The stator functions as an enclosure for the potting of the stator core and an interface for the mounting and alignment of the stator core. It has a shell-like shape with many small features and tolerance specifications. Since its stiffness is not expected to have a great limiting effect on the dynamic characteristics of the setup, the machinability of the material becomes the prior consideration to lower the cost. Thus, aluminum 6082-T6 is selected for the fabrication of the stator housing.

Target housing

Similar to the stator housing, the target housing functions as an interface for mounting the target plate onto the base and transmitting the generated force to the load cell. However, the weight and stiffness of this part are of great concern, since the mass of the target assembly directly determines the natural frequency of the mass-spring system, if the load cell is considered a spring. Thus a low mass for the target housing is desired to obtain a wider measurable frequency range below the resonance frequency of the load cell. Meanwhile, a high elastic modulus is also desired for the target housing, in order to suppress its internal dynamics when the target is dynamically loaded. As a result, titanium alloy Ti6Al4 is chosen for its superior balance between density, strength, and elastic modulus.

4.3.2. Sensor Selection

The general types or grades of the sensors to be used for force and position measurement were already determined in the conceptual design (section 3.2). In this section, the specific models of the sensors are selected based on requirements and hardware availability.

Load cell

The piezoelectric load cell Kislter 9061A is used, which can measure up to 400 kN and has an axial stiffness of 15.4 kN/µm, which theoretically results in a natural frequency of 19.8 kHz for the moving mass of about 1 kg in our design. However, in reality, the finite contact stiffness at contact interfaces will bring down the stiffness as well as the natural frequency of the force sensing system. Besides, other dynamic modes will also contribute to creating measurement error, which will be analysed in section 4.4.

To convert the charge output of the load cell into a voltage signal, a Kistler 5018A laboratory charge amplifier is also used.

Accelerometer

The Brüel & Kjær 4397A miniature accelerometer is chosen to compensate for the force error of the load cell output at high frequencies. This model has a measuring range of $\pm 500\,g$ and a frequency

range of 1 - 25 000 Hz. Considering the maximum force output of 500 N and the moving mass of 1 kg, the corresponding free-motion acceleration would be 50 g, which is 10 times smaller than the maximum measurable acceleration of the sensor. Thus, any resonance peaks with a Q factor under 10 will remain within the measuring range of the accelerometer, which corresponds to a damping ratio of 5 % or more. Even a smaller damping might cause a small part of the peak to be out of the measurable range, but the accelerometer can still provide a significant correcting effect to the load cell output, until when it is very close to the resonance frequency.

Position probe

Three of Tesa GT 62 inductive position probes are used for calibrating and measuring the air gap. The measuring range of ± 5 mm and repeatability of 0.05 µm are considered sufficient compared to the designed minimum and maximum air gap of 0.15 mm and 1.65 µm. Besides, each probe applies a force of only 0.9 N against the counter-surface to be measured, which is considered negligible compared with the force range of 0 - 500 N for the designed actuator.

4.3.3. Contact Interfaces

To ensure predictable and consistent contact surfaces when the parts deform due to loading and thermal expansion, the general strategy applied in this project is to add an extruded ring-shaped feature at each mounting hole on one of the contacting surfaces, as shown in Figure 4.5. As a result, the two surfaces only make contact at these “contact pads”, and certain deformation is allowed without influencing the contact area.

While designing contact pads, as a rule of thumb, the contact area is defined by the standard washer size for the same thread type. The standard thickness of contact pads (i.e., the distance between the contact pad surface and the rest of the surface) is set to 0.5 mm throughout the setup. For contact interfaces with the load cell, contact areas are machined with tighter tolerances and better surface quality, to ensure a more reliable force transmission.

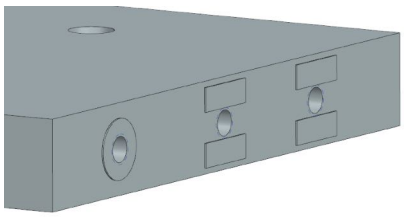

Figure 4.5: Contact pads at threaded holes. The shapes of the contact area are adapted to the shapes of the contact interface of the counterpart to be mounted.

4.3.4. Accessibility Features

Additional holes are added onto the base structure parts, for providing accessibility to the bolts inside the base so that some adjustment can be made without the need to disassemble the base structure to access the bolts, or for letting through sensor wires. Given the relatively small sizes and amount of accessibility holes, they are not expected to have a significant influence on the stiffness and dynamics of the setup.

4.3.5. Instrument Connection

The connection of the setup with measuring equipment in the electric domain is demonstrated in the block diagram below (Figure 4.6). In addition to the components already introduced in this report, a PCB is used to provide a current source to power the Hall sensor, and meanwhile amplify the sensor outputs from the Hall sensor and the sense coil. Besides, a Speedgoat target machine is used to process all the measured data and generate an output signal, which is then sent to a linear power amplifier that is able to work in current or voltage modes, with maximum output voltage and current being 60 V and 8 A respectively.

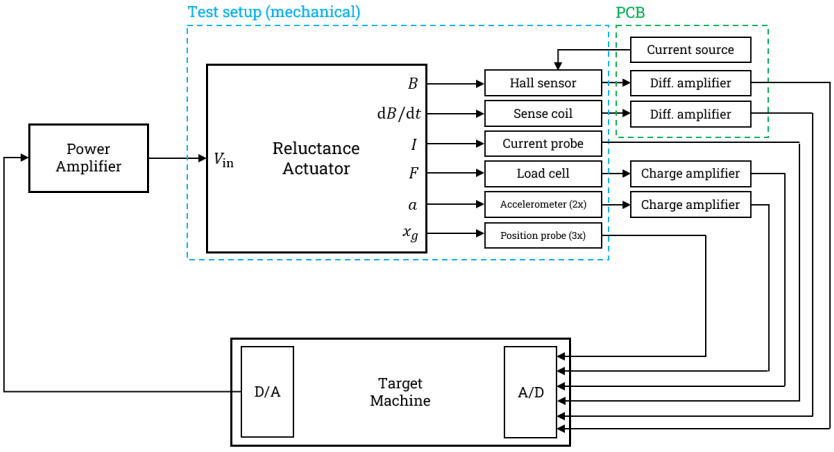

Figure 4.6: Diagram showing the instrument connection of the test setup.

4.3.6. Final Design

The CAD model for the final design of the test setup is shown in Figure 4.7.

4.4. Design Validation by FEM

For FEM analysis, a simplified CAD model of the setup is made, by removing parts and features that are considered to have little contribution to the results, such as the linear bearing, threaded rods, and detailed features for alignment or improving accessibility. Meanwhile, the load cell is removed from the model, and its stiffness is represented using a joint with finite stiffness between remote points attached to the two load cell interfaces. The linear and rotational stiffness for the joint are set according to the datasheet provided by the load cell supplier. However, for simplicity, contact stiffness is not taken into consideration while setting up the FEM model, so the frequencies and shapes of the modes resulting from the FEM analysis might be imprecise.

4.4.1. Static FEM Analysis

The deformation of the stator and the target plate are measured with a 500 N distributed attractive load applied between them, simulating the case when the maximum allowed force is statically applied. The result shows that the total relative deformation between the target plate and the stator is about 1.8 µm (Figure 4.8), resulting in a static stiffness of 2.8×10^8 N/m.

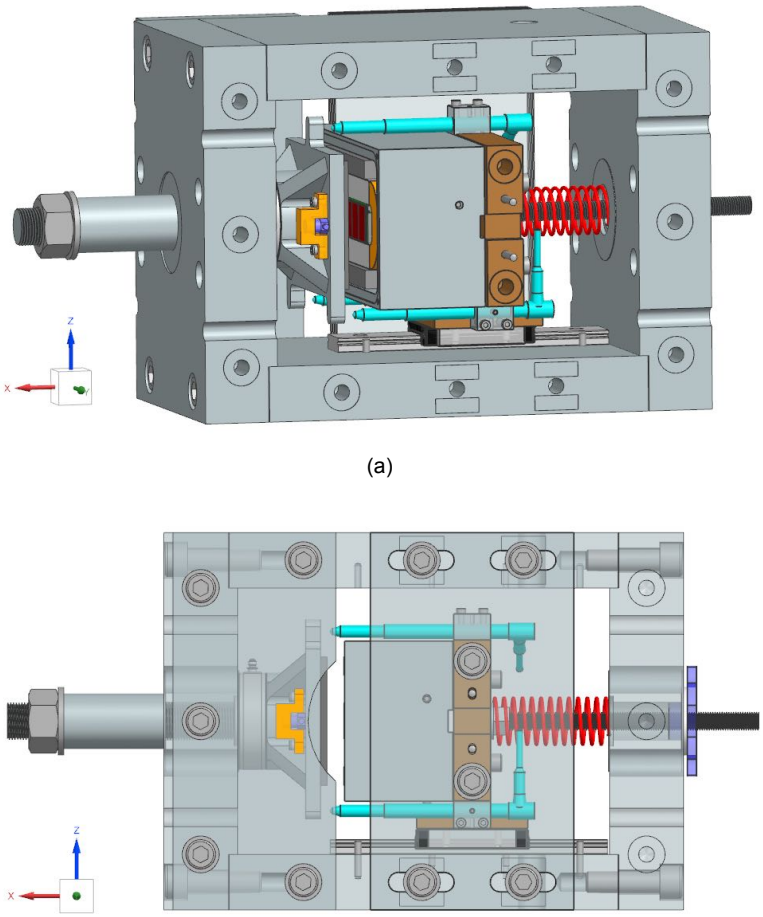

(a)

(b)

Figure 4.7: Finalised design for the test setup: (a) oblique view with two plates on the side of the base structure hidden, and (b) side view.

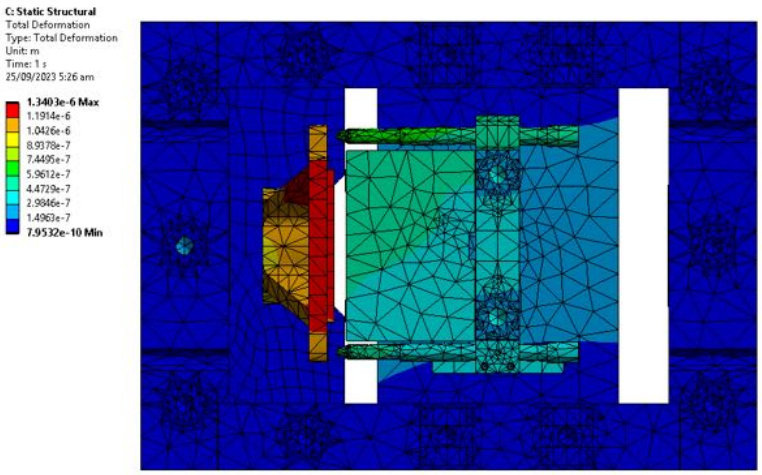

Figure 4.8: Static FEM analysis of the designed setup (some side plates are hidden in the plot to reveal inner components), with $500\,\mathrm{N}$ distributed attractive load applied between the stator and the target plate. As a result, the relative deformation between stator and target plates about $1.8\,\mu\mathrm{m}$ (Figure 4.8), resulting in a static stiffness of $2.8 \times 10^8 \mathrm{N/m}$.

4.4.2. Dynamic FEM Analysis

Using a simplified CAD model of the setup with irrelevant parts and features removed, dynamic FEM analysis is also carried out using ANSYS and processed in MATLAB for calculating the system transfer function based on the simulated results. The transfer functions from the applied force F_{real} to the force measured by the load cell F_{load} and accelerometer F_{acc} are plotted in Figure 4.9, where $F_{\text{acc}} = m_{\text{eff}} a_{\text{meas}}$ and m_{eff} represents the effective mass corresponds to the measured acceleration. Then the merged force output is obtained simply by adding the two output signals, i.e., $F_{\text{merge}} = F_{\text{load}} + F_{\text{acc}}$.

For obtaining the merging results demonstrated in Figure 4.9, the mass of the target assembly (including the target plate, target housing, and accelerometers) of 1.11 kg is used as an initial value for the effective mass m_{eff}, then the value of m_{eff} is tuned until an optimal merging result is obtained with the first (few) resonance peaks fully eliminated. Finally, the effective mass of $m_{\text{eff}} = 0.90\,\text{kg}$ is found to offer the best compensation effect on the first observed mode at 1.8 kHz, and is used for plotting the results shown in Figure 4.9. This value is smaller than the total mass of the target assembly, mostly due to the fact that the modes being compensated do not involve the entire target assembly and thus have smaller modal masses than the total target mass.

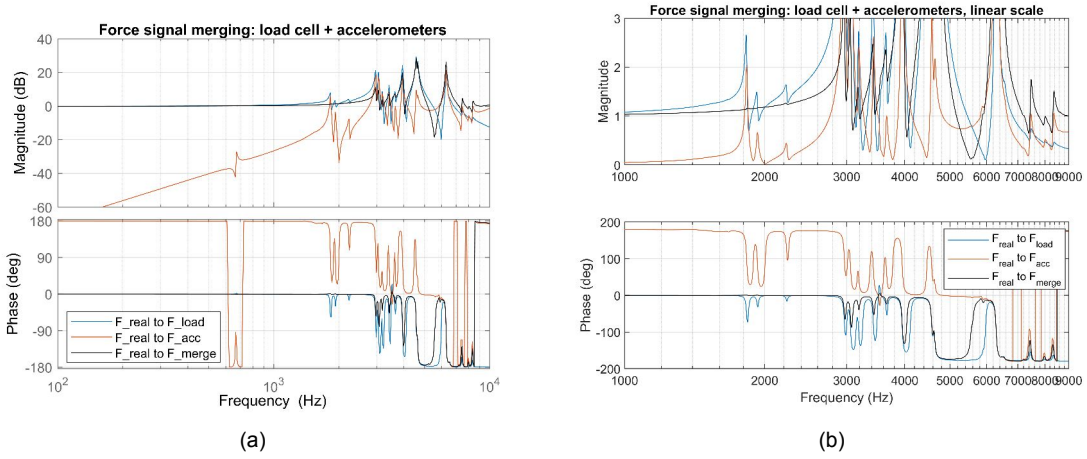

Figure 4.9: FEM simulated frequency response from applied force F_{real} to measured force using load cell F_{load}, accelerometers F_{acc}, and merged from both F_{merge}: (a) from 100 Hz to 10 kHz with logarithmic scale for magnitude, (b) zoom-in at high frequencies from 1 kHz to 9 kHz, with linear scale for magnitude to show the improvements more clearly. It can be seen that the first three modes observed in the load cell measurement (between 1.8 and 2.2 kHz) are effectively compensated by accelerometers, and frequencies corresponding to force errors of 0.5 % and 1.0 % are improved from 800 Hz and 1100 Hz to 1200 Hz and 1620 Hz, respectively.

In the results shown in Figure 4.9, by comparing the magnitude and phase of the merged data to the original measurement from the load cell, resonance peaks below 3 kHz are effectively suppressed using measurements from accelerometers. The frequencies and corresponding mode shapes for the first five modes observed in Figure 4.9 are shown in Appendix C. However, the magnitude of the merged signal still deviates from 1 with the increase of frequency, which is probably due to the influence of modes at higher frequencies, which cannot be fully compensated using the selected m_{eff} value. As a result, using the merged signal for force estimation, maximum frequencies corresponding to force errors below 0.5 % and 1.0 % are improved from 800 Hz and 1100 Hz to 1200 Hz and 1620 Hz, respectively. Thus, it can be concluded from the FEM analysis that, using the hybrid force measuring scheme is able to widen the measurable frequency range if an error of less than 0.5 % is required. However, the measuring accuracy is still limited by the influence of higher-frequency modes, which cannot be fully compensated using the current method.

4.5. Setup Assembly

The machined parts and the reluctance actuator prototype are assembled and properly aligned with the help of custom-designed tools. The detailed procedure is described in Appendix B. The outcome is shown in Figure 4.10.

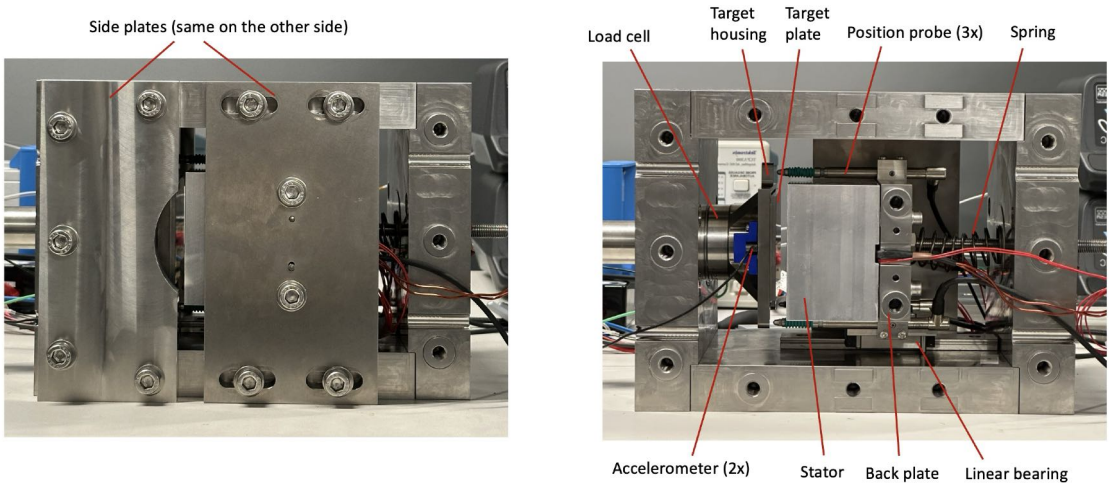

Figure 4.10: Assembled setup: (a) in measuring state with side plates installed for higher stiffness, (b) without side plates to reveal components inside.

5

Calibration and Measurements of the Designed Reluctance Actuator

In this chapter, experiments are carried out to test and calibrate the designed actuator and setup, in preparation for the flux control implementation in the future. Methods and corresponding results of the measurements will be described and discussed.

5.1. Preliminary: Load Cell Calibration

The testing and calibration of the load cell is considered of great importance and concern, since the applied preload could influence the sensitivity of the load cell, and charge-mode piezoelectric load cells are prone to drifting, both of which effects could lead to increased uncertainty of the measurements. These two sources of uncertainty are investigated below and approaches for compensation are proposed.

5.1.1. Signal Drift

In a piezoelectric measuring chain, any leakage current or insufficient insulation could lead to a drift in the output signal. While using the load cell with a charge amplifier in the DC mode, there will be little filtering effect on the drift due to the relatively large time constant used for the charge amplifier, and as a result the drift can be observed directly in the measured signal. Ideally, the drift is linear with a constant rate, and according to the datasheet of the charge amplifier, the drift should be within ±0.03 pC/s (corresponding to ±0.008 N/s) for a properly configured measuring chain. However, the force drift observed in our measurements often exceeds this range, being up to 0.05 - 0.10 N/s with varying drift rate and direction over time. This can already lead to a force error above 1 % of the full force range in a 2-minute DC measurement, and the constantly varying drift rate makes it challenging to predict and compensate for this effect. As a result, there could be a great uncertainty that is hard to quantify in the results measured in the DC mode due to signal drifting.

However, by observing the measured drift, it is noticed that, the drift tends to stabilise with a decreased rate over time, down to 0.01 - 0.02 N/s in 1 - 2 minutes (Figure 5.1), when the entire setup is kept static without any change in physical states and input signals. Plus, although the setup is properly grounded and high-insulation cables are used for connection, any cable movement or physical contact with the setup during measurements is still found to create an additional noise or drift. Based on these observations, the following techniques are suggested to reduce or compensate for the force drift for DC measurements:

- Keep the setup static (without any change in input signals or physical states) for a longer time

before each measurement.
- Reduce any cable movement and unnecessary contact with the setup during measurement.
- At the beginning and end of each measurement, wait for 30 seconds without any change in the applied force, so that the measured force in these sections can be used to estimate the drift rate throughout the measurement.
- Repeat each measurement multiple times so that data with lower observed drift can be selected and used.

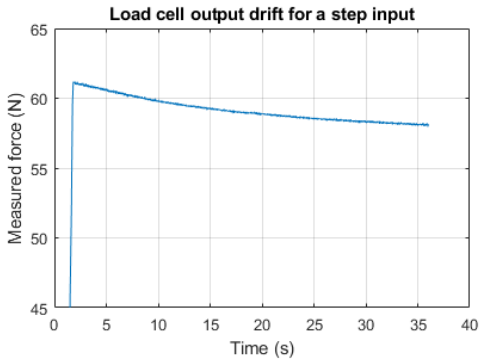

Figure 5.1: Measured force for a step input using the load cell and the charge amplifier in DC mode, demonstrating the force drift with decreasing drift rate over time.

However, it is still hard to generally quantify the influence of drift on the measurements after applying these techniques, since the ways some experiments are performed tend to cause more drift or make it harder to observe and compensate for the drift. Thus, for each measurement that involves DC force measurements, the influence and compensation methods of the drift will be discussed respectively below.

5.1.2. Sensitivity Calibration

In the setup, the load cell is clamped between the base and the target plate and preloaded using a threaded rod as demonstrated in Figure 4.3, which creates a force shunt and causes the effective sensitivity of the load cell to be lower than the specified value. Thus, a static calibration is performed to determine the sensitivity of the load cell in the preloaded state.

In the configuration shown in Figure B.2, i.e. with the force measuring direction aligns with the gravity, calibration weights are incrementally placed on top of the target plate (with center of mass vertically aligns with the geometric center of the target plate), with total weight up to 280 N. Corresponding outputs of the load cell are measured, which are compared with the applied weights to determine the sensitivity of the load cell. Results are shown in Figure 5.2, where a trend line with model $y = k_{\text{fit}}x$ is fitted to the data and the measured ratio between measured and applied force $k_{\text{fit}} = F_{\text{meas}}/F_{\text{appl}}$ is found to be 0.896 with a mean error of 0.39 N and maximum error of 0.81 N.

Although the load cell is used in DC mode for this experiment, the drifting effect discussed in section 5.1.1 is believed to have a negligible influence on the calibration result, since sample points are obtained by measuring step changes made within 0.5 - 1.0 s with expected drift being less than 0.02 N. Besides, drifts can be easily estimated and compensated using the signal segments right before and after the loading step where the applied load is constant.

The repeatability of this calibration result is tested by repeating the preloading and calibration process (with a reduced number of sample points) 2 weeks after the initial calibration. The resulting $F_{\text{meas}}/F_{\text{appl}}$ is found to vary within 0.005 or 0.6 % of the initial result, indicating an acceptable repeatability of the calibration for our application.

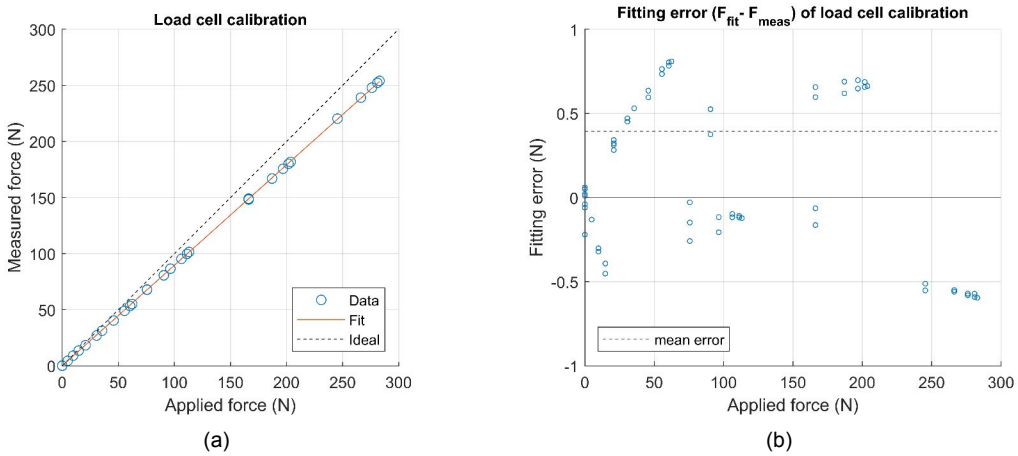

Figure 5.2: Calibration results for the load cell, showing the data samples and a fitted trend line in the form of $y = k_{\text{fit}}x$. The slope of the fitted line $k_{\text{fit}} = F_{\text{meas}}/F_{\text{appl}}$ is 0.896, with a mean error of 0.39 N and maximum error of 0.81 N.

However, this calibration scheme still leaves some additional uncertainty that is hard to quantify. For example, the load cell is calibrated in a smaller force range (0 - 280 N) than the designed actuator (0 - 500 N). Plus, the load cell is calibrated by compressive loading, while the actuator to be tested would only be able to generate tensile forces to the load cell. But since a good linearity with small fitting error is observed in the force range of the calibration, no significant changes in sensitivity are expected if the force range is expanded by 3 - 4 times, especially given that the force range of the actuator is only 1/400 of the measurable range of the load cell. Another potential source of uncertainty is that, the loading direction is vertical during calibration but would be horizontal during other tests, which might lead to a change in the initial loading state of the load cell caused by the force and torque created by the weight of the target plate. However, due to the fact that a piezoelectric load cell only measures the relative change in force, and the weight of the target plate (with its housing) is only 1/50 of the maximum force output of the actuator, the influence of such an effect is also believed to be negligible.

5.2. Actuator Impedance

To characterise the electric model of the realised reluctance actuator, the impedance of the actuator at several typical gap sizes is measured using the Bode 100 analyzer. The result up to 100 kHz is plotted in Figure 5.3. Below 1 kHz, measurements at different gap sizes are found to generally match the theoretical expression of coil impedance $Z = Ls + R$, with the same impedance at low frequencies and a transition of slope from s^0 to s^1 at certain corner frequencies $\omega_{\text{corner}} = R/L$ that increases with gap sizes. This also indicates that the actuator inductance L decreases with increasing gap sizes. By fitting the theoretical model of coil impedance $Ls + R$ into the data, the coil resistance R is measured to be 0.72 Ω and actuator inductance L is found to be 53 mH, 39 mH, and 32 mH at minimum (0.15 mm), nominal (0.90 mm), and maximum (1.65 mm) air gap, respectively.

For frequencies above 1 kHz, a gradual drop in phase is observed, from 90° down to around 0° at 40 kHz. A sudden change in the slope of the magnitude from s^1 to s^{-1} is also observed at around 40 kHz. This is believed to be caused by the capacitive coupling effect within in driving coil, which is equivalent to having capacitors formed between loops of the coil. This, as a result, creates an

additional pole at around 40 kHz in the frequency response of actuator impedance [1]. An equivalent electrical schematic of the coil with capacitive coupling effect and relevant analyses are given in [1]. However, since the control bandwidth of the actuator is expected to be no greater than 10 kHz, the influence of capacitive coupling is considered to be minor and no special concern would be needed. Besides, another observation would be that small peaks at around 1.3 kHz appear in some magnitude and phase curves, especially for the measurements made at lower gap sizes (the peak is not clearly observable in all curves due to the frequency interval between samples being bigger than the peak width). This is believed to be caused by the dynamics of the test setup, and its frequency also matches the frequency of the first resonance peak observed in the mechanical dynamics of the setup (Figure 5.18).

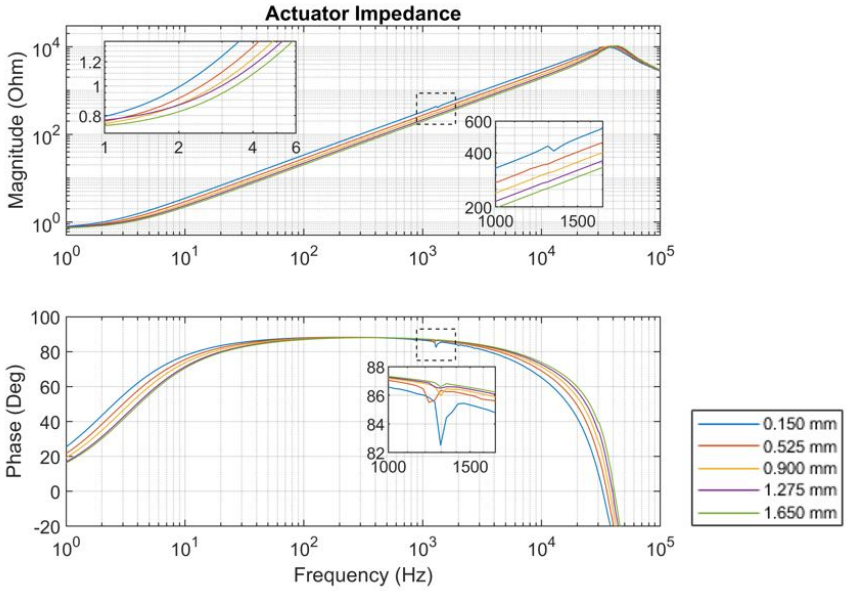

Figure 5.3: Measured actuator impedance (with laminated target plate) at different gap sizes, with zoom-in views for low-frequency magnitudes and the peaks around 1.3 kHz. The observed trend generally matches the theoretical model $Z = Ls + R$, while peaks are observed around 1.3 kHz due to the mechanical dynamics of the setup, and drops in both magnitude and phase are observed due to the capacitive coupling effect.

5.3. Actuator Calibration

In the flux control scheme proposed in Figure 2.15, two key component needs to be determined or obtained through actuator calibration, the nonlinear compensators $F(I, x_g)$, $F(B, x_g)$ and the flux merging factor $k_{\text{flux}} = B_{\text{Hall}}/B_{\text{sense}}$, as concluded at the end of the section 2.4. In this section, the designed reluctance actuator is calibrated in multiple experiments to determine these two components in the control scheme.

5.3.1. DC Calibration

Due to the presence of multiple nonlinear effects, the ideal theoretical relations between current, flux density, air gap, and force as described by (2.9), (2.14), and (2.15) would not be sufficiently accurate for nonlinear compensation (NLC) in the proposed control scheme in Figure 2.15. For more effective nonlinear compensation, DC calibration of the designed actuator is carried out to measure and characterise the actual relations between key variables of the actuator (namely, x_g, I_{coil}, B_{Hall}, B_{sense}, and F).

However, the use of permanent magnets in our reluctance actuator leads to the presence of a bias force even when the actuator is idle (i.e., no current in the driving coil). Considering the fact that a piezoelectric load cell only measures the relative force change instead of the absolute force, this force offset created by the magnets will be missing in the load cell output, while only relative force changes based on this offset will be measured. Thus, a dedicated experiment is carried out as described below to measure the bias force created by the permanent magnets at different gap sizes.

Preliminary: Bias force measurement

For measuring the bias force provided by the permanent magnets, the air gap is manually varied (using the knob installed on the threaded rod) from 0 mm to 35 mm, or in the other direction, with no current applied in the driving coil. The reason for covering the gap range up to 35 mm is to make the force output sufficiently close to zero (i.e. <0.15 N from FEM estimation) so that it can be used to set the zero-force point. A 30-second static-force period is also added before and after the operation to measure the force drift.

During the operation, the gap size is measured using three position probes, and outputs from the position and force sensors are acquired using a Speedgoat target machine at 100 Hz. In order to reduce the influence of force drift and other random effects on the results, the experiment is performed with multiple repetitions, and for each repetition a constant offset is applied to the measured force so that it reaches zero when $x_g = 35\,\text{mm}$. Then, three repetitions with observed force drift no greater than 0.01 N/s (based on the 30-second segments added to the beginning and end of each measurement in which the air gap is kept constant) are selected to form a combined data set for curve fitting.

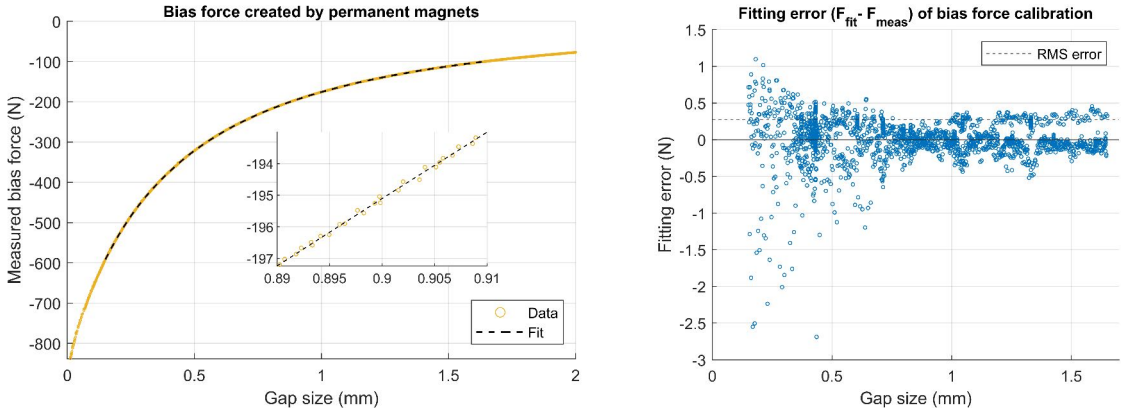

Figure 5.4: Bias force created by permanent magnets measured by continuously varying the gap size with zero current in the driving coil: (a) measured data with a smoothing spline fitted to the data, and (b) corresponding fitting error for each sample point, with a root-mean-square error of 0.27 N and maximum error of 2.69 N.

Next, a smoothing spline (a curve with certain smoothness between a cubic spline interpolant and a least-squares straight-line fit) is fitted to the combined sample set from the three measurements. This specific fitting method is chosen instead of a parametric fitting based on the theoretical model $F_{\text{bias}} = k_1/(x_g + k_2)^2$, since the latter is found to result in a much greater fitting error, meaning that the theoretical model fails to model some unexpected effects and thus cannot be used to characterise the $F_{\text{bias}}(x_g)$ relation with decent accuracy. Besides, the purpose of curve fitting here is to characterise the trend formed by the sample points using a smooth curve with the lowest possible error, without the need to extract any parameter. As a result, the fitted curve using

smoothing spline has a root-mean-square error of 0.27 N and maximum error of 2.69 N (i.e. 0.5 % of the full force range). The sample points and fitted curve are plotted in Figure 5.4. This obtained curve can be used to determine the bias force at any gap size within the operating range.

However, although only data with the lowest force drift (< 0.01 N/s) are selected and used, each measurement takes around 120 seconds and the corresponding force error can still reach up to 1.2 N. Besides, this estimation is based only on the data measured when the air gap remains constant, in which case the drift tends to be lower than the case when the gap size is constantly changing. As a result, the actual transient drift could be greater than 0.01 N/s with a varying drift rate over time, thus their influence on the measurements is hard to estimate and compensate for, making it challenging to quantify the repeatability of the results. Furthermore, another source of error is that, when applying a force offset to the force measurement, it is assumed that $F_{\text{bias}} = 0.15$ N at $x_g = 35$ mm, which is estimated using 2D FEM analysis and can be different than the actual bias force.

Some potential approaches for reducing the above-mentioned errors are proposed but not experimentally applied due to time limitations. They are therefore left as suggestions for future work:

- Carry out the experiment with a constant negative current (such as -2 A or -4 A) in the driving coil, in addition to the zero-current case above. As a result, the force drift might be lower due to the lower changing rate of the applied force. These results are redundant with the result from the zero-current case, and thus can replace the zero-current bias force measurement for bias force compensation if a significant reduction in force drift is observed.
- After varying the air gap from 0 to 35 mm, add a "return trip" to let the air gap travel from 35 mm back to 0 mm. As a result, for each gap size, two force measurements can be obtained with known time separation. This provides more information on understanding the force drift and might enable a more accurate drift compensation.
- Shortcut the flux loop using a separate plate at $x_g = 35$ mm so that the force applied on the target reaches absolute zero. This provides a more accurate way of setting the zero point of the measured force curve.

With the result of this measurement providing knowledge on the bias force at different gap sizes, in the next section, DC calibration of the actuator is carried out for characterising the relation between current, gap size, flux density, and force output, during which all forces are measured relative to the zero-current bias force and can be corrected using the fitted curve obtained above.

Measurements for DC calibration

For measuring the relations between current, gap size, flux, and force, both current and gap size are swept with certain intervals (0.2 A and $(x_{\max} - x_{\min})/8$, respectively) throughout their operating ranges, by applying the current input profile shown in Figure 5.5(a) (with the power amplifier operating in the constant-current mode) at 9 evenly distributed gap sizes throughout the gap range, respectively. The actual current in the driving coil I, flux density from the Hall sensor B_{Hall}, and force output F are measured. The results are shown in Figure 5.5(b)-(d), where each data point is obtained by averaging the corresponding sensor output signal over the period where it remains steady. For force measurements, the drift can be estimated by observing the change of force output during constant-current segments, and can be compensated accordingly if found necessary. Furthermore, bias forces at different gap sizes are determined using the $F_{\text{bias}}(x_g)$ curve obtained in Figure 5.4, and are applied as an offset on the force measurements.

In Figure 5.5(b), the relation between the measured current I and the flux measured by Hall sensor B_{Hall} at different gap sizes are shown. An approximately linear relationship with a decreasing slope

for bigger gap sizes is observed, which is consistent with the theoretical relation (2.9). The highest and lowest slopes have a difference of 2.2 times, which corresponds to a maximum gain variation of at least 50 % if the measured result at a signal gap size is used for controller design.

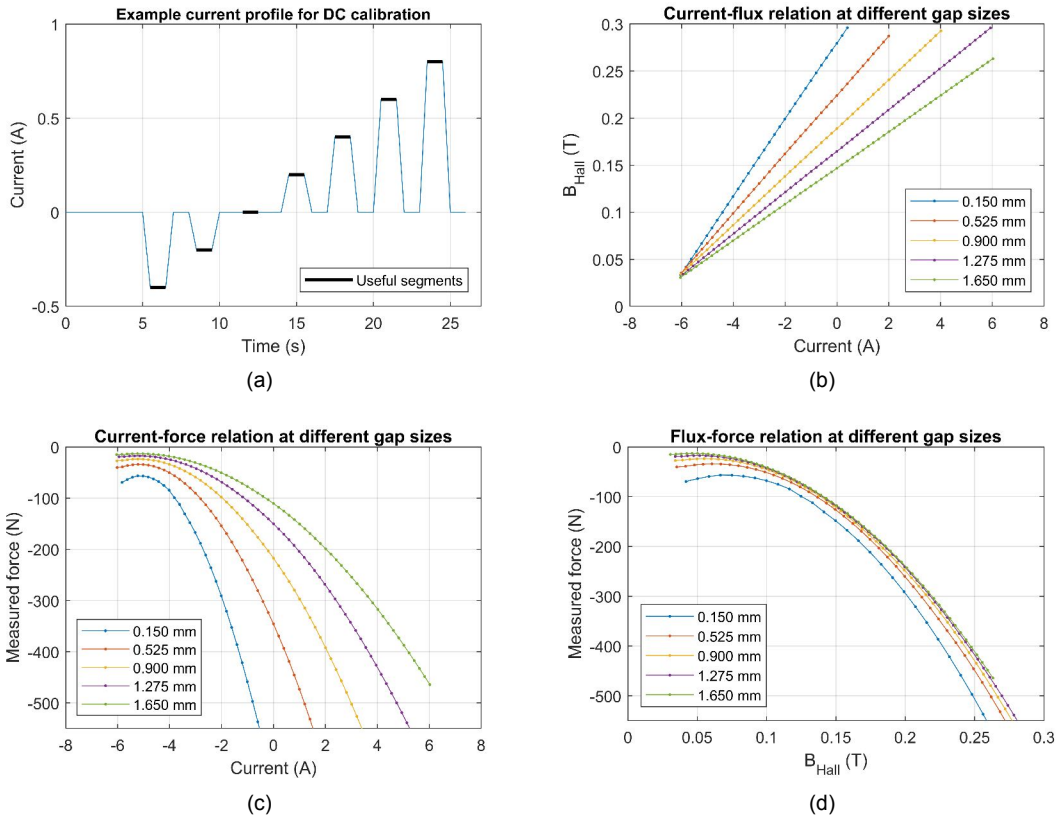

Figure 5.5: DC calibration of the reluctance actuator prototype: (a) example current input profile with useful segments highlighted, and (b) current-flux, (c) current-force, (d) flux-force relations at different gap sizes. Note that the calibration is performed at 9 evenly distributed gap sizes, while only 5 are plotted for better clarity. It can be observed in (b) that the current-flux relation is approximately linear with a greater slope for smaller gap sizes. By comparing (c) and (d), it is found that the current-force relation is much more dependent on gap size variation than the flux-force relation, resulting in a higher actuator stiffness.

In Figure 5.5(c) and (d), the measured current-gap-force relationship $F(I, x_g)$ and flux-gap-force relationship $F(B_{\text{Hall}}, x_g)$ are shown. Besides the quadratic relations as expected based on the theoretical equations (2.15) and (2.14), a nonzero minimum force that increases with decreasing gap size is observed, while corresponding current and flux when minimum forces are reached also differs for different gap sizes. This is believed to be caused by the mismatch between the flux created by the coil and the magnets, with slightly different flux distributions at different gap sizes. The minimum force for $x_g = 0.15\,\text{mm}$ is 57 N, which approximately matches the earlier estimation of $F_{\text{min}} = 65\,\text{N}$ during the actuator design in section 3.2. Furthermore, by comparing Figure 5.5(c) and (d), it can be noticed that the current-force relation is much more dependent on gap size variation than the flux-force relation. This means that if the actuator is controlled to keep a constant flux density, the resulting gap dependency of the force output, i.e. the stiffness of the actuator, will be much lower than the case in which a constant current is controlled. To better quantify the difference, the gradient of force with respect to gap size $\mathrm{d}F/\mathrm{d}x_g$, or in other words the actuator stiffness, is calculated and plotted for the constant current and constant flux cases as shown in Figure 5.6(a) and (b). It can be seen that the actuator stiffness increases for smaller gap sizes in both cases, being up to $-898\,\text{N/mm}$ in the constant current case and up to $-174\,\text{N/mm}$ in the constant flux case (or $-707\,\text{N/mm}$ and $-86\,\text{N/mm}$ if only the data with $x_g \geq 0.525\,\text{mm}$ are

considered). By taking a reference current value of $-2\,\mathrm{A}$ and reference flux value of $0.15\,\mathrm{T}$ for a clearer comparison, it is shown in Figure 5.6(c) that the actuator stiffness for the given flux level is 5 - 10 times lower than the constant current case.

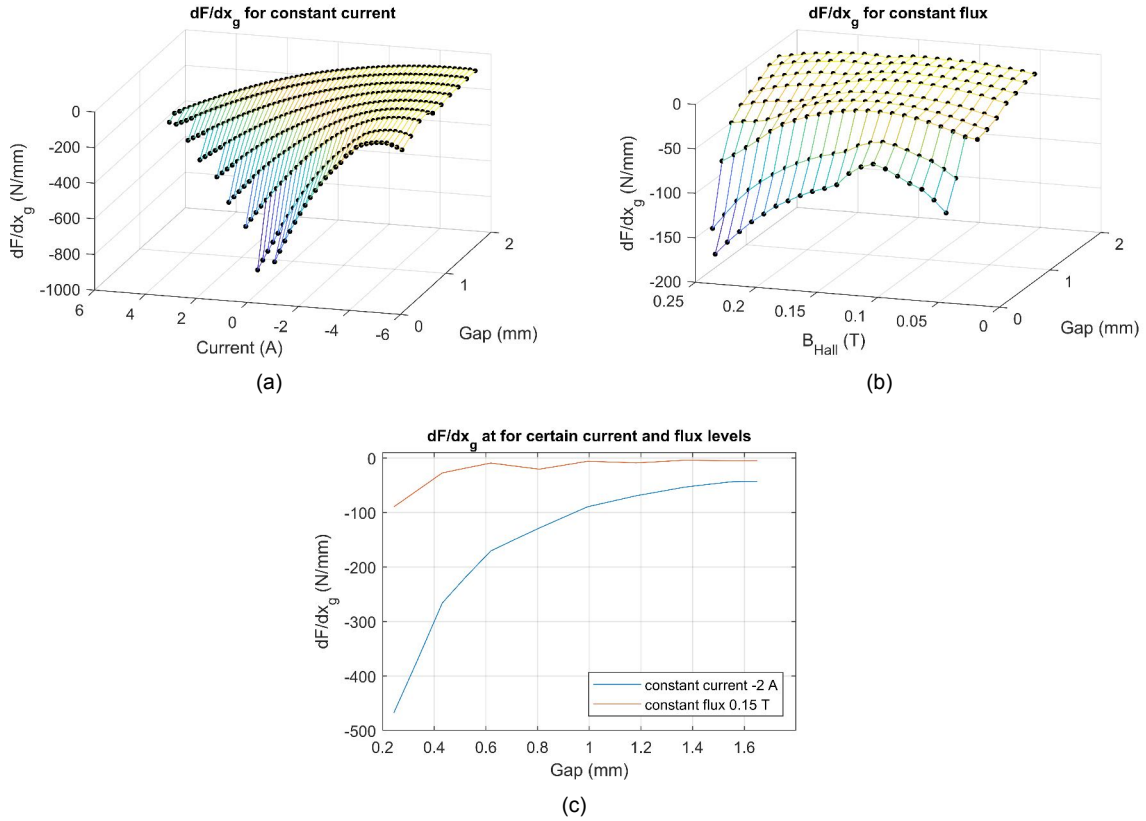

Figure 5.6: Gradient of force output with respect to gap size (i.e. actuator stiffness), $\mathrm{d}F/\mathrm{d}x_g$, for (a) constant current and (b) constant flux. For easier comparison, (c) is made by taking a reference value for both current and flux. As a result, the actuator stiffness reaches up to $-898\,\mathrm{N/mm}$ for constant current and up to $-174\,\mathrm{N/mm}$ for constant flux (or $-707\,\mathrm{N/mm}$ and $-86\,\mathrm{N/mm}$ if only the data with $x_g \geq 0.525\,\mathrm{mm}$ are considered). Generally, keeping the actuator at a constant flux, instead of a constant current, would reduce the actuator stiffness by at least 5 - 10 times.

Then, 3D mappings of the relations $B_{\mathrm{Hall}}(I, x_g)$, $F(I, x_g)$, and $F(B_{\mathrm{Hall}}, x_g)$ can be made by performing natural-neighbor interpolation on the data set as shown in Figure 5.7, from which 2D look-up tables can be obtained for any given grid by extrapolation.

However, it is worth noticing that, the way the input profile (Figure 5.5(a)) is designed makes the current in the coil always reach the target current level from the same direction, meaning that the measured data can only represent a half of the hysteresis B-H loop. Hence the repeatability of the measured relationship would be influenced by hysteresis errors in the measured flux and force. One of the following experiments (section 5.4) will help estimate this uncertainty caused by the hysteresis effect.

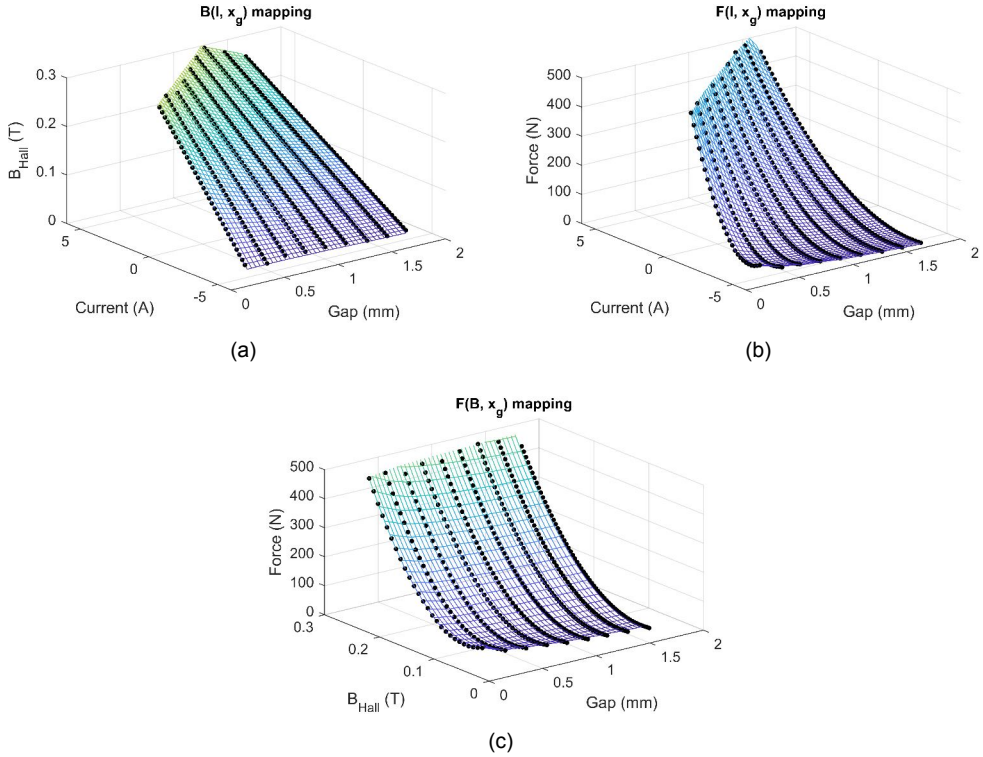

Figure 5.7: 3D mappings between gap x_g, current I, flux B_{Hall}, and force F by performing natural-neighbor interpolation on the data shown in Figure 5.5.

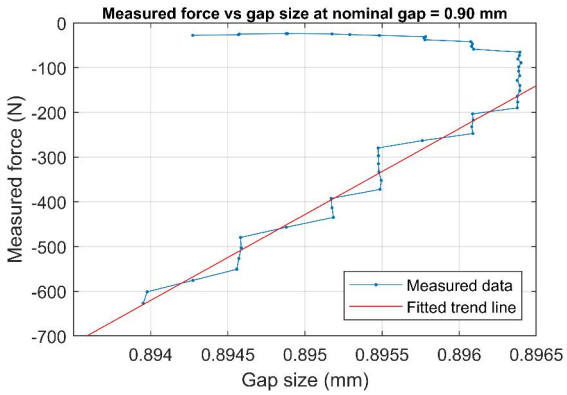

Figure 5.8: Relation between force output and corresponding gap size measured at nominal air gap of $0.90\,\text{mm}$. A trend line is fitted to (part of) the data for determining the static stiffness of the setup, and its slope is found to be $1.9 \times 10^8\,\text{N/m}$.

Furthermore, in the same experiment, by measuring the change in gap size using position probes, the static stiffness of the setup can be estimated. In Figure 5.8, the relationship between force output and corresponding actual gap sizes is plotted, where gap sizes are measured by averaging the outputs from the three position probes. In the plot data points "jump" in big steps due to the resolution limitation of position probes, but a steady trend can already be clearly identified for stiffness estimation. Besides, it is noticed that, data points with absolute force output smaller than 195 N, which corresponds to the zero-current bias force at the specific gap size, behave differently with a seemingly much lower stiffness and an opposite gap varying direction. The cause of this effect is still unclear and thus only data points with force output greater than 195 N are taken for stiffness estimation. A trend line is fitted to the data and the slope turns out to be $1.9 \times 10^8\,\text{N/m}$.

Similar results are obtained also at other gap sizes. This, combined with a moving mass of 1 kg, will result in a resonance frequency of 2.2 kHz. This achieved stiffness is considered satisfying compared with the FEM result of 2.8×10^8 N/m which did not take the effect of contact stiffness into account.

5.3.2. AC Calibration of Flux Sensors

The AC calibration aims to measure and compare the flux output from the Hall sensor and the sense coil, so that their output ratio $k_{\text{flux}} = B_{\text{Hall}}/B_{\text{sense}}$ can be obtained for different gap sizes, DC current levels, and frequencies. This value k_{flux} serves as the flux merging factor for matching the output signals from the Hall sensor and the sense coil, as indicated in Figure 2.15.

To investigate the dependency k_{flux} on different variables, two separate tests are performed as follows.

5.3.2.1 Measuring k_{flux} with respect to DC current

In this measurement, DC current level and gap size are taken as the main variables being investigated. An input profile in the form of Figure 5.9(a) is used to sweep the DC current throughout its operating range (with 0.4 A interval), with 50 Hz AC components of 0.3 A added on top to enable the use of the sense coil which can only measure AC flux. The amplitude and frequency of the AC component are selected to achieve a good signal-to-noise ratio for both sensors.

For data processing, measured signals from the sense coil are first integrated using the cumulative trapezoidal method to restore B_{sense} from $(\mathrm{d}B/\mathrm{d}t)_{\text{sense}}$. Then, sinusoidal waves are fitted to the Hall sensor output and the integrated sense coil output to determine the amplitudes of the AC elements in both signals, which gives the B_{Hall} and B_{sense} values at the corresponding DC current level and gap size.

Results for different gap sizes are plotted in Figure 5.9(b), in which it can be clearly noticed that the flux output ratio k_{flux} depends on both DC current and gap size. Smaller air gaps lead to a smaller k_{flux}, while as for DC current dependency, k_{flux} increases as the DC current moves away from about -4 to -6 A, which corresponds to the current when minimum forces are reached (Figure 5.5(c)).

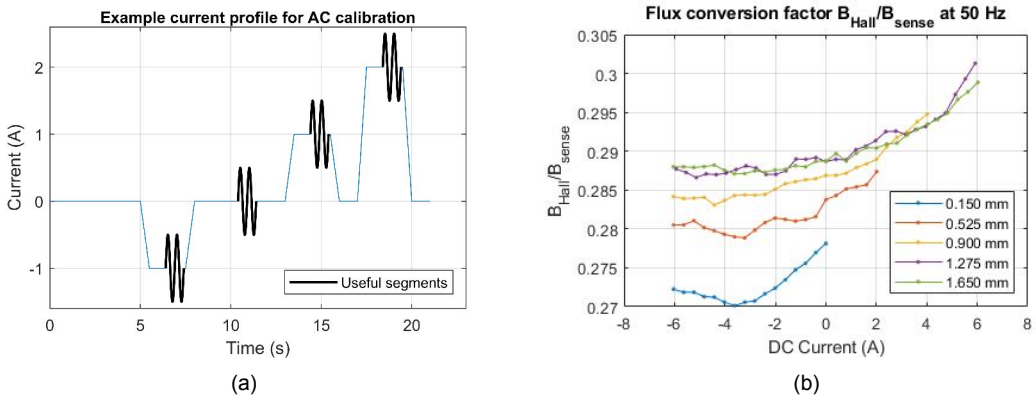

Figure 5.9: AC calibration of flux sensors: (a) example current input profile (with different amplitude and frequency than actually used, for a clearer illustration), (b) flux conversion ratio $B_{\text{Hall}}/B_{\text{sense}}$ at different gap sizes.

This can be explained by comparing the reluctance of the Hall sensor $\mathcal{R}_{\text{Hall}}$ with those of the iron core $\mathcal{R}_{\text{Fe}}$ and the air gap $\mathcal{R}_{\text{air}}$. Similar to electric current, magnetic flux always tends to travel via paths with lower reluctance. As the DC current moves away from the minimum-flux point, a decrease in permeability of the iron core leads to a higher reluctance $\mathcal{R}_{\text{Fe}}$, and as a result more flux tends to flow through the Hall sensor instead of going around it via the iron core. Similarly, as the gap size increases, $\mathcal{R}_{\text{air}}$ rises and $\mathcal{R}_{\text{Hall}}$ becomes less significant compared with $\mathcal{R}_{\text{air}}$, thus more flux more to pass through the Hall sensor instead of travelling around.

5.3.2.2 Measuring k_{flux} with respect to frequency

The previous section 5.3.2.1 only measures the flux output ratio k_{flux} at a fixed frequency of 50 Hz. This section performs frequency-domain measurements to investigate the frequency dependency of k_{flux}.

The frequency response from the driving coil current I_{coil} to the Hall sensor output B_{Hall} and the sense coil output $\dot{B}_{\text{sense}}$ are measured using the Bode 100 analyzer at the minimal (0.15 mm), nominal (0.90 mm), and maximum (1.65 mm) air gap as shown in Figure 5.10(a)(b). An ideal integrator $1/s$ is applied to the sense coil output to restore flux measurements B_{sense} (Figure 5.10(c)), and finally frequency response of the flux output ratio k_{flux} is obtained by dividing the frequency response $I_{\text{coil}} \rightarrow B_{\text{Hall}}$ using $I_{\text{coil}} \rightarrow B_{\text{sense}}$ (Figure 5.10(d)).

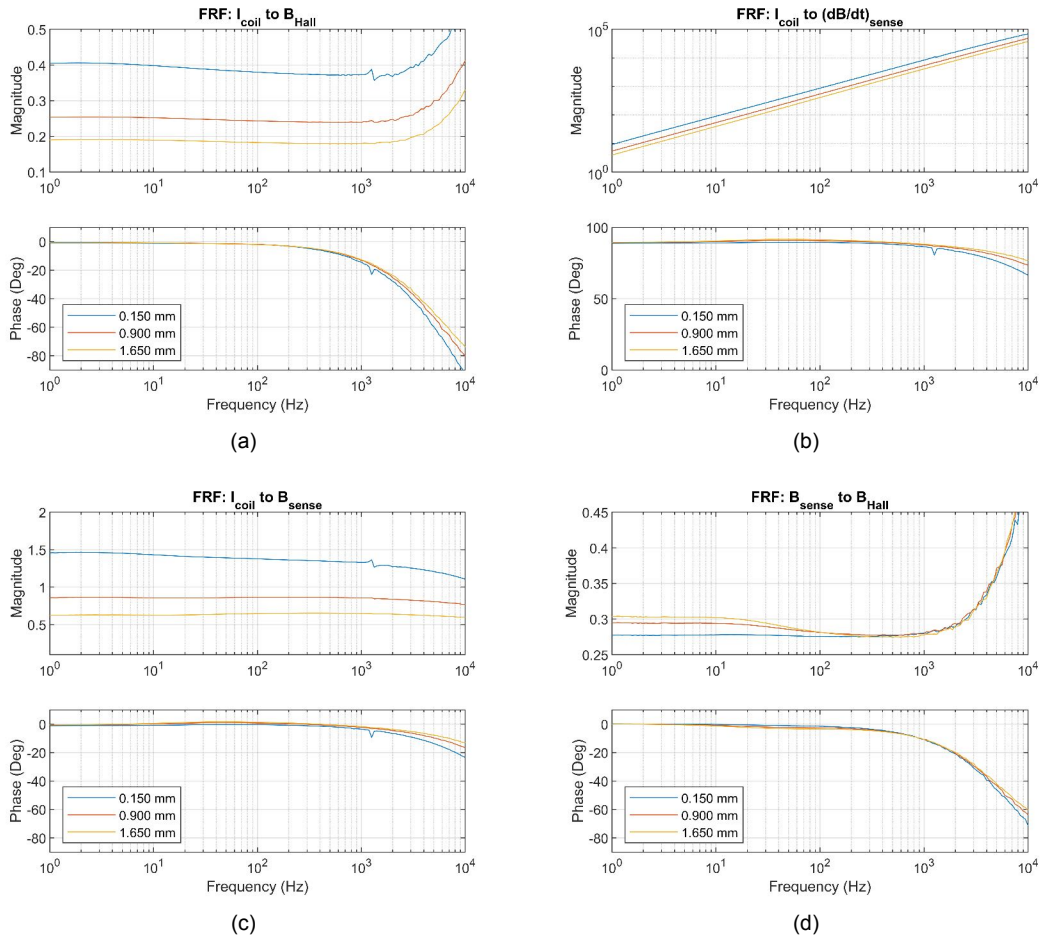

Figure 5.10: Frequency responses: (a) from current I to flux measured by Hall sensor B_{Hall}, (b) from current I to the rate of change of flux measured by sense coil $\dot{B}_{\text{sense}}$, (c) from current I to flux measured by sense coil B_{sense} (after applying integrator), (d) from B_{sense} to B_{Hall}, equivalent to the flux merging factor k_{flux}.

As shown in the bode plots, the frequency responses of the Hall sensor shows a significantly greater variation in gain and phase at high frequencies ($>$ 1 kHz). As a result, the measured k_{flux} is found to be dependent on both frequency and gap size. At low frequencies k_{flux} shows a clear difference at different gap sizes, while between 10 Hz and 200 Hz k_{flux} values at different gap sizes merge towards the same value, and for higher frequencies than 200 Hz the gap dependency is hardly noticeable anymore. Besides, the frequency response of k_{flux} shows a significant rise in magnitude from 1 kHz due to the high-frequency rise in the Hall sensor response $I_{\text{coil}} \rightarrow B_{\text{Hall}}$. The cause for this effect is still uncertain, with one potential cause being the increase of $\mathcal{R}_{\text{Fe}}$ due to the eddy current effect leading to more flux passing through the Hall sensor. However, this effect would barely influence the merged flux measurement since the signal from the Hall sensor will only be used for DC and low-frequency measurements as mentioned in section 2.4.

5.4. Hysteresis Loop

To estimate the influence of the hysteresis effect on the calibration results, the flux-current and force-current loops are measured by cycling the current within a certain range. The input current profile has a constant and very low slew rate of 1 A/s in order to eliminate dynamic effects. The current range is adjusted for different gap sizes to cover the designed force range of 0 - 500 N. Measured data are processed by averaging and low-pass filtering for noise reduction, and results obtained at the nominal air gap of 0.90 mm are plotted in Figure 5.11. For each hysteresis loop, the differences in flux and force at the same current level between the ascending and descending branches of the loop are plotted in Figure 5.12.

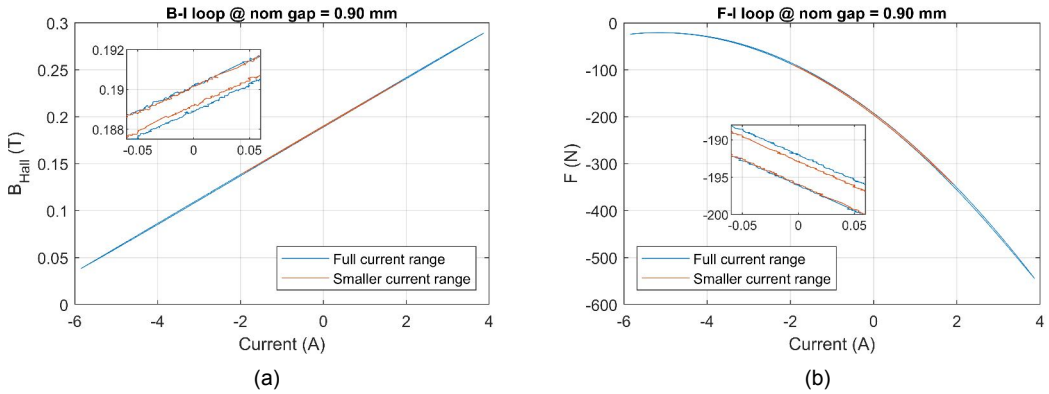

Figure 5.11: Hysteresis loops measured at nominal air gap of 0.9 mm: (a) between current I and flux measured by Hall sensor B_{Hall}, and (b) between current I and force F. It can be seen that loops with a smaller current range are narrower with smaller ΔB_{Hall} and ΔF between the ascending and descending branches of the loop.

In Figure 5.12, it can be observed that, for hysteresis loops covering the same force range of 0 - 500 N, a smaller gap size would result in a greater ΔB_{Hall} and ΔF between the ascending and descending branches at the same current level, meaning a greater hysteresis error. While comparing at the same gap size, hysteresis loops covering a bigger current or force range would result in a greater ΔB_{Hall} and ΔF and thus a greater hysteresis error. Overall, it is found that ΔB_{Hall} remains below 1 % of the full range of flux throughout the gap range, while ΔF reaches up to 3 % of the full force range and can only be kept under 1 % for $x_{\text{g}} > 0.90$ mm.

The results above are obtained when a laminated target plate made with silicon steel is used. To also quantify the hysteresis effect for the non-laminated target and compare it with the laminated target, the same experiment is carried out with the laminated target plate replaced by a non-laminated target of the same dimension made with stainless steel 430F, and the results are

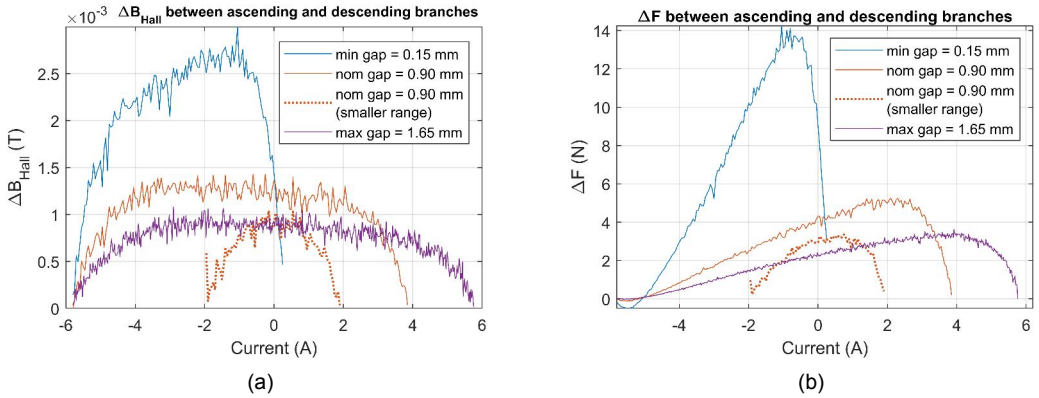

Figure 5.12: Differences between the ascending and descending branches of hysteresis loops for laminated target: (a) ΔB_{Hall}, and (b) ΔF. It can be seen that ΔB_{Hall} and ΔF are greater for smaller gap sizes or loops with wider current ranges.

compared in Figure 5.13 and Figure 5.14. It is found that the flux-current curve of the non-laminated target has a lower slope than that of the laminated target, with the slope ratio (calculated using fitted trend lines) $k_{\mathrm{nonlam}}/k_{\mathrm{lam}} = 0.957$. This is largely due to the difference in magnetic permeability between the materials used for the laminated and non-laminated target plates, i.e., silicon steel and stainless steel 430F, respectively. Calculating the ratio of total reluctance for the two cases (while taking 3000 and 800 as relative permeability values for silicone steel and stainless steel) gives $\mathcal{R}_{\mathrm{nonlam}}/\mathcal{R}_{\mathrm{lam}} = 0.961$, which closely matches with the measured slope ratio. Besides, for the same current range and gap size, the non-laminated target shows a much wider hysteresis loop. At nominal gap of 0.90 mm, for the non-laminated target, maximum ΔB_{Hall} is increased from 0.5 % to 2.0 % of full flux range and maximum ΔF increased from 1.0 % to 2.7 % of full force range compared with the laminated target. This indicates that the non-laminated target has a greater hysteresis loss under the same condition.

However, given the performance benefits of using laminated targets as shown above, non-laminated targets are still preferred for many applications in the industry for easier production and implementation. In this case, the results shown above will serve to quantify and estimate the performance loss for using a non-laminated target.

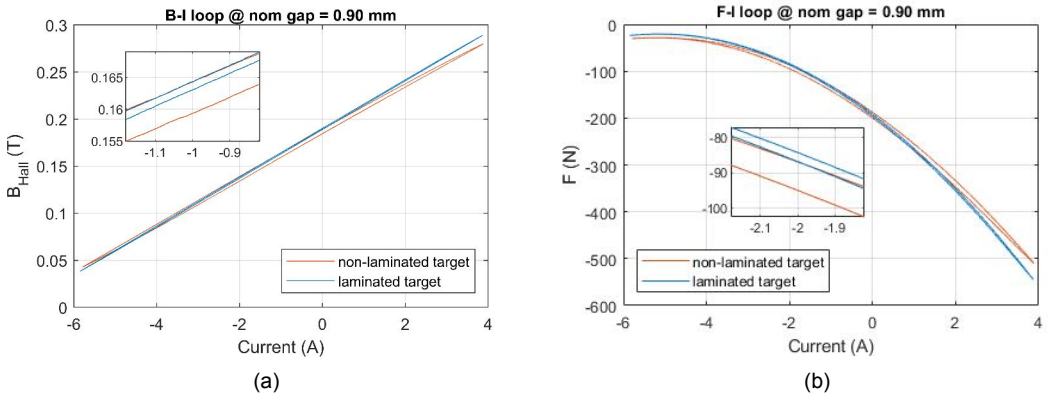

Figure 5.13: Hysteresis loops with laminated and non-laminated target plates.

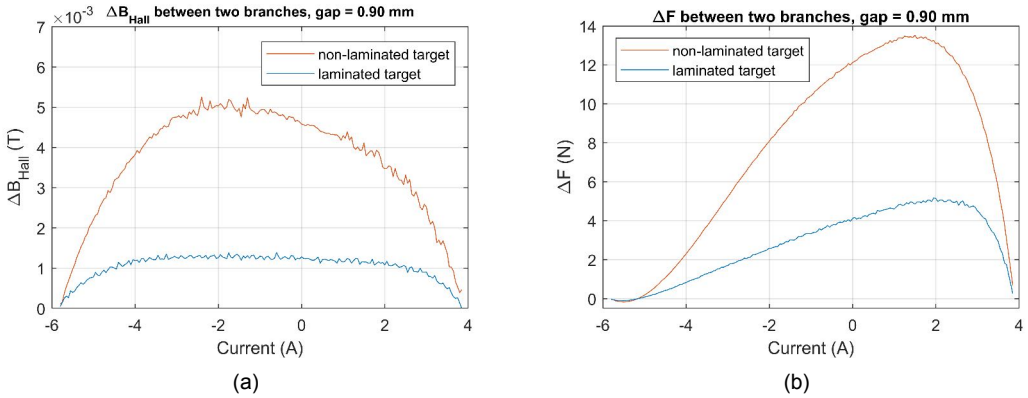

Figure 5.14: Differences between the ascending and descending branches of hysteresis loops, for laminated and non-laminated target plates: (a) ΔB_{Hall}, and (b) ΔF. By comparison, the non-laminated target has greater ΔB_{Hall} and ΔF (with maximum ΔB_{Hall} and ΔF increased from 0.5 % and 1.0 % to 2.0 % and 2.7 %), thus greater hysteresis errors, than the laminated target under the same conditions.

5.5. Hybrid Flux Measurement

In this section, the hybrid flux measurement scheme proposed in section 2.4 is implemented and validated experimentally. Firstly, the noise in the output signals of the Hall sensor and sense coil are measured and compared to determine the cutoff frequency for signal merging, then complementary filters are applied to the measured signals to test the merging results.

5.5.1. Preliminary: Flux Sensor Noise Measurement

To compare the noise characteristics of the Hall sensor and sense coil, their outputs are measured in several different configurations of measuring instruments to determine and understand the main sources of noise. This would provide the necessary information for configuring the signal merging scheme.

The noise in the Hall sensor and sense coil outputs are recorded simultaneously using a Speedgoat target machine with differential analogue input channels, at a sampling rate of 10 kHz. To be able to separate the noise contributed by each element in the measuring chain (i.e., flux sensors, differential amplifiers, power amplifier, and A/D converters) and identify the main source of noise, measurements are performed in several different equipment configurations (Figure 5.15), and in each of them certain elements are shortcutted to eliminate certain noise sources. Measured time series data are processed using fast Fourier Transform (FFT) to reveal frequency domain characteristics. The resulting power spectral density (PSD) of measured voltage signals (before applying sensor gains to convert voltage to flux density) are plotted in Figure 5.16(a)(b), and the corresponding average power of the measured noise are given by Table 5.1. It is found that, for both sensors, A/D converters and the power amplifier are the main sources of noise, while the flux sensors themselves contribute negligible noise in comparison. The contribution of the A/D converter and power amplifier to the Hall sensor noise is comparable, while for the sense coil, the power amplifier contributes to the noise with around 1000 times more power than A/D converters. As a result, the sense coil has a voltage noise that is around 500 times higher in average power than the Hall sensor noise.

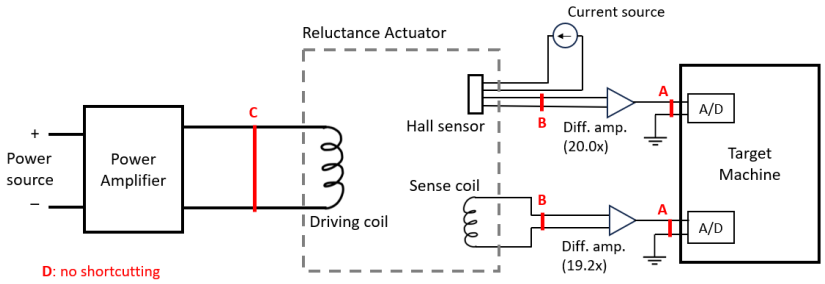

Figure 5.15: Equipment configurations for flux noise measurements. For configurations A, B, and C, the A/D converter inputs, differential amplifier inputs, and driving coil are shortcutted respectively as indicated in the drawing. For configuration D, no element is shortcutted.

Table 5.1: Average power of flux noise in different setup configurations (as illustrated in Figure 5.15).

Configuration	**Avg. power of noise** (V^2)	
	Hall sensor	Sense coil
A	1.8×10^{-15}	1.3×10^{-15}
B	1.8×10^{-15}	2.0×10^{-15}
C	3.4×10^{-15}	3.3×10^{-15}
D	4.8×10^{-15}	1.3×10^{-12}

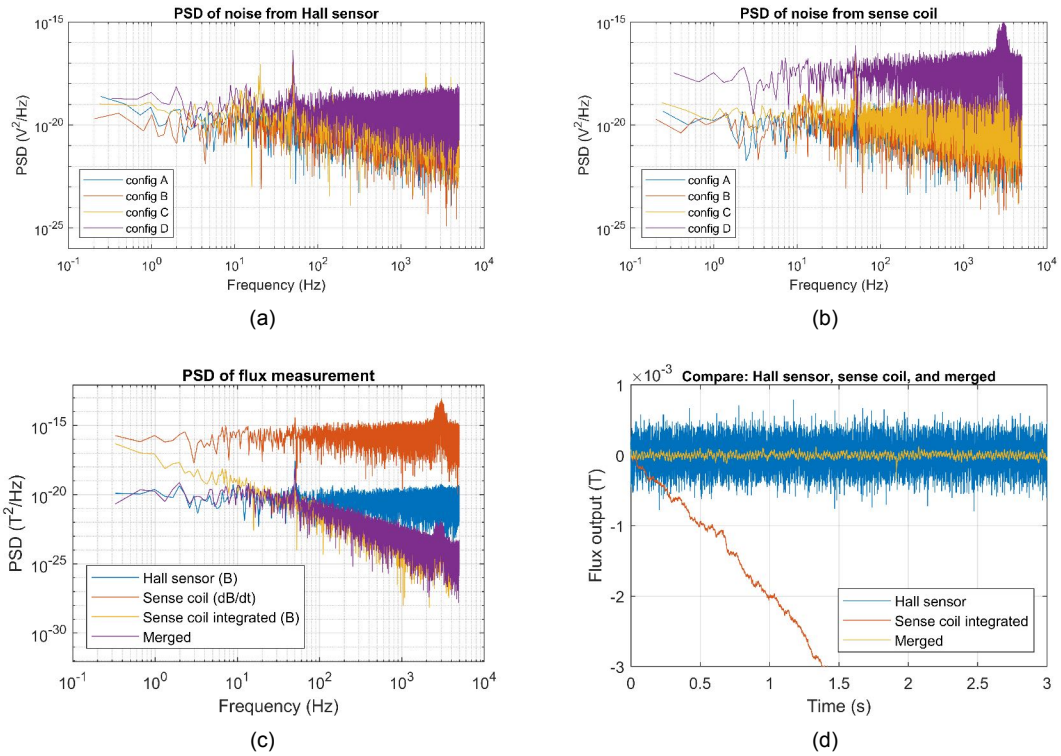

Figure 5.16: Noise comparison for flux sensors: PSD of voltage noise from (a) Hall sensor and (b) sense coil in different configurations, (c) Flux noise comparison between Hall sensor and sense coil, as well as a merged signal using complementary filters at $30\,\mathrm{Hz}$, (d) Flux noise comparison in the time domain between Hall sensor, sense coil and merged signal.

Then, to compare noises in flux density measurement, data measured without any shortcutting (configuration D) are taken, and the sense coil output is integrated using the cumulative trapezoidal method, after which corresponding sensor gains are applied to signals from both sensors to convert voltage into flux measurements. It needs to be mentioned that, a high-pass filter of 0.1 Hz is applied to the integrated sense coil output before FFT is performed, in order to eliminate the influence of DC drift (due to integration) on FFT results. Results for both sensors are plotted in Figure 5.16(c) for comparison, where it can be seen that flux output from the sense coil has greater noise than that from the Hall sensor at frequencies below 30 Hz, while for higher frequencies the opposite holds. Thus, second-order low-pass and high-pass filters with a cutoff frequency of 30 Hz can be used to merge flux signals, as proposed in section 2.4. PSD of the merged signal is also plotted in Figure 5.16(c), which shows that the noise in the merged signal is kept below or equal to the original noises. The effect of merging can also be seen by comparing the time domain signals (Figure 5.16(d)). The merged signal shows significantly lower noise than the Hall sensor output, and the time drift in sense coil output is also eliminated in the merged signal.

5.5.2. Frequency Response of Flux Measurement

As determined in the previous section 5.5.1, second-order low-pass and high-pass filters with cutoff frequency of 30 Hz as well as a k_{flux} of 0.295 for $x_{\text{g}} = 0.90\,\text{mm}$ (obtained at 1 Hz in Figure 5.10) are used for flux signal merging. The frequency responses from current in the driving coil to measured flux before and after signal filtering and merging are plotted in Figure 5.17. The general merging principle is demonstrated in Figure 5.17(a), where low- and high-pass filters are applied to Hall sensor and sense coil measurements respectively, and the filtered signals are added to form a merged measurement. In Figure 5.17(b), flux measurements from the Hall sensor and sense coil (after performing integration and applying a constant flux conversion factor k_{flux}) alone are compared with the merged hybrid measurement. However, it is found that the frequency responses of the Hall sensor and sense coil poorly match each other. Due to the frequency dependency of k_{flux} observed in Figure 5.10, using a k_{flux} measured at 1 Hz will only achieve a good match between the two signals at very low frequencies, while from 20 Hz their gains start to diverge with up to 10 % difference, until 2 kHz where the gain of Hall sensor measurement starts to rise rapidly. Thus, even though the merged signal is able to represent the expected merging effect, i.e. the merged FRF curve tends to converge with the Hall sensor measurement below 30 Hz and with the sense coil measurement after 30 Hz, the strong mismatch between Hall sensor and sense coil measurements in the frequency domain makes the flux measurement accuracy hardly improved or even worse compared to using a single flux sensor alone. Thus, further investigation and attempts would be needed, such as changing the location of the Hall sensor or the sense coil, to improve the accuracy and thus the feasibility of this hybrid flux measuring scheme.

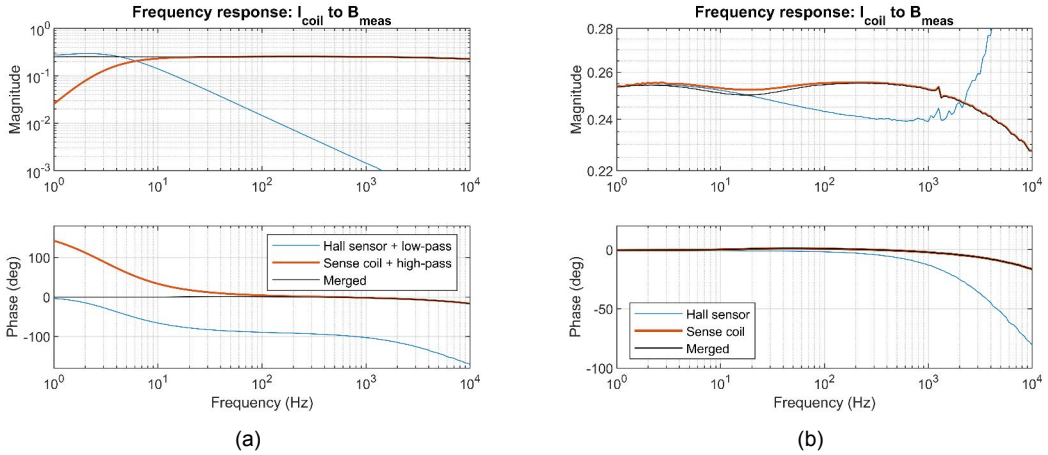

Figure 5.17: Frequency responses from current in the driving coil to measured flux from Hall sensor and sense coil (after performing integration and applying $k_{\text{flux}} = 0.295$), at nominal air gap of $0.9\,\text{mm}$.

5.6. Hybrid Force Measurement

A hybrid force measurement scheme was introduced in section 4.2.4, using a load cell together with two symmetrically configured accelerometers for force error compensation at high frequencies. FEM analysis was carried out in section 4.4, in which it was discovered that force error due to setup dynamics up to around 3 kHz can be partially compensated, and the maximum measurable frequency with less than 0.5 % error was increased from 800 Hz to 1200 Hz. To experimentally validate this effect, frequency responses from the driving coil current I_{coil} to the force measured by the load cell F_{load} and accelerometers $F_{\text{acc}} = m_{\text{eff}} a_{\text{acc}}$ are measured, where m_{eff} is the effective moving mass corresponds to the measured acceleration. Note that the force outputs are measured with respect to the current instead of the applied force as in the FEM analysis (section 4.4), since the actually applied forces are hard to be measured directly, so the relations with current are measured as a compromise. Then the merged force measurement is obtained by compensating the load cell output with the averaged force measured by the accelerometers, i.e., $F_{\text{merge}} = F_{\text{load}} + (F_{\text{acc},1} + F_{\text{acc},2})/2$ as proposed in section 4.2.4. Then the applied m_{eff} is tuned until an optimal compensating effect is achieved for the first observed mode (around 1300 Hz).

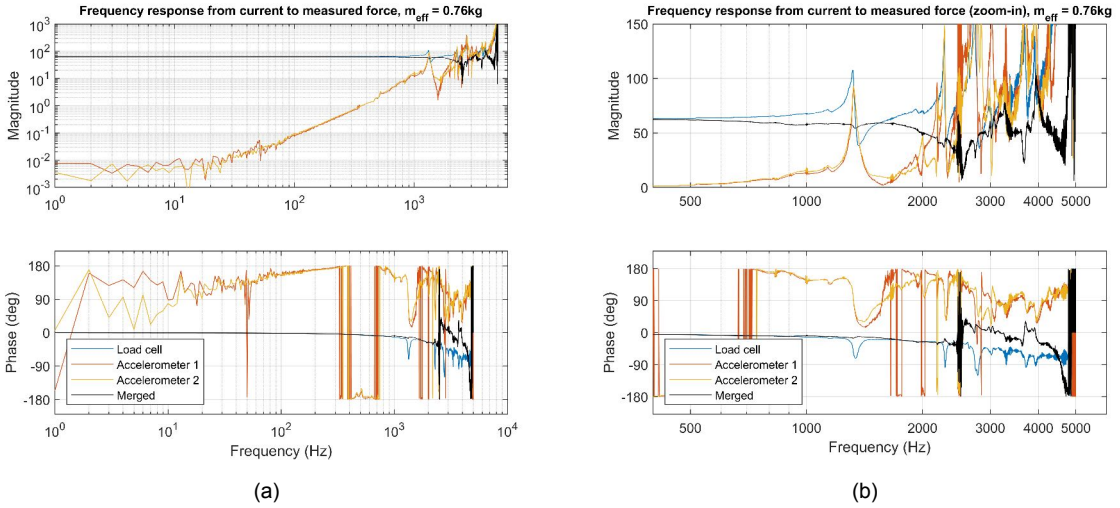

(a) (b)

Figure 5.18: Frequency responses from current to measured forces from the load cell and accelerometers: (a) full-frequency plot with magnitude in logarithmic scale, (b) zoom-in view at high frequencies with magnitude in linear scale.

However, an important notice is that, the relation between the current I and the measured force F_{meas} of a reluctance actuator, even without any influence of dynamic modes, is inherently nonlinear and frequency-dependent. Therefore, the measured $I \rightarrow F_{\text{meas}}$ curves in Figure 5.18 shows the combined effect of two relations: from the current to the applied force ($I \rightarrow F_{\text{apply}}$) and from the applied force to the measured force ($F_{\text{apply}} \rightarrow F_{\text{meas}}$), which cannot be distinguished from each other. Therefore, this measurement cannot be used to quantify the improvement in the force measuring uncertainty by signal merging. Nevertheless, since no resonance peak is expected in the $I \rightarrow F_{\text{apply}}$ relation, the effect of the signal merging can still be qualitatively verified by observing the suppression of resonance peaks in the merged signal.

In Figure 5.18, it can be seen that the mode at around 1.3 kHz is suppressed with a much lower peak in magnitude and phase. As a result, the gain variation in the merged signal is much reduced, with the maximum gain variation reduced from 51 % to 8 % up to 1.3 kHz, and reduced from 71 % to 14 % up to 1.7 kHz. This qualitatively proves that, by using the proposed hybrid force measuring

scheme, force error due to dynamic modes of the setup can be reduced up to at least 1.7 kHz and therefore the measurable frequency range can be expanded. However, as mentioned above, the improvement in force error cannot be quantified since the observed gain variation might also be partially caused by the dynamics in the $I \rightarrow F_{\text{apply}}$ relation. Another observation is that, the frequency of the first observed mode (around 1.3 kHz) is different than that found in the FEM analysis (around 1.8 kHz), and the optimal value of m_{eff} for achieving the best compensation effect on the first mode is also different from the one found in the FEM analysis. This can be explained by the simplification made on the CAD model used for FEM analysis, such as ignoring contact stiffness and modelling parts in contact as a single combined part, which is expected to result in an overestimation of mode frequencies.

6

Conclusions and Recommendations

6.1. Conclusions

Based on the achieved outcomes and experimental results, the following conclusions can be drawn.

- **A literature review on the linearisation and flux measurement of reluctance actuators is carried out, based on which schemes for implementing current and flux control are proposed.**
  The improvements in actuator linearity and control accuracy of using flux control instead of current control are experimentally verified in the literature. For flux sensing, it is also shown in the literature that applying a hybrid flux estimation scheme using a sense coil together with a Hall sensor or a current sensor is able to improve accuracy and extend the measurable frequency range of the measurement. As a result, a flux control scheme with nonlinear compensation and a hybrid flux estimation scheme using a Hall sensor and a sense coil is proposed for future implementation.

- **A hybrid reluctance actuator prototype that is suitable for both current and flux control is designed and realised.**
  A peak force output of 500 N and root-mean-square force of 354 N can be achieved throughout the designed gap range of 0.15 - 1.65 mm. A continuous force density of 119 N/kg with respect to the total actuator mass or 983 N/kg with respect to the moving mass is realised, which is found to be much higher than those realised by standard Lorentz actuators [16][17].

- **A hybrid flux measuring scheme using a Hall sensor and a sense coil is proposed and implemented on the designed actuator.**
  A Hall sensor placed in a slot on the stator pole and a sense coil placed around the stator pole are both implemented. The merged flux signal obtained using second-order complementary filters is found to have minimised noise and zero DC drift. However, the output ratio between the Hall sensor and the sense coil is found to be dependent on gap size, DC current, and frequency. As a result, a good matching between the two sensor outputs for all frequencies cannot be achieved using a constant merging factor k_{flux}. Thus, unless the mismatch between the Hall sensor and the sense coil outputs can be much reduced in future work, flux measurement using a single flux sensor alone might provide a more reliable measurement. Besides, a significant gain variation above 1 kHz is observed in the frequency response from I_{coil} to B_{Hall}, which might be due to the special way of placing the Hall sensor in a slot on the core. Further investigation is needed on the cause of such a phenomenon.

- **A 1-D test setup for the reluctance actuator prototype has been designed and realised.**
  The setup is capable of measuring the force output of reluctance actuators up to at least 500 N and positioning the actuator through the gap range of 0 to 40 mm (with position

measurement available within 0 - 10 mm). A linear static stiffness of 1.9×10^8N/m can be achieved in the force measuring direction.

- **A hybrid force measuring scheme using a load cell and accelerometers is proposed and implemented.**
  By compensating the load cell output using acceleration measurements, force error due to resonance modes of the setup is reduced up to at least 1.7 kHz. As a result, the maximum gain variation in the frequency response from current to measured force is reduced from 51 % to 8 % up to 1.3 kHz, and reduced from 71 % to 14 % up to 1.7 kHz. The improvement in load measuring repeatability has yet to be experimentally quantified, while the FEM analysis suggests an improvement in the maximum measurable frequency from 800 Hz to 1200 Hz for a force error below 0.5 %.

- **DC calibration is performed to characterise the relationship between current, flux, gap size, and force output for the purpose of nonlinear compensation.**
  The actuator is calibrated at different gap sizes throughout the designed force range of 0 - 500 N. 3D mappings of $F(I, x_g)$ and $F(B, x_g)$ can be made by interpolation using the measured data, and look-up tables for any given data grid can be extrapolated and then used for nonlinear compensation. However, the influence of DC drifting of the load cell is found hard to predict or compensate for, and thus might have an uncertain influence on the repeatability of the calibration results, where further investigation is still needed.

- **Hysteresis loops $B(I)$ and $F(I)$ are measured for both laminated and non-laminated target plates.**
  For the laminated target, hysteresis errors for flux and force are found to be up to 1 % and 3 % of their full range, respectively. While using a non-laminated target plate instead, it is found to produce wider hysteresis loops the flux and force errors at the nominal air gap being 4 and 2.7 times greater, respectively.

6.2. Recommendations

For the purpose of improving the results of existing measurements as well as making further progress, the following recommendations are given for future works.

- **Determine and improve the repeatability of the bias force measurement.**
  The DC drifting of the load cell output is found to be more significant and unpredictable than expected, with a varying rate over time up to 0.05 - 0.10 N/s. For the measurement of the bias force (section 5.3.1), it is found especially hard to predict, quantify, and compensate for the influence of the DC drifting of the load cell. For future work, a few recommendations are given for determining and improving the repeatability of this experiment.
  - Carry out the experiment with a constant negative current (such as -2 A or -4 A) in the driving coil, in addition to the zero-current case above. As a result, the force drift might be lower due to the lower changing rate of the applied force. These results are redundant with the result from the zero-current case, and thus can replace the zero-current bias force measurement for bias force compensation if a significant reduction in force drift is observed.
  - After varying the air gap from 0 to 35 mm, add a “return trip” to let the air gap travel from 35 mm back to 0 mm. As a result, for each gap size, two force measurements can be obtained with known time separation. This provides more information on understanding the force drift and might enable a more accurate drift compensation.
  - Shortcut the flux loop using a separate plate at $x_g = 35$ mm so that the force applied on the target reaches absolute zero. This provides a more accurate way of setting the zero point of the measured force curve.

- **Further investigate on the feasibility of the hybrid flux measuring scheme.**
  It is concluded in this project that the presence of the mismatch between the Hall sensor and sense coil in the frequency domain makes it unrealistic for the hybrid flux measurement to achieve a more reliable measurement than using a single flux sensor alone. However, modifications to the currently applied hybrid flux measuring scheme can be made in attempting to reduce the mismatch, such as relocating the sense coil onto the same stator pole with the Hall sensor. Besides, further investigation on the frequency response of the Hall sensor is also needed to explain the significant gain variation after 1 kHz. Finally, a more comprehensive comparison can be made between different flux measuring schemes, and draw a final conclusion on the feasibility of the hybrid flux measuring scheme proposed in this report.

- **Further test on the hybrid force measuring scheme and quantify the results.**
  In this project, the hybrid force measuring scheme using a load cell and two accelerometers is implemented and tested. However, the compensation effect is only observed qualitatively while the improvement in the measuring repeatability cannot be determined. Therefore, the effect of this force measuring scheme still needs to be further tested and investigated in order to determine the results quantitatively.

- **Make more comprehensive comparison between non-laminated and laminated targets.**
  In this project, hysteresis loops measured with laminated and non-laminated target plates are compared. In future works, the comparison can be made more comprehensive by involving more aspects, such as the actuator impedance, frequency responses related to the measured flux and force, etc. This will help quantify the loss in performance when non-laminated targets are used.

- **Experimentally implement the proposed flux control in a closed loop and compare the achieved performance with the current control.**
  This project serves to prepare for the experimental implementation of flux control and perform actuator calibration. Based on the results and findings concluded from this project, and by using the actuator and setup realised in this project, attempts to implement flux control can be made.

Bibliography

[1] Max Jans. “Comparison of reluctance actuator control strategies: Modelling and analysis of Inner control loops for reluctance actuators”. Bachelor’s Thesis. Fontys Hogescholen Engineering, June 2022.

[2] Shingo Ito, Francesco Cigarini, and Georg Schitter. “Flux-controlled Hybrid Reluctance Actuator for High-precision Scanning Motion”. In: *IEEE Transactions on Industrial Electronics* 67.11 (2020), pp. 9593–9600.

[3] Andelko Katalenic. “Control of Reluctance Actuators for High-Precision Positioning”. PhD thesis. Technische Universiteit Eindhoven, Apr. 2013.

[4] Ian MacKenzie. “Design and control methods for high-accuracy variable reluctance actuators”. PhD thesis. Massachusetts Institute OF Technology, Feb. 2015.

[5] Xiaodong Lu. “Electromagnetically-Driven Ultra-Fast Tool Servos for Diamond Turning”. PhD thesis. Massachusetts Institute OF Technology, Sept. 2005.

[6] Robert Munnig Schmidt et al. *The Design of High Performance Mechatronics*. Third. Amsterdam: Delft University Press, 2020. ISBN: 978-1-64368-051-4.

[7] Leon Jabben. “Mechatronic Design of a Magnetically Suspended Rotating Platform”. PhD thesis. Technische Universiteit Delft, Dec. 2007.

[8] Min Chen and Carl R. Knospe. “Feedback Linearization of Active Magnetic Bearings: Current-Mode Implementation”. In: *IEEE/ASME Transactions on Mechatronics* 10.6 (2005), pp. 632–639.

[9] A. Katalenic et al. “Linearization of a current-driven reluctance actuator with hysteresis compensation”. In: *Mechatronics* 23 (2013), pp. 163–171.

[10] A. Katalenic, C.M.M. van Lierop, and P.P.J. van den Bosch. “On hysteresis and air gap disturbance in current and voltage mode feed-forward control of variable reluctance actuators”. In: *2011 50th IEEE Conference on Decision and Control and European Control Conference* (Dec. 2011), pp. 1608–1613.

[11] Yuan et al. *Stage Having Paired E/I Core Actuator Control*. U.S. Patent 6,069,417, May 2000.

[12] Young Chol Kim, Seung Ki Ryu, and Jeong Woong Ryu. “Gain Scheduled Control of Magnetic Suspension System”. In: *KACC* (1993), pp. 321–326.

[13] Shingo Ito et al. “Long-range Fast Nanopositioner Using Nonlinearities of Hybrid Reluctance Actuator for Energy Efficiency”. In: *IEEE Transactions on Industrial Electronics* 66.4 (2019), pp. 3051–3059.

[14] Mohammed Asadullah Khan et al. “Magnetic sensors-A review and recent technologies”. In: *Engineering Research Express* 3.022005 (2021).

[15] James E. Lenz. “A Review of Magnetic Sensors”. In: *Proceedings of the IEEE* 78.6 (June 1990), pp. 973–989.

[16] H2W Technologies, Inc. *Non-Comm DC Voice Coil Linear Actuator - NCC12-60-1000-2X*. URL: https://h2wtech.com/product/voice-coil-actuators/NCC12-60-1000-2X (visited on 11/12/2023).

[17] Sensata Technologies, Inc. *Cylindrical Frameless Linear Voice Coil Actuator*. URL: https://www.sensata.com/products/motors-actuators/cylindrical-frameless-linear-voice-coil-actuator-la50-65-000a (visited on 11/12/2023).

A

Actuator Assembly

In this section, all the steps for the assembly of the actuator, including post-machining, mechanical assembly and potting, are described.

A.1. Assembly Plan and Tooling

Preparation

The main components of the actuator, including lamination stacks of the stator core and the target plate, driving coil, Hall sensor, sense coil cable, stator housing, and target housing, are fabricated. Meanwhile, necessary 3D-printed toolings are prepared.

Post-machining

A slot and a through hole on the center pole of the core for accommodating the Hall sensor as mentioned in section 3.3.1, and a threaded hole on the side for connecting the grounding wire as mentioned in section 3.3.2, need to be machined.

A pair of thick aluminum plates with threaded rods are used to clamp the stator core in the direction of lamination, in order to prevent the lamination from getting loose during milling, drilling, and tapping. Figure A.1 shows the clamped stator core.

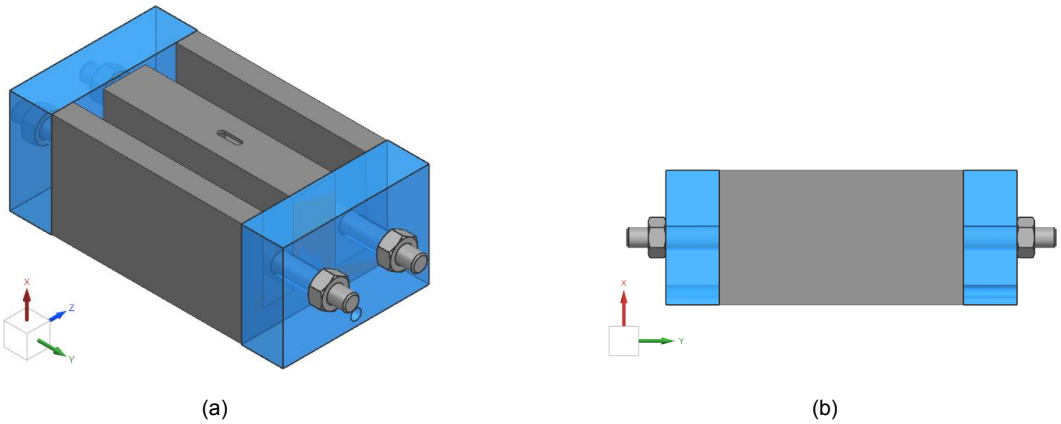

(a) (b)

Figure A.1: Stator core clamped using aluminum plates (in blue) and threaded rods.

Hall sensor installation

The two-component epoxy glue Scotch-Weld DP490 is mixed with 150 - 200 µm glass beads (as bond line controller), and applied to bond the Hall sensor onto the stator core in the machined slot. The sensor wires are protected using heat shrink tubes against sharp edges, and then led to the bottom of the stator core through the hole.

Magnet installation

The two-component epoxy glue Scotch-Weld DP490 mixed with 150-200 µm glass beads (as bond line controller) is used to bond the magnets onto the center pole of the stator core. However, due to the repulsive force between each magnet piece, the magnets tend to push each other away. Thus, some constraint forces are needed to hold the magnets in place once they are installed, until the epoxy glue is sufficiently cured.

For this purpose, a set of 3D-printed tooling is designed (Figure A.2), to apply pressing force on the magnets against the pole surface, and meanwhile provide side-ward constraints. The former serves to provide top-down constraints and increases the friction between the magnets and the pole surface, while the latter serves to align and constrain the magnets sideways at correct positions.

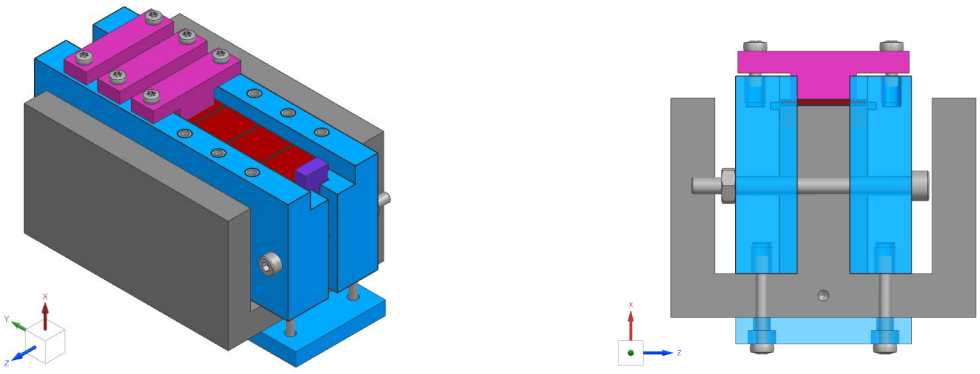

(a) (b)

Figure A.2: Stator core with 3D-printed tooling for magnet installation.

Before the installation, all 3D-printed tools are coated with PTFE spray for easier release from the epoxy. First, the epoxy glue is applied throughout the pole surface. After each magnet piece is slid onto the pole and pushed into place (against the repulsive force), the corresponding top constraint block will be installed to lock the magnet in place. Once all the magnets are installed and locked, the epoxy glue is cured at room temperature for ~ 4 hours, then all the auxiliary 3D-printed tools are carefully removed. This way, the epoxy would be hard enough to hold the magnets in place without the tooling, but still not too hard for any unwanted epoxy residue to be removed. The core-magnet assembly is then left in room temperature until the epoxy at fully cured.

Grounding wire connection

A grounding wire is connected to the stator core with a bolt and a fork connector, using the threaded hole made in the “post-machining” step.

Driving coil installation

The driving coil is prepared by wrapping 0.15 mm Nomex paper around the long side of the coil for a better insulation against the stator core. Then the coil is slid onto the stator core, and a wedge pair

is applied at each short side of the coil Figure A.3, to fix the coil relative to the stator core using normal force and friction force.

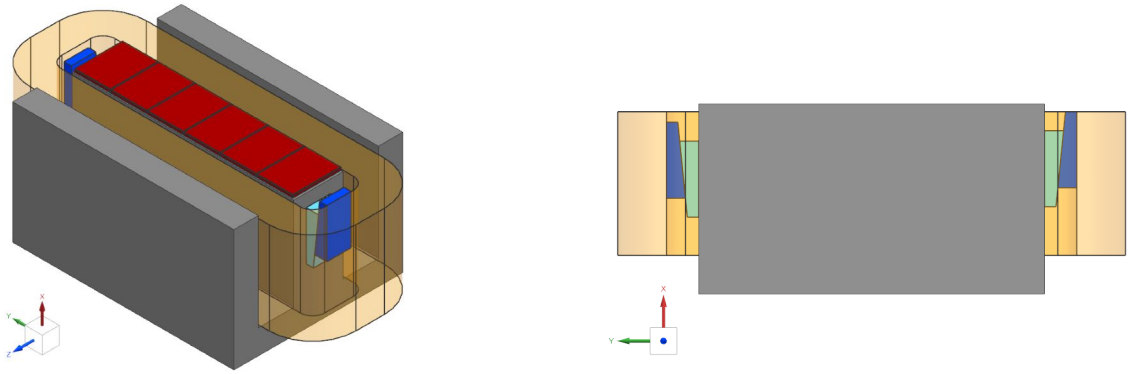

(a) (b)

Figure A.3: Installation of the driving coil onto the stator core using wedge pairs (blue in figures).

Sense coil installation

According to the winding scheme described in section 3.3.1, a sense coil with 4 turns is implemented using a coaxial cable with a conductor diameter of 7×D0.08 mm and outer diameter of 1.13 mm. In addition, Kapton tape is used to hold the winding in its original shape and place.

Stator housing mounting

The actuator assembly is then put into the stator housing, and set screws are used to push the stator core sideways onto the dedicated contact features on the housing, which are designed to ensure a decent alignment accuracy as described in section 3.3.6.

Finally, the assembled actuator stator is shown in Figure A.4.

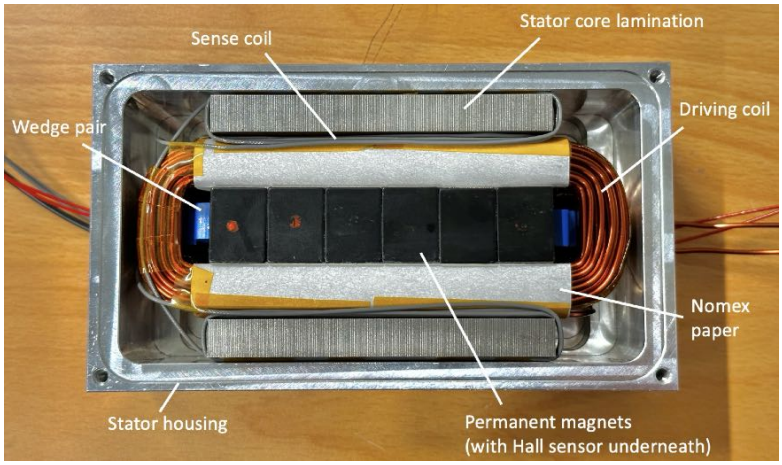

Figure A.4: Assembled actuator stator before potting.

A.2. Potting

Potting is carried out on the assembled stator in order to fix all the components together in place.

Base plate mounting

A 20 mm aluminum base plate is mounted on top of the stator assembly, to ensure a flat top surface of the actuator after the curing of the potting compound (Figure A.5). Between the base plate and the stator assembly, a 1.5 mm silicone ring is used for sealing, which is shown in green in Figure A.5, and a 1.5 mm silicone sheet is used as the release agent to prevent the epoxy resin from making direct contact with the base plate, which might make the base plate unable to detach. The actual assembly after mounting the base plate is shown later in Figure A.8(a).

It is worth mentioning that, while tightening the bolts to mount the base plate, the gap between the base plate surface and the stator housing top surface is monitored and controlled to an optimal value determined in a preliminary test, to make sure the four bolts are properly and evenly tightened, so that the top surfaces of the two side poles will make full contact with the silicone sheet. Otherwise, over-tightening might reduce the gap size between the silicone sheet and certain components (such as magnets, driving coil, and sense coil), reducing the bonding effect of the potting, while unequal tightening at different bolts might make the top surfaces of the side poles unable to make full contact with the silicone sheet, resulting in an uneven top surface of the actuator after curing.

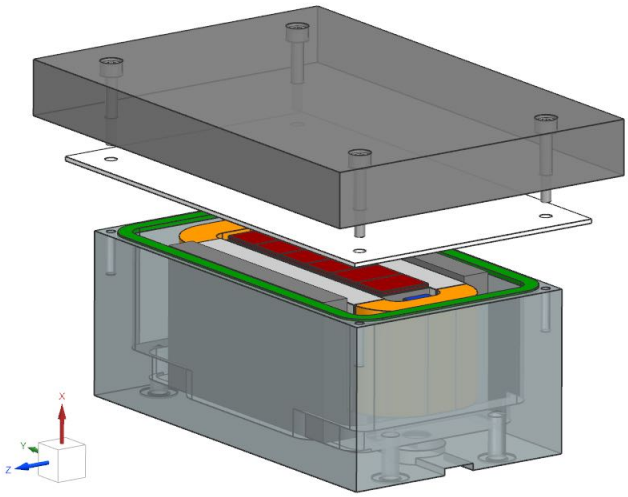

Figure A.5: Mounting of the base plate before potting. A silicone ring is used for sealing (shown in green in the CAD model), and a silicone sheet is used as a release agent to isolate the potting compound from the base plate.

Pouring and curing

To ensure a good filling of the potting epoxy to achieve the anticipated bonding and insulating effect of the potting epoxy, a potting procedure using a vacuum chamber is designed:

- The resin and hardener are preheated to 40 °C (to reduce the viscosity of the mixture).
- The resin and hardener are mixed at the specified ratio at room temperature, and the mixture is stirred slowly (to trap less air inside the mixture).
- A certain amount of mixture (less than 1/3 of the total amount needed) is injected into the assembly (in a vacuum chamber) from one of the three holes (as shown in Figure A.7).
- The vacuum chamber is sealed and the pump is switched on to start extracting air. The inner pressure is released every time it reaches a relatively low level and stops decreasing further. When the speed at which air bubbles come out slows down significantly (or when it reaches 2-3 minutes if air bubbles are not visible), the pump is switched off.

- Repeat the 3rd and 4th step above, and adjust the amount of the mixture being added each time depending on the condition, until the assembly is fully filled and the degassing is considered sufficient. Then, a certain amount of mixture is added to the three “pools” on top of the holes until they are full.
- The assembly is placed at room temperature for at least 48 hours to cure the potting compound (epoxy resin), and the assembly is put in a 50-60°C oven for 3-4 hours for post-curing.

Before implementing the pouring procedure above using the real actuator assembly, to check if the anticipated filling effect can be realised using the designed potting procedure, a test pour is carried out using a dummy actuator made of 3D-printed parts.

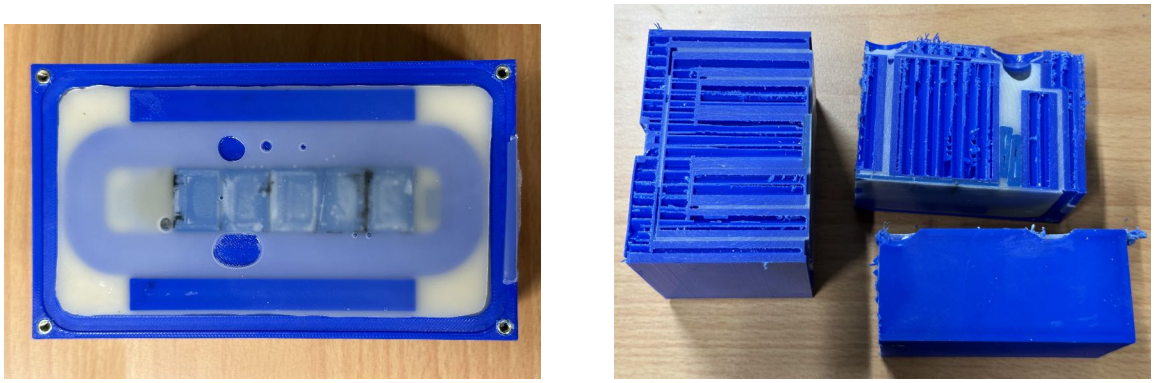

(a) (b)

Figure A.6: Test potting using 3D-printed actuator parts: (a) top surface after curing of the potting compound, (b) Cut assembly after curing, to check the filling of the potting compound at cross sections.

By inspecting the results shown in Figure A.6, it is found that most of the small gaps are properly filled with potting compound, while some cavities can still be observed, especially in the middle of big surfaces (Figure A.6(a)) and at corners (Figure A.6(b)). However, considering the scale of the cavities, they are expected to have no major influence on the final effect of the potting. Thus it is concluded that the designed potting procedure is able to achieve the expected filling effect, while some improvements are still made to aim for a better filling quality:

- Tilt the actuator while pouring the potting compound until more than half of the potting compound has been poured in, to reduce the amount of air trapped at the bottom.
- Preheat the actuator assembly before pouring the potting compound, to keep the potting compound at a higher temperature (thus lower viscosity) for a longer time during potting.
- Degas the actuator assembly in the vacuum chamber for a longer period, to remove more air from the assembly.

Then, using the improved pouring steps, the potting process is carried out on the real actuator assembly. The pouring process in a vacuum chamber is shown in Figure A.7, the assembly after the pouring process is shown in A.8(a), and the assembly after curing and post-curing is shown in A.8(b), demonstrating the final outcome of the potting. As a result, the potting compound is sufficiently hardened, and the components of the actuator are sufficiently covered by the potting compound, with the side poles of the core being the top surface of the actuator as desired.

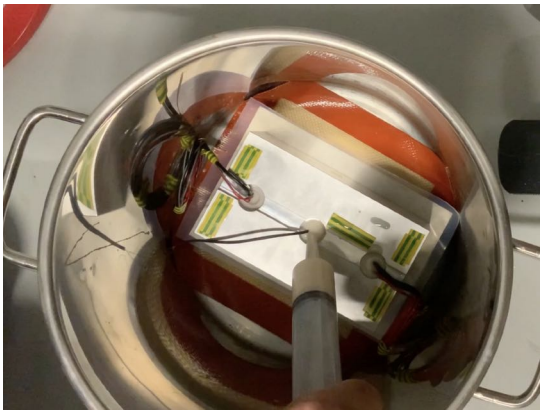

Figure A.7: During potting in a vacuum chamber.

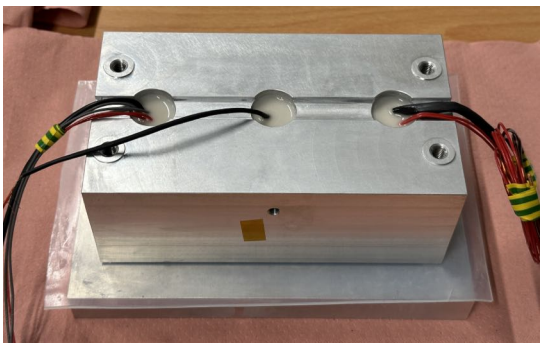

(a)

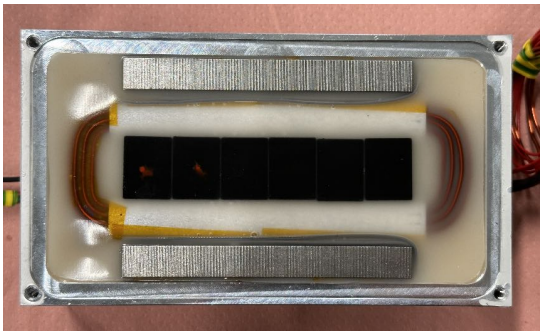

(b)

Figure A.8: Actuator assembly (a) after pouring the potting compound, (b) after the potting compound is fully cured.

B

Test Setup Assembly

Load cell preloading and target plate installation
To enable tensile force measurement and reach a more linear operation zone for the load cell, the load cell is preloaded with about 20 kN (10 % of the full range of the load cell). Meanwhile, the target is installed onto the base plate, with the load cell in between. To align the target plate in Y, Z, and RX direction when the preloading torque is applied, alignment tools shown in Figure B.1 are designed and used. To monitor and control the applied preload, the force output is measured during the preloading process. The same preload needs to be applied every time this process is carried out, to make sure all the calibration and measurement data are still repeatable.

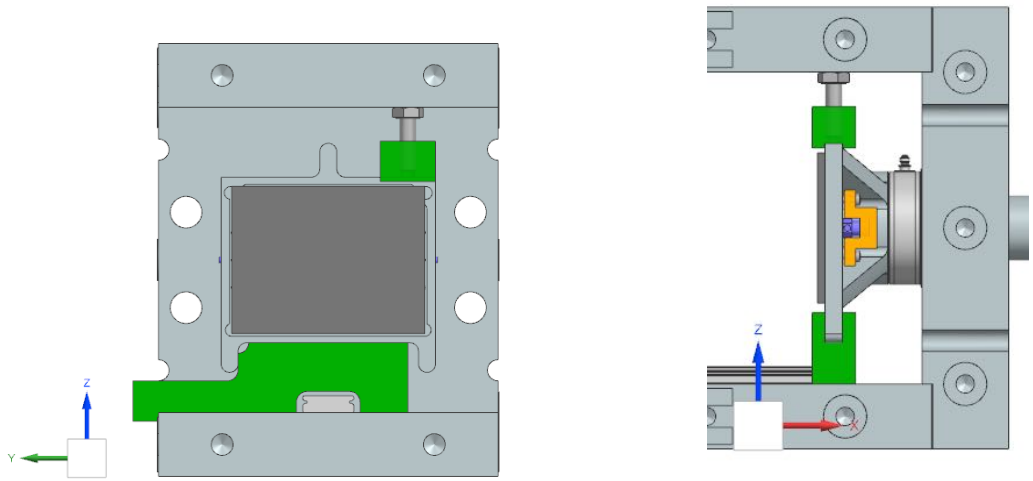

(a) (b)

Figure B.1: Alignment of the target plate while applying preload to the load cell, using customised alignment tools (shown in green).

Then, the load cell is calibrated in this configuration but with the loading direction being vertical Figure B.2, using other unassembled parts as reference weights. The purpose is to update the sensitivity of the load cell at the preloaded state, thus the influence of changing the loading direction on the calibration results is expected to be negligible.

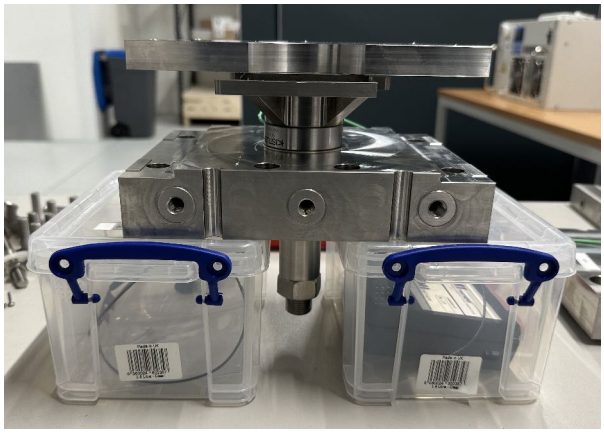

Figure B.2: Configuration for calibration of the load cell. A metal plate is already placed on top of the target plate as a reference weight.

Stator installation and alignment

In order to align the stator with the target plate in the Y, Z, and RX direction, a 3D-printed alignment tool is used while mounting the stator assembly onto the back plate Figure B.3.

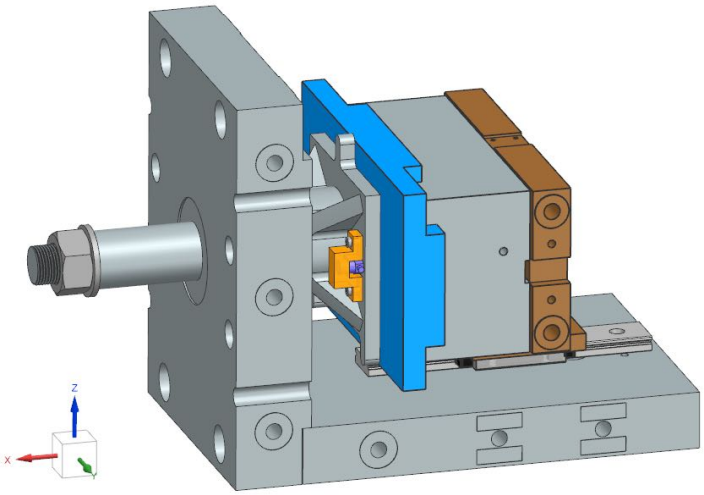

Figure B.3: Alignment between the stator core and the target plate, using a 3D-printed tool (shown in blue).

However, the alignment tool is not able to correct any misalignment in the RY and RZ direction, which means the stator and the target plate might be nonparallel, leading to a nonuniform gap size. The nonparallelism between the two surfaces can be measured by bringing the two surfaces in contact, zeroing the position probes, and then observing the difference in the readings of the probes when the stator is being pulled away from the target plate. By applying shims at the contact area between the stator housing and the back plate and repeating the steps above to install and align the stator, a uniform air gap can finally be achieved.

Then, the rest of the parts are assembled without special tooling needed, and the assembly of the setup is completed.

C

Mode Shapes from FEM Analysis of the Test Setup

Deformation of the first five modes observed in the simulated frequency response from applied force to measured force Figure 4.9 are shown below.

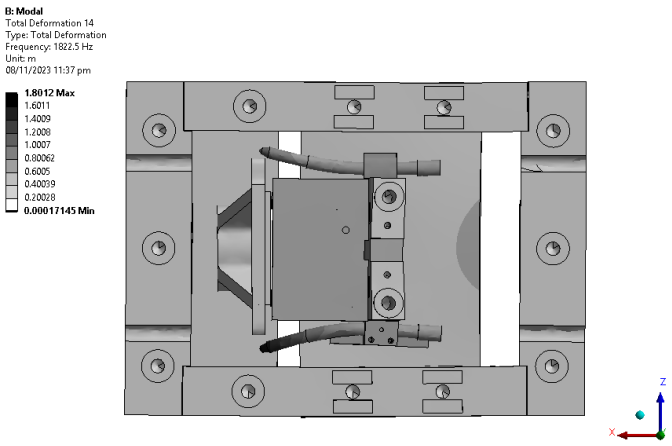

Figure C.1: Mode shape at 1823 Hz.

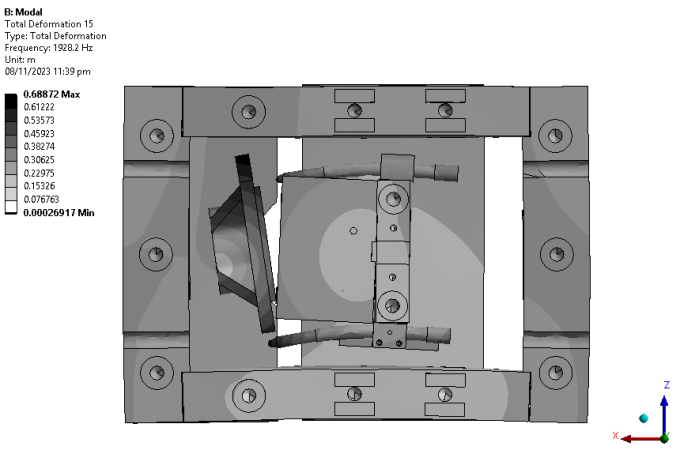

Figure C.2: Mode shape at 1928 Hz.

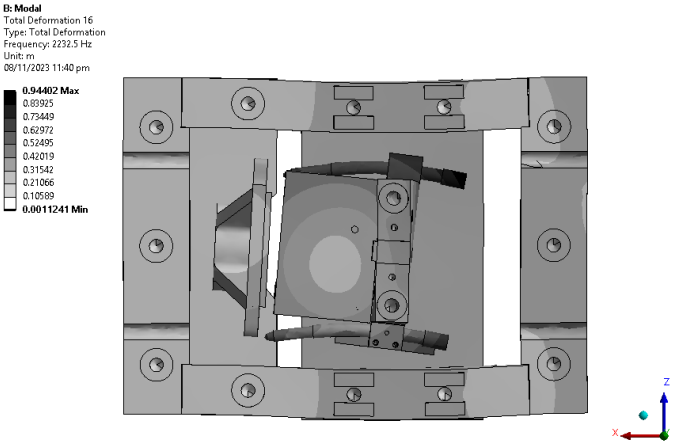

Figure C.3: Mode shape at 2233 Hz.

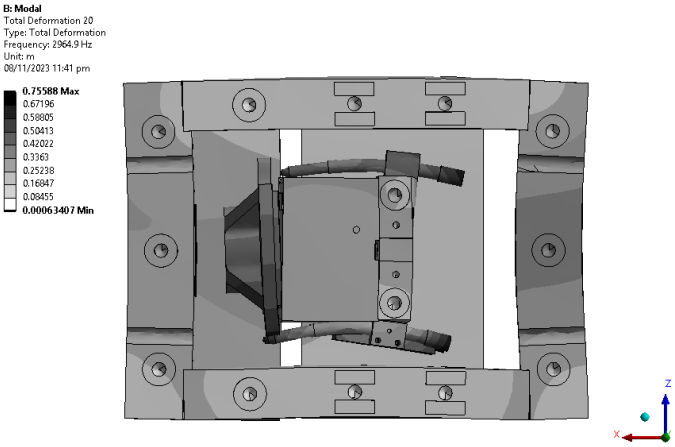

Figure C.4: Mode shape at 2965 Hz.

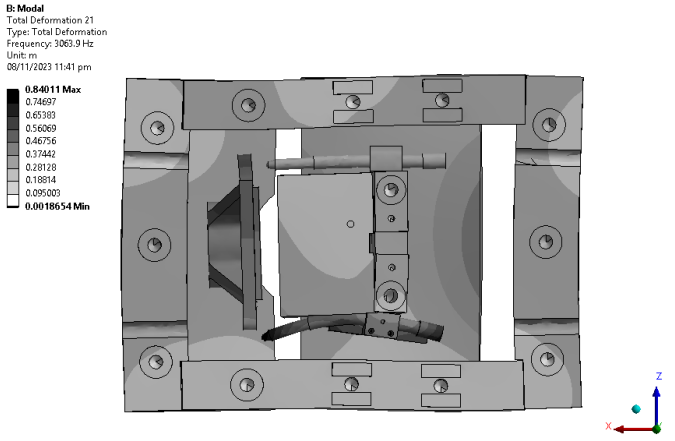

Figure C.5: Mode shape at 3064 Hz.